Novel Approach to the Study of Surface Plasmon Resonance and Field Enhancement Properties of Noble Metal Nanostructures

by

Moussa Ngom

A dissertation submitted in partial fulfillment
of the requirements for the degree of
Doctor of Philosophy
(Applied Physics)
in The University of Michigan
2009

Doctoral Committee:

Professor Theodore B. Norris, Chair
Professor Bradford G. Orr
Professor Herbert Graves Winful
Associate Professor Nicholas Kotov
Donnell Thaddeus Walton, Corning Inc.

To N'Datte (Sokhna Aminata Wyatt Ngom):
only you, my love could have accompanied me along this route. There aren't words I can come up with that will come close to describing my love for you
and N'Gouts (Marie Ngounda Ngom):
for bursting in the scene and making your presence felt, I know you'll be something special.

ACKNOWLEDGEMENTS

First and foremost Bethamie Lynn Wyatt (Ngom) who's been there in the beginning: it's a shame we did not make it to the finish line together, thank you for stacking up the challenges and keeping me on my toes the whole time: thank you for putting up with me and for helping me become what i am today. You and I will always share this history and our precious child.

To Ted (the satisfied bear) for never saying no, the man that has more great ideas than most. My favorite sentence of yours: "I have this great idea..." send me down the path then give me all the credit; thank you for providing the resources and building my confidence to take on this challenge. I'll work on inserting Swahili letters in my future science.

To Donnell for your friendship, your availability (when you feel like it), and for strongly suggesting Michigan and sending me to Roy and Brad. Brad for introducing me to Ted and for being always supportive with ideas, suggestions, and money. To Herb for teaching me how to be a graduate student and readying me for the waiting challenges. To Nick Kotov for opening up his lab to me and making available all the sample used in this dissertation. To John Mansfield for introducing us to the electron microscopy community. To Bett and Linda for making the administrative stuff seem so simple.

To my brother Habib for always letting me get over and accepting me for what i try to be: a living version of your beautiful heart. I grew up trying to be just like you

but i haven't even come close; there's something old, wise, and beautiful about who you are. There is no limit to how much I love and admire you.

My dad Djibril, for your love and support and for sending me to this adventure well prepared with all the resources one can ever hope for. My mother Nancy, for setting the bar of beauty, intelligence and strength all bundle in one: only you know how to take my heart. I hope to be able to repay my parents the way they want me to.

To the rest of the family, there is no me without you: Marie (my only sister, my one and only love), Arfang, Babacar, Mohamed, Pap Samba, Albert, Mama (Malvinia Wyatt Blalock), Rhonda (for listening and all the great and invaluable advise), Aliou, Awa, Nancy, Malick, Nadia, Ndeye Fatou (I heard you are huge), Ablaye Ndiaye (Papi: I can't wait to know you better).

Last but not least: Fatou Kine for my behavior towards you, you'll never know how valuable you've been to me. I'm sorry you had to meet me during the worse times of my life. But the patience and love you showed me, gave me hope again and a whole new heart beating inside me. You are the one I've dreamt of so many times. My love for you is brand new and beautiful; it's good to feel this way again towards some one not related to me. Your place in definitely set on stone.

To all the rest of the extended family and close friends there are way too many of us to name but you are in my thoughts. I can never forget my uncle Moussa N'Diaye who left us way too soon; I remember trying to bend your toes I'm sure you would laugh hard at the memory I miss you. Marvin, big man, you to left too soon i still wish i had more time to know you better.

To all the members of our cool research group: Hyunyong, Jae Hyun, JingYong (for showing me the way laser experiments should be done), Dong Sun, Chuck, Yu Chong, Malakeh, Yunbo, Jessica, and Meredith; it was an enjoyable time.

TABLE OF CONTENTS

DEDICATION . . . . . **ii**

ACKNOWLEDGEMENTS . . . . . **iii**

LIST OF FIGURES . . . . . **vii**

CHAPTER

Introduction **1**

I. Metal Nanoparticles 6

1.1 Introduction 6
1.2 Plasmon Modes in Metals 7
1.2.1 Bulk Plasmon 9
1.2.2 Surface Plasmon 10
1.3 Spectral Properties of Spheroidal Metallic Nanoparticles 13
1.3.1 Optical Absorption for a Prolate Spheroid 14
1.3.2 Results and Discussion 21

II. Analytical Description of the Energy Loss Probability for Electron Passing by a Spheroid 26

2.1 Introduction 26
2.2 Theory 28
2.2.1 Coordinate System 28
2.2.2 Scalar Functions 30
2.2.3 Analytical Solution for the Energy Loss 33
2.3 Numerical Evaluation and Discussion 34

III. Single Particle Plasmon Spectroscopy of Gold Nanorods and Silver Nanowires 40

3.1 Introduction 40
3.2 Experiment 43
3.2.1 Synthesis of Gold Nanorods and Silver Nanowires 43
3.2.2 Electron Energy Loss Spectroscopy 45
3.3 Results and Discussion 50
3.4 Conclusion 62

IV. Electron Beam Mapping of Plasmon Resonances of Electromagnetically Coupled Gold Nanorods 64

4.1 Introduction 64

4.2 Experiment . . . 66
4.2.1 Synthesis of Gold Nanorods . . . 66
4.2.2 Energy Filtered Transmission Electron Microscopy . . . 67
4.3 Results and Discussion . . . 70
4.4 Conclusion . . . 76

V. Enhanced Surface Third Harmonic Generation from Gold Nanorods . . . 81

5.1 Introduction . . . 81
5.2 Third Harmonic Generation Using Focused Gaussian Beam . . . 83
5.3 Experiment . . . 85
5.3.1 Synthesis of Gold Nanorods . . . 87
5.3.2 Laser Systems . . . 89
5.4 Results . . . 93
5.5 Conclusion . . . 99

Conclusion and Future Work . . . **100**

BIBLIOGRAPHY . . . **107**

LIST OF FIGURES

Figure

1.1 Stained glass window at the Notre Dame cathedral in Paris 8

1.2 Geometry of two semi-infinite media with dielectric functions $\epsilon_1(\omega)$ and ϵ_2 separated by a planar interface at $z = 0$ 10

1.3 ellipsoidal particle 15

1.4 An overview of the different length and width Au nanorods present in a colloidal sample. The solution is mainly composed of different size nanorods. 22

1.5 Ensemble optical absorption spectrum of colloidal Au nanorods. The 1^{st} peak at 520nm is the main surface plasmon absorption of Au and the 2^{nd} is to the longitudinal absorption of the nanorods, the observed broadening is due to the polydispersity of the sample. 23

1.6 Simulation of the surface plasmon absorption of Au nanorods with varying aspect ratio, the medium dielectric cosntant ϵ_m is set to 1. This shows the dependence of the longitudinal plasmon to the particle aspect ratio 24

1.7 Calculated absorption spectra of a Au nanorod with aspect ratio $\rho = 4$, with varying dielectric constant ϵ_m 25

2.1 A spheroid is a quadric surface in three dimensions obtained by rotating an ellipse about one of its principal axes. Three particular cases of a spheroid are: 1) the ellipse is rotated about its major axis, the surface is a prolate spheroid; 2) the ellipse is rotated about its minor axis, the surface is an oblate spheroid. 28

2.2 representation of the geometry under study: an electron is moving in vacuum with constant velocity and impact parameter b. The homogeneous prolate spheroid is described by a frequency dependent dielectric function $\epsilon(\omega)$ 31

2.3 energy loss probability vs energy for 50 keV electrons incident a different impact parameter ($\frac{b}{a} = 1.05, 1.15, 1.3$) on a Ag prolate spheroid. 36

2.4 energy loss probability vs energy for 50 keV electrons with impact parameter ($\frac{b}{a} = 1.05$) incident on three different Ag prolate spheroid of different shape ($\eta_o = 0.38, 0.45, 0.58$), see equation (2.28). 37

2.5 energy loss probability vs energy for 50 keV electrons at different impact parameter ($\frac{b}{a} = 1.05$) on a two different Ag prolate spheroid of equal shape ($\rho = 4$) and different size ($a = 10, 30$). 38

2.6 energy loss probability vs energy for Ag prolate spheroid with ($\eta_o = 0.3$) at impact parameter ($\frac{b}{a} = 1.05$) and size ($a = 10$). Shown are results for 3 different incident energies ($E = 5, 10$, and $50KeV$). 39

3.1 TEM images of 4.6 aspect ratio gold nanorods 44

3.2 Ensemble optical absorption spectrum of solution. The 1^{st} peak at 520nm is the main surface plasmon absorption of Au and the 2^{nd} is to the longitudinal absorption of the nanorods, the observed broadening is due to the polydispersity of the sample. 45

3.3 SEM images of silver nanowires 46

3.4 (a) Ensemble optical absorption spectrum of Ag nanowires in solution; the peak at 3.5eV is due to the transverse plasmon absorption. The broad peak is due to longitudinal plasmon absorption; the broadening is due to contributions from different length and width nanowires present in the solution. 47

3.5 A typical electron energy loss spectrum scheme is shown. The electrons are collected through a spectrometer to show their energy distribution following their interaction with the sample. 48

3.6 A typical electron energy loss spectrum is shown displaying the peaks of interest: the zero loss peak and the plasmon peak 49

3.7 TEM images of Ag nanowires of length 706 nm and width 50 nm 51

3.8 deconvoluted spectrum acquired from the edge of the particle. Two peaks are clearly resolved, the transverse mode is at 3.54 eV and longitudinal mode is at 1.8 eV. 52

3.9 (a) Ensemble optical absorption spectrum of Ag nanowires in solution; the peak at 3.5eV is due to the transverse plasmon absorption. The broad peak is due to longitudinal plasmon absorption; the broadening is due to contributions from different length and width nanowires present in the solution. 53

3.10 Deconvoluted spectra of four different length Ag wires with an average diameter of $\sim$ 50 nm: the transverse plasmon resonance is relatively consistent (3.4 to 3.6 eV); the slight peak variations can be largely attributed to wire thickness and film support. The longitudinal plasmon peak is red shifted as the wire length increases confirming its dependence on the particle aspect ratio. 54

3.11 An overview of the different size and shape Au nanorods present in the sample. The solution is mainly composed of different size nanorods. 55

3.12 Ensemble optical absorption spectrum of solution. The 1^{st} peak at 520nm is the main surface plasmon absorption of Au and the 2^{nd} is to the longitudinal absorption of the nanorods, the observed broadening is due to the polydispersity of the sample. 56

3.13 (a) TEM image of a single Au rod 40nm long and 10nm wide with electron beam position indicated by the small red circle a the tip of the particle. 58

3.14 deconvoluted Spectrum of a single nanorod. Both plasmon peaks are resolved: the longitudinal plasmon peak is at 1.74 eV and the transverse peak is at 2.47 eV. . . . 59

3.15 Two nanorods (dipole) positioned with a 10-nm gap. 60

3.16 Deconvoluted spectra of the dipole taken at the edge and in the gap between the two rods along with that of the single nanorod fig 3.14. The plasmon peak at the edge of the dipole is 1.62 eV and 1.72 eV in the gap both peaks are red shifted compared to the single rod plasmon peak but the shift is smaller for excitation in the gap. 61

3.17 Comparison between analytical representations of the energy loss peak for 3 Au prolate spheroids. For all expressions we set the host dielectric $\epsilon_m = 1$ and the damping coefficient for the Drude model for dielectric $\gamma = 1.06$. The aspect ratio ρ is varied to show its influence on the plasmon peak absorption. 63

4.1 TEM images of 4.6 aspect ratio gold nanorods 67

4.2 Ensemble UV-Vis absorption spectrum of Au nanorod solution. The first peak at 520 nm ($\sim 2.4eV$) is the main surface plasmon absorption of Au and the second is to the longitudinal absorption of the nanorods. The observed broadening is due to the polydispersity of the sample. 68

4.3 single Au nanorod with aspect ratio of ~ 3 70

4.4 Dimer 1; pair of identical nanorod forming an angle dipole with a gap ~ 10 nm. . . 71

4.5 Dimer 2; angle dipole with separation ~ 1 nm. 71

4.6 energy loss spectrum of a single Au nanorod the transverse peak is at 2.4 eV and the longitudinal peak is at 1.8 eV. 72

4.7 the electron loss spectra of coupled nanorods compared to the single nanoparticle spectrum. The dipole formations show a significant redshift of the longitudinal plasmon peak and a larger number of electron count largely attributed to high concentration of fields at the gap; confirming the large field enhancement at the dipole gap. 73

4.8 (a) EFTEM spectral map of the spatial variation of the longitudinal plasmon at 1.9 eV (corresponding to optical transition wavelength of ∼650nm) and the transverse plasmon 2.4 eV (520nm). (b) Theoretical distribution of the electromagnetic field around a single particle at 1.9 eV (650 nm) for the longitudinal plasmon and the transverse plasmon at 2.4 eV (520 nm). 77

4.9 map of spatial mode of the longitudinal (1.4 eV) and transverse (2.2 eV) plasmon of a pair of Au nanorods at close proximity with a 5 nm gap. (b) Theoretical distribution of the longitudinal plasmon around the pair of Au nanorods. 78

4.10 comparison of the decay of surface plasmon intensity of the experimental EELS data and the optical calculations obtained using the DDA method. The intensity decay is measured along the symmetric axis of the Au nanorod 79

4.11 Sketch to illustrate the induced spatial charge structure between closely spaced nanoparticles, when exposed to an electron beam 79

4.12 Spectra collected at the edge and gap of two nanorods at close proximity. This measurement also shows that the electron beam can induce charge displacement along one axis at a time, as it is demonstrated here for the longitudinal axis 80

5.1 log-log plot of the Excitation power dependence of the measured THG signal measured over a single point within the scanned sample area: the surface of the sapphire substrate containing the Au nanorods 86

5.2 Experimental arrangement for third harmonic generation in transmission at the interface of a sapphire substrate and air 87

5.3 TEM image of an overview of the different size and shape Au nanorods present in the sample. 88

5.4 Ensemble optical absorption spectrum of solution. The 1^{st} peak at 520nm is the main surface plasmon absorption of Au and the 2^{nd} is to the longitudinal absorption of the nanorods, the observed broadening is due to the polydispersity of the sample. 89

5.5 Ti:Sapphire Oscillator. 90

5.6 Ti:Sapphire Regenerative Amplifier. 92

5.7 Different size and shape nanoparticle present in solution have different absorption spectra that add up to give the broad UV-Vis spectrum. The small peak at 520 nm is due to the transverse absorption of the spheroidal particles and the broad peak is the longitudinal absorption due different length particle in the solution. . . 95

5.8 Area scanned with a circularly polarized light. Intensity graphs of THG 2-D scan of sample area. View of along the x (horizontal) axis and the z (vertical) axis with 1 μm steps in both directions. The lighter color represent the intensity of the THG signal in linear scale. High intensity signal is generated when we scan over a nanorod. The bright red dots represent the highest enhancement obtained 96

5.9 Area 2-D scan with a vertically polarized light. View of along the x (horizontal) axis and the z (vertical) axis with 1 μm steps in both directions. 96

5.10 Area 2-D scan with a horizontally polarized light. View of along the x (horizontal) axis and the z (vertical) axis with 1 μm steps in both directions. 97

5.11 optical absorption spectrum of the sample of laser irradiation, obtained by excitation using a coherent light source. 98

5.12 SEM image of parts of the sample area after laser (THG) irradiation; it shows that the area still contains Au rod of different shape and size 99

Introduction

This thesis reflects the results of four years of research at the center for ultrafast optical sciences (CUOS) at the University of Michigan – Ann Arbor on the investigation of the electromagnetic properties of noble metal nanostructures.

Nanostructures are the building block of plasmonics, a field of nanotechnology in which research is taking place at a breathtaking pace. They are the product of advances in nanofabrication: self assembly based on wet chemistry and electron beam lithography. Nanostructures are however much more than just a miniaturizing process, they hold the secret to developing novel materials and novel devices that can perform tasks that cannot be achieved with conventional techniques. This is added to the promise of making things faster, with less heat generation, and with less power consumption. But arguably, one of the most promising and exciting problem is optical subwavelength imaging. Conventional optics does not allow sub wavelength imaging according to the more than 100 years old Rayleigh limit. In spite of this limit, nanostructures have become instrumental in imaging objects several order of magnitude smaller than the wavelength of visible light. These unusual attributes stem from the change in optical properties of noble metals when reduced to small sizes. The change in color of gold for example, when it is divided into extremely small or colloidal particles is probably the first ever reported effect which can be re-

lated to nanotechnology. Initiated by the work of Faraday [1] and even much earlier such properties/effects have been exploited to staining glasses; e.g. in churches and cathedrals.

Indeed, the optical properties of noble metal material (gold, silver) exhibit striking differences relatives to their bulk and thin film responses, as their sizes approach the nanoscale. The interesting and sometimes unexpected properties of nanoparticles are partly due to the aspects of the surface of the material dominating the properties in lieu of the bulk properties.

When light shines on a metal nanoparticles (i.e. one smaller than the wavelength of light), the alternating electric field associated with the optical wave causes the surface charges to slosh back and forth along an axis of the nanoparticle. The natural oscillation frequency of the collective motion of the electron in the metal is known as the plasma frequency, the electromagnetic mode corresponding to this oscillation is a surface plasmon. This light matter interaction leads to strongly enhanced optical fields of sub-wavelength dimensions. These intense fields or surface plasmons are indeed, confined within a few nanometers from the surface of nanoparticles; it is at this juncture or region of near fields that most plasmonic research is focused.

Surface plasmon frequencies are typically in the visible or near infrared part of the electromagnetic spectrum. For this reason, optical spectroscopy techniques have been the primary methods for investigating nanoparticles samples. However these techniques, aside from being extremely challenging, are limited in their ability to characterize single nanostructures. These limitations are the driving force behind the search for alternate methods, which have lead us to look in to electron mi-

croscopy.

Electron energy loss spectroscopy (EELS) in the transmission electron microscope (TEM) involves analyzing the energy of initially mono-energetic electrons after they have interacted with a specimen. This method has been routinely used for many years to study the bulk plasmon loss in thin metallic film and clusters for energies up to many electron-volts (eV). But for a long time optical spectroscopy and EELS have remained quite separate because they dwell in different energy range. Now, with the recent emergence of monochromatic electron beams and improved energy detection, EELS is routinely producing examples of surface plasmon characterization in single nanostructures at spatial resolution of a nanometre or better and energies as low as 1 eV well into the optical regime. Consequently, this method of characterization is now emerging as an important tool in the study the optical properties of noble metal nanostructures.

The primary goal of this thesis is to show that EELS is a viable tool to describe the optical properties of nanostructures. In that process, it also establishes a relationship or rather bridges a gap between optical spectroscopy and EELS. This is accomplished through a comparative study of EELS measurement and optical spectroscopy of single and closely spaced nanostructures, with the intent of showing that both techniques are required to access a full description of their dielectric function. The dielectric function provides a complete characterization of the interaction of a material with the electromagnetic field. Thus, fine details are needed to access the fundamental properties of the metal and the designed geometries of the structural

units for the functionality of the nanostructures.

The first two chapters of the text, set the groundwork by deriving the optical absorption of ellipsoidal metallic nanoparticles excited by either an external electromagnetic field or induced by a fast moving electron. Chapter I gives a short background on surface plasmon resonances, by describing the optical properties of metals, starting with Maxwells equations and the derivation of the dielectric function of the free electron gas. It concludes with a discussion of the analytical expression of the optical absorption of a prolate spheroid. Chapter II gives a mathematical description of the interaction between a moving charged particle and a metallic prolate spheroid. The experimental EELS measurements of single and paired nanostructures are given in chapters III and IV. In chapter III the relation between energy-loss measurements and optical spectroscopy of a single nanoparticle plasmon modes is discussed, and in chapter IV the spatial modes of isolated and paired nanoparticles are shown to have strong similarities to that of electromagnetic fields distribution around gold nanorods induced by optical excitation simulated using the discrete dipole approximation method.

Finally, chapter V makes use of the ability of these nanoparticles to enhance electromagnetic fields to intensify surface third harmonic generation (THG). THG has been proposed as a method to observe transparent objects through variations in their nonlinear properties; third-order nonlinear effects and specifically third harmonic generation are particularly suitable for this purpose since all materials have nonvanishing third-order coefficient. However, it is a generally weak signal inciting a need for enhancement to increase the yield in non linear microscopy.

This work has been a collaborative effort that has brought together different disciplines that have evolved separately for many years. The nanoparticles samples have been assembled by Dr Kotov's group in the chemical engineering department at the University of Michigan in Ann Arbor (U of M). The EELS measurements have been initiated at the Electron Microbeam Analysis Laboratory (EMAL) at U of M. However, measurements requiring higher energy resolution samples have been achieved at Argonne national laboratory (ANL), the Ohio State University Fontana Laboratory, and the national center for electron microscopy (NCEM) at Lawrence Berkeley Laboratory (LBL). The discrete dipole approximations (DDA) calculations have been completed at the department of Chemistry in Northwestern University in Evanston, IL.

CHAPTER I

Metal Nanoparticles

1.1 Introduction

The electronic properties of noble metal materials change drastically as a consequence of reducing their size and dimensionality to nanoscale proportions. The density of states and spatial length scale of the electronic motion are reduced with decreasing size, the energy eigenvalue are now determined by the system's boundaries thus surface effect become very important [2, 3].

Metallic nanoparticles have the ability to sustain coherent electron oscillations known as surface plasmon (SP) leading to electromagnetic fields confined to their surface. The formation of SP are due to the electric field of an incoming radiation that induces the formation of a dipole or a polarization of charges on the nanoparticle surface. These charges act as an effective restoring force for charge neutrality allowing for a resonance to occur at a specific frequency. For noble metal nanoparticles (Ag, Au, Cu), this resonance frequency is in the visible part of electromagnetic spectrum. This gives rise to fascinating colours that have been used long before the advent of nanotechnology, as we can see in the beautiful stained glasses of many churches as

figure 1.1 shows, dating back in the 17^{th} century.

These optical properties have attracted a large amount of work pioneered by the work of Mie [4] Gans [5]. Mie first described these phenomena theoretically by solving Maxwell's equation for the absorption and scattering of a radiation field interacting with a spherical metal particle under the appropriate boundary conditions. His theory has found wide applicability since then because it allows the calculations of the particle extinction spectra, as long as the material dielectric function is known and the size is smaller than the wavelength of light [6, 7].

In this chapter, we set the groundwork by describing the optical properties of metals by giving the dielectric function of the free electron gas. We define the different plasmon modes present in nanoparticles, then we describe the spectral properties of spheroidal metallic nanoparticles in particular Au nanorods. We also derive the size and shape dependent plasmon absorption of these particles.

1.2 Plasmon Modes in Metals

Metals are defined by their quasi free electrons in the ground state, which are not bound to single atoms but to the metal bulk. These free electron are responsible for the well known properties of high electric conductivity, and high optical reflectivity. The physical origin of light absorption by metallic nanoparticles is the coherent oscillation of these conduction band electrons induced by the interacting field [3, 7]. These electrons are commonly described collectively as a plasma with density N_e, which means that the free electron of a metal are treated as an electron liquid of high density. A plasma is a medium with equal concentration of positive and negative

Figure 1.1: Stained glass window at the Notre Dame cathedral in Paris

charges, of which at least one charge type is mobile. In a metal the negative charges of the condution electrons are balanced by an equal concentration of positive charges of the ion core [8]. Plasma waves are longitudinal electromagnetic charge density waves and their quanta are referred to as plasmons [3, 6, 7]. They exist in two forms: bulk plasmon in the volume of a plasma and surface plasmons, which are bound to the interface of a plasma and a dielectric [9]. Surface plasmons exist for metals like Au, Ag, Al, and Cu from DC to optical and near UV frequencies, depending on the dielectric function of both the metal and the neighboring dielectric.

1.2.1 Bulk Plasmon

The Bulk plasmon denotes a collective excitation of the dense electron gas in the bulk of the metal. It is a longitudinal dielectric response $\epsilon(\omega)$ of an electron gas obtained from the equation of a free electron in an electric field E :

$$m\frac{d^2x}{dt^2} = -eE \tag{1.1}$$

if x and E have the time dependence $e^{-i\omega t}$, then $x = \frac{eE}{m\omega^2}$. The dipole moment of one electron is $-ex = \frac{e^2E}{m\omega^2}$, and the polarization P, define as the dipole moment per unit volume is:

$$P = -nex = -\frac{ne^2E}{m\omega^2}, \tag{1.2}$$

where n is the electron concentration.

The dielectric function at frequency ω is [10]:

$$\epsilon(\omega) = 1 + \frac{P(\omega)}{\epsilon_o E(\omega)} \tag{1.3}$$

and the dielectric function of the free electron gas follow from (1.2) and (1.3):

$$\epsilon(\omega) = 1 - \frac{ne^2}{\epsilon_o m\omega^2} \tag{1.4}$$

the plasma frequency ω_p is defined by the relation

$$\omega_p^2 = \frac{ne^2}{\epsilon_o m} \tag{1.5}$$

The dielectric function (1.4) can now be written as:

$$\epsilon(\omega) = 1 - \frac{\omega_p^2}{\omega^2} \tag{1.6}$$

Bulk plasmons show a material dependent resonance frequency in the form of the plasma frequency expressed in (1.5).

These resonant frequency are generally excited by shooting fast electrons through a thin film and observing the losses suffered by the electrons [11].

1.2.2 Surface Plasmon

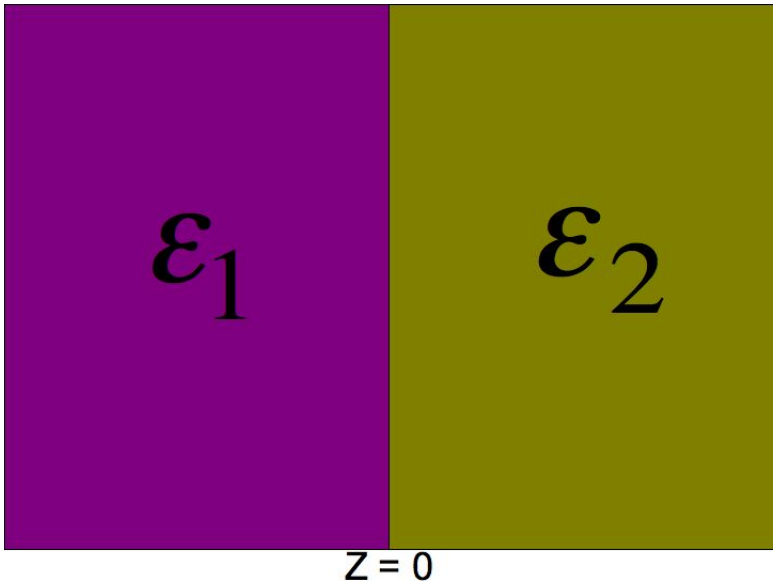

Figure 1.2: Geometry of two semi-infinite media with dielectric functions $\epsilon_1(\omega)$ and ϵ_2 separated by a planar interface at $z = 0$

Surface plasmons, also known as surface plasmon polaritons, are surface electromagnetic waves that propagate in a direction parallel to the metal/dielectric (or metal/vacuum) interface. Since the wave is on the boundary of the metal and the external medium (air or water for example), these oscillations are very sensitive to any change of this boundary, such as the adsorption of molecules to the metal surface.

We consider the simplest geometry consisting of two semi infinite non magnetic media, the first with a positive real dielectric ϵ_2 adjacent to a metallic/conducting media with a frequency dependent dielectric function $\epsilon_1(\omega)$, separated by a planar interface at $z = 0$ see figure 1.2. The full set of Maxwell's equations in the absence of external field can be expressed as follow [10]:

$$\nabla \times H_i = \epsilon_i \frac{1}{c} \frac{\partial}{\partial t} E_i \tag{1.7}$$

$$\nabla \times E_i = -\frac{1}{c} \frac{\partial}{\partial t} H_i \tag{1.8}$$

$$\nabla \cdot (\epsilon_i E_i) = 0 \tag{1.9}$$

$$\nabla \cdot H_i = 0 \tag{1.10}$$

where the index i describes the media: $i = 1$ at $z < 0$, and $i = 2$ at $z > 0$. We are solving for the propagating wave confined to the interface, with evanescent waves decaying in the perpendicular z-direction. Solutions to equations 1.7–1.10 can generally be classified into s-polarized and p-polarized electromagnetic modes. For an ideal surface, if waves are to be formed that propagate along the interface there must necessarily be a component of the electric field normal to the surface [12]. Choosing the x-axis along the propagating direction we write:

$$E_i = (E_{i_x}, 0, E_{i_z}) e^{-k_i |z|} e^{i(\beta_i x - \omega t)} \tag{1.11}$$

and

$$H_i = (0, E_{i_y}, 0) e^{-k_i |z|} e^{i(\beta_i x - \omega t)} \tag{1.12}$$

where β_i represents the magnitude of the wave vector parallel to the interface. In-

troducing equations 1.11 and 1.12 into equations 1.7–1.10, we find:

$$ik_1 H_{1_y} = \frac{\omega}{c}\epsilon_1 E_{1_x}, \tag{1.13}$$

$$ik_2 H_{2_y} = \frac{\omega}{c}\epsilon_1 E_{2_x} \tag{1.14}$$

and

$$k_i = \sqrt{\beta_i^2 - \epsilon_i \frac{\omega^2}{c^2}} \tag{1.15}$$

The boundary conditions imply that the component of the electric and magnetic fields parallel to the surface must be continuous. Using equations 1.13 and 1.14, one writes the following system of equations:

$$\frac{k_1}{\epsilon_1} H_{1_y} + \frac{k_2}{\epsilon_2} H_{2_y} \tag{1.16}$$

and

$$H_{1_y} - H_{2_y} = 0 \tag{1.17}$$

which has solution only if the determinant is zero, i.e.

$$\frac{\epsilon_1}{k_1} + \frac{\epsilon_2}{k_2} = 0 \tag{1.18}$$

This is the so called surface plasmon condition [11, 12, 13].

From the boundary conditions also follows the continuity of the wave vector $\vec{\beta}$ such that $\beta_1 = \beta_2 = \beta$. Making use of equations 1.15 and 1.18, we can also express the surface plasmon condition as follow:

$$\beta(\omega) = \frac{\omega}{c}\sqrt{\frac{\epsilon_1 \epsilon_2}{\epsilon_1 + \epsilon_2}} \tag{1.19}$$

This expression is valid for both real and complex ϵ_1, i.e. for conductors with and without attenuator [13]. The surface plasmon frequency is obtained by inserting the free electron dielectric function 1.4 into equation 1.19 to obtain:

$$\omega_{sp} = \frac{\omega_p}{\sqrt{1+\epsilon_2}} \tag{1.20}$$

this implies that there is negligible damping of the conduction electrons oscillation, the wave vector β goes to infinity as the frequency approaches ω_{sp}, the group velocity goes to zero. The mode thus acquires electrostatic character, and is known as the surface plasmon [13].

1.3 Spectral Properties of Spheroidal Metallic Nanoparticles

Accelerated electric charges due to an external electric field, radiate electromagnetic energy in all direction; it is this secondary radiation that is called the scattered field. In addition, the excited charges may transform part of the incident electromagnetic energy into other forms, a process called absorption . Scattering and absorption are not mutually independent processes. Often when these processes are referred to as scattering when absorption is meant as well [6]. Both processes occur simultaneously, their combined effect are termed "extinction" defined as the attenuation of an electromagnetic field as it traverses a particulate medium [7]. There are instances where one of the processes is dominant. For example, visible light passing through a fog is almost entirely scattered, whereas light passing along a shaft of a coal mine might be attenuated primarily by absorption. Absorption is usually the dominant attenuation mechanism in homogeneous media [6].

Mie [4] is the first to theoretically describe the absorption of spherical Au particles

with sizes below the resolution limit of light and to show that they display a strong absorption band in the visible region of the electromagnetic spectrum at about 520 nm, called the plasmon absorption [6, 14]. This theory is extended to prolate and oblate spheroid by Gans [5].

The Au nanorods and Ag nanowires we are interested in can be accurately modeled as prolate spheroids [3, 15, 16]. Spheroidal nanoparticles have two plasmon resonance absorptions, one due to the transverse oscillation of electrons around 520 nm for Au and $\sim$ 350 nm for Ag, regardless of particle size. The other absorption is much stronger and is due to the longitudinal oscillation of the electrons. Its wavelength maximum is redshifted with respect to the transverse plasmon and depends on the aspect ratio (ρ), defined as the length divided by the width of the nanoparticle.

1.3.1 Optical Absorption for a Prolate Spheroid

A theoretical description of particle plasmons involves analyzing the interaction of a sub-wavelength metal particle with an electromagnetic field using the electrostatic approximation. Indeed, if the particle is much smaller than the wavelength of light, the oscillating electromagnetic field is practically constant over the particle volume, so that we can calculate the spatial field distribution assuming the simplified problem of a particle in an electrostatic field [6, 10, 13].

Following the treatment of Bohren *et al* [6], we derive the field distribution of an ellipsoidal particle (figure 1.3), which is the most general smooth particle (one without edges or corners), then we extract the fields for spheroidal particles which are a special class of ellipsoids.

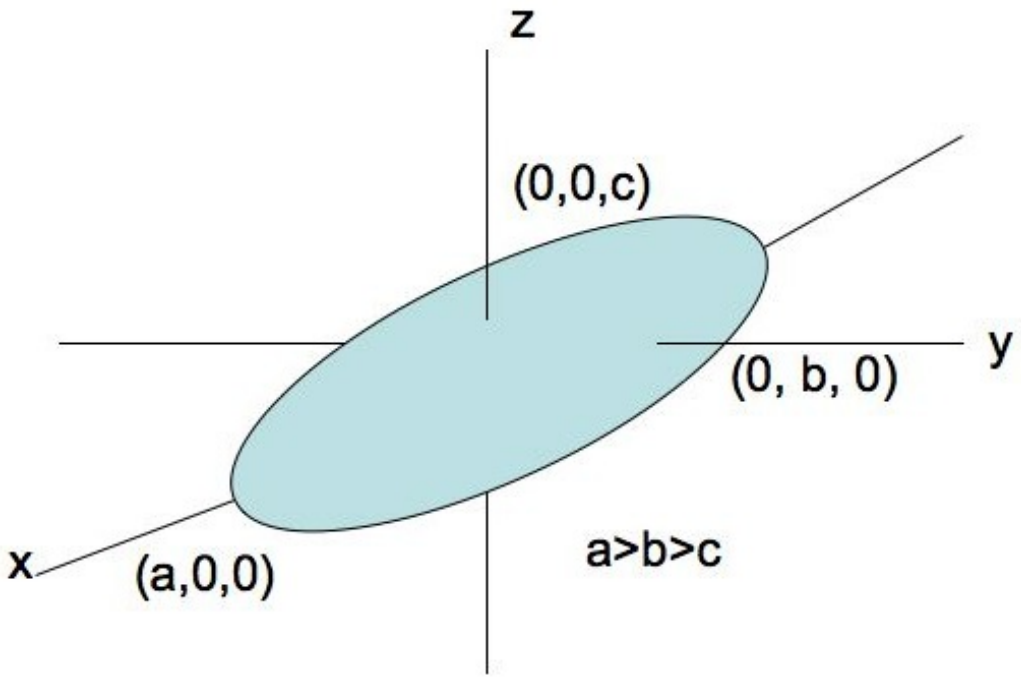

Figure 1.3: ellipsoidal particle

In the electrostatic approximation, it is shown that the scatterer, the ellipsoid in our case, is equivalent to an ideal dipole with dipole moment:

$$\vec{p} = \epsilon_m \alpha E_o e^{-i\omega t} \hat{e}_r \tag{1.21}$$

of an ideal dipole illuminated by an $\vec{r}$ polarized plane wave $E_o e^{\vec{k}.\vec{r}-i\omega t}\hat{e}_r$, where ϵ_m is the medium dielectric function and α is the polarrizablity defined as the ease with which the scatterer is polarized [10]. The dipole moment oscillates with the frequency ω of the applied field. The absorption and scattering cross section of a small particle

in the electrostatic approximation is defined as:

$$C_{abs} \sim Im(\alpha) \tag{1.22}$$

$$C_{sca} \sim |\alpha^2| \tag{1.23}$$

We start with an ellipsoid with semi-axes $a > b > c$ shown in figure 1.3, the surface of which is defined by:

$$\frac{x^2}{a^2} + \frac{y^2}{b^2} + \frac{z^2}{c^2} = 1. \tag{1.24}$$

To determine the dipole moment of an ellipsoidal particle induced by a uniform electrostatic field, the ellipsoidal coordinates (ξ, η, ζ) are use, they are defined by:

$$\begin{aligned}
\frac{x^2}{a^2+\xi} + \frac{y^2}{b^2+\xi} + \frac{z^2}{c^2+\xi} &= 1, \qquad -c^2 < \xi < \infty \\
\frac{x^2}{a^2+\eta} + \frac{y^2}{b^2+\eta} + \frac{z^2}{c^2+\eta} &= 1, \qquad -b^2 < \eta < -c^2 \\
\frac{x^2}{a^2+\zeta} + \frac{y^2}{b^2+\zeta} + \frac{z^2}{c^2+\zeta} &= 1, \qquad -a^2 < \zeta < -b^2
\end{aligned}$$

Conversely we can write the coordinates (x, y, z) as functions of (ξ, η, ζ) as:

$$\begin{aligned}
x^2 &= \frac{(a^2+\xi)(a^2+\eta)(a^2+\zeta)}{(b^2-a^2)(c^2-a^2)} \\
y^2 &= \frac{(b^2+\xi)(b^2+\eta)(b^2+\zeta)}{(a^2-b^2)(c^2-b^2)} \\
z^2 &= \frac{(c^2+\xi)(c^2+\eta)(c^2+\zeta)}{(a^2-c^2)(b^2-c^2)}
\end{aligned}$$

In a uniform electrostatic field aligned along the z axis, the potential Φ has the symmetry properties:

$$\Phi(x, y, z) = \Phi(-x, y, z) = \Phi(x, -y, z) = \Phi(-x, -y, z) \tag{1.25}$$

$$\Phi(x, y, -z) = \Phi(-x, y, -z) = \Phi(x, -y, -z) = \Phi(-x, -y, -z) \tag{1.26}$$

where x, y, z are positive. Thus only the potential in two octants is considered: one with positive z and one with negative z. The potential and its derivative are required to be continuous on the plane $z = 0$.

Let us consider the octant in which x, y, z are positive. We set Φ_1 as the potential induced inside the particle; outside the particle the potential Φ_2 may be written as the superposition of the potential Φ_o and the perturbing potential Φ_p caused by the particle, where Φ_o is:

$$\Phi_o = -E_o z = -E_o \left[\frac{(c^2+\xi)(c^2+\eta)(c^2+\zeta)}{(a^2-c^2)(b^2-c^2)} \right] \tag{1.27}$$

noting that at sufficiently large distances the perturbing potential is negligible.

Laplace's equation in ellipsoidal coordinates is:

(1.28)

$$\nabla^2\Phi = (\eta-\zeta)f(\xi)\frac{\partial}{\partial\xi}\left\{ f(\xi)\frac{\partial\Phi}{\partial\xi} \right\} + (\zeta-\xi)f(\eta)\frac{\partial}{\partial\eta}\left\{ f(\eta)\frac{\partial\Phi}{\partial\eta} \right\} + (\xi-\eta)f(\zeta)\frac{\partial}{\partial\zeta}\left\{ f(\zeta)\frac{\partial\Phi}{\partial\zeta} \right\}$$

where $f(q) = \big\{(q+a^2)(q+b^2)(q+c^2)\big\}$. We'll follow the procedure developed by Bohren[6] [page 143 - 147]. It is postulated that the potentials Φ_1 and Φ_p are of the form:

$$\Phi(\xi,\eta,\zeta) = F(\xi)\big\{(c^2+\eta)(c^2+\zeta)\big\}^{\frac{1}{2}},$$

where it follows from (1.28) that $F(\xi)$ satisfies the ordinary differential equation:

$$f(\xi)\frac{d}{d\xi}\left\{ f(\xi)\frac{dF}{d\xi} \right\} - \left(\frac{a^2+b^2}{4} \right) F(\xi) = 0. \tag{1.29}$$

One solution is:

$$F_1(\xi) = (c^2+\xi)^{\frac{1}{2}} \tag{1.30}$$

a second linearly independent solution for to (1.29) may be obtained by integrating F_1:

$$F_2(\xi) = F_1(\xi) \int_\xi^\infty \frac{dq}{F_1^2(q) f(q)} \tag{1.31}$$

with the property $\lim_{\xi\to\infty} F_2(\xi) = 0$. The function F_1 is not compatible with the requirement that:

$$\lim_{\xi\to\infty} \Phi_p = 0; \tag{1.32}$$

therefore, the perturbing potential of the particle is:

$$\Phi_p(\xi,\eta,\zeta) = C_2 F_2(\xi)\big\{(c^2+\eta)(c^2+\zeta)\big\}^{\frac{1}{2}}, \tag{1.33}$$

where C_2 is a constant. If the potential inside is to be finite at the origin, we must have:

$$\Phi_1(\xi,\eta,\zeta) = C_1 F_1(\xi)\big\{(c^2+\eta)(c^2+\zeta)\big\}^{\frac{1}{2}}, \tag{1.34}$$

where C_1 is a constant. Thus, the field inside the particle is uniform and parallel to the applied field. The boundary condition is defined above and the requirement that the normal component of $\vec{D}$ be continuous at the boundary between particle and medium yields equations to determine C_1 and C_2. We then obtain the potentials inside and outside the particle:

$$\Phi_1 = \frac{\Phi_o}{1 + \frac{L_3(\epsilon_1-\epsilon_m)}{\epsilon_m}} \tag{1.35}$$

$$\Phi_p = \Phi_o \frac{\frac{abc}{2}\frac{\epsilon_1-\epsilon_m}{\epsilon_m}\int_\xi^\infty \frac{dq}{(c^2+q)f(q)}}{1 + \frac{L_3(\epsilon_1-\epsilon_m)}{\epsilon_m}} \tag{1.36}$$

where

$$L_3 = \frac{abc}{2}\int_0^\infty \frac{dq}{(c^2+q)f(q)}$$

At distances r from the origin which are much greater that the largest semiaxis a, the potential Φ_p is given asymptotically by:

$$\Phi_p \sim \frac{E_o \cos\theta}{r^2} \frac{\frac{abc}{3}\frac{\epsilon_1-\epsilon_m}{\epsilon_m}}{1+\frac{L_3(\epsilon_1-\epsilon_m)}{\epsilon_m}}, \qquad (r \gg a)$$

which is recognized as the potential of a dipole with moment:

$$\vec{p} = 4\pi\epsilon_m abc \frac{\epsilon_1-\epsilon_m}{3\epsilon_m + 3L_3(\epsilon_1-\epsilon_m)} \vec{E}_o.$$

Therefore, the polarizability α_3 of an ellipsoid in a field parallel to one of its principal axes is:

$$\alpha_3 = 4\pi abc \frac{\epsilon_1-\epsilon_m}{3\epsilon_m + 3L_3(\epsilon_1-\epsilon_m)} \tag{1.37}$$

The applied field could have been picked to be parallel to any of the other principle axes. Therefore the polarizability α_1 and α_2 when the applied field is parallel to the x and the y axes respectively, are:

$$\alpha_1 = 4\pi abc \frac{\epsilon_1-\epsilon_m}{3\epsilon_m + 3L_1(\epsilon_1-\epsilon_m)}$$
$$\alpha_2 = 4\pi abc \frac{\epsilon_1-\epsilon_m}{3\epsilon_m + 3L_2(\epsilon_1-\epsilon_m)}$$

where

$$L_1 = \frac{abc}{2}\int_0^\infty \frac{dq}{(a^2+q)f(q)}$$
$$L_2 = \frac{abc}{2}\int_0^\infty \frac{dq}{(b^2+q)f(q)}$$

where L_1, L_2, and L_3 are called the geometrical factors. To check these results, we mention the example of a sphere which is a special ellipsoid with $a = b = c$; therefore,

$$L_1 = L_2 = L_3 = \frac{a^3}{2}\int_0^\infty \frac{dq}{(a^2+q)^{\frac{5}{2}}} = \frac{1}{3},$$

and the polarizabilities reduce to that of a sphere $\big($see Bohren [6] page 139 equation (5.15)$\big)$.

The prolate spheroid is a special class of ellipsoid, which has two axes of equal length ($b = c$), thus only one of the geometrical factor is independent or ($L_2 = L_3$), it has the following analytical expression for L_1 as a function of the eccentricity e:

$$L_1 = \frac{1-e^2}{e^2}\left(-1 + \frac{1}{2e}\ln\frac{1+e}{1-e}\right) \qquad e^2 = 1 - \frac{b^2}{a^2}, \tag{1.38}$$

The focus of our work is on the plasmon absorption on the long axis of the prolate particle hence L_3. The geometrical factor for the remaining axes can be obtained easily from the relationship:

$$L_1 + L_2 + L_3 = 1.$$

For a generalized prolate particle of volume V, the dielectric function is defined as: $\epsilon_p(\omega) = \epsilon'(\omega) + i\epsilon''(\omega)$. We assume it to be dispersed in a non-absorbing medium with dielectric ϵ_m, the expression for the polarizability $\alpha(\omega)$ is:

$$\alpha(\omega) = \sum_{n=1}^{2} \frac{V\epsilon_m^{\frac{3}{2}}}{GL_n^2} \frac{\omega\epsilon''}{\left\{\epsilon' + \frac{1-L_n}{L_n}\epsilon_m\right\}^2 + (\epsilon'')^2} \tag{1.39}$$

where G is the particle cross-sectional projected onto a plane that is perpendicular to the incident radiation, and L_n are the geometrical factors for the transverse or longitudinal axes of the particle.

We derive the dielectric function for prolate particle using the relation $\epsilon = 1 + \chi$ where χ is the electric susceptibility of the medium and making use of equation (1.21), we deduce that the dielectric function of a prolate spheroid can be expressed as:

$$\epsilon_p \sim 1 + \alpha, \tag{1.40}$$

1.3.2 Results and Discussion

The geometrical factor L_n (where $n = 1$, 2, or 3) in equation 1.37 for the polarizability of the prolate particle contains the size and shape dependence of the plasmon absorption. As stated above we are interested in Au nanorods which are modeled as prolate spheroids [15, 16, 17, 18].

Thus the plasmon absorption for Au nanorods splits into two bands [3] corresponding to oscillation along and perpendicular to the long axis of the particle. The transverse mode shows a resonance at about 2.4 eV (520 nm), which is coincident to the plasmon resonance of spherical particles, while the resonance of the longitudinal mode is red shifted with respect to transverse plasmon, and strongly depends on the nanorod aspect ration ρ. We show a UV-Vis absorption spectrum of our sample of colloidal Au nanorods that clearly shows that the two plasmon peaks as displayed in figure 1.5. A TEM image of the corresponding nanorods is shown in figure 1.4. The average length is $\sim$ 40 to 50 nm and the average width is $\sim$ 10 to 15 nm.

The absorption spectra of Au nanorods with varying aspect ratio were calculated with the measured dielectric function of Au [19] using equation 1.39 and are shown in figure 1.6. The peak absorption for the longitudinal plasmon is red shisfted as the aspect ratio (ρ) is increased from 4 to 6. This result is in agreement with experimental results (see references [3, 15, 16] and references therein) for the dependence of the absorption maximum of the longitudinal plasmon resonance. This spectral position of the transverse mode maximum blue shits with increasing aspect ratio as demonstrated experimentally by Martin et al [20]. We also note that the experimental spectrum has a longitudinal peak much broader that the simulated one. This is

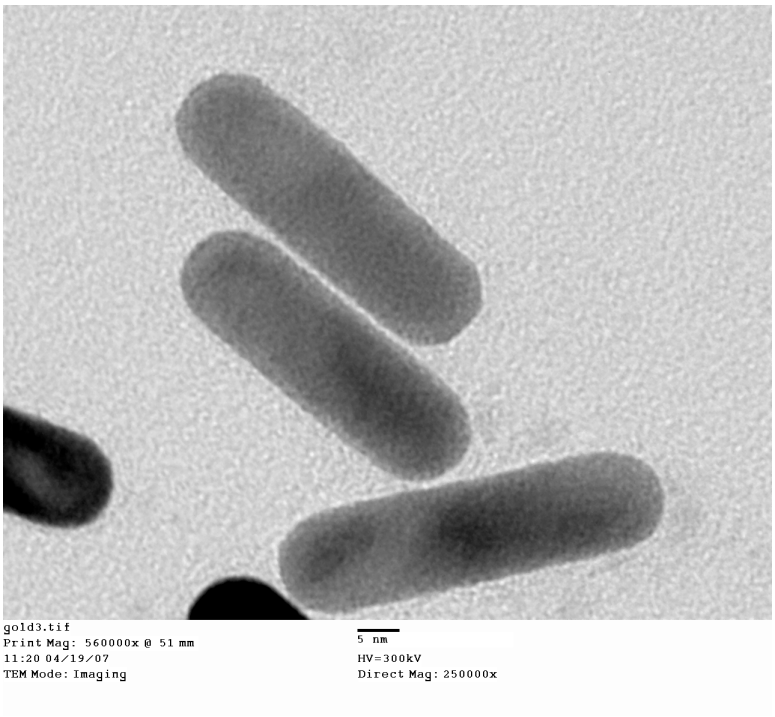

Figure 1.4: An overview of the different length and width Au nanorods present in a colloidal sample. The solution is mainly composed of different size nanorods.

due to the polydispersity of the Au sample containing nanorods with different length and width contributing to the plasmon peak.

Our calculations show that the plasmon peak of the prolate particles are also affected by the host dielectric (water in this case). Figure 1.7 shows plots of the plasmon absorption of a Au nanorod with $\rho = 4$ with varying ϵ_m. These plots clearly show the dependance of the plasmon peaks on the medium dielectric constant; they show that the plasmon peaks shift to the red as the ϵ_m is increased. The position and shape of the plasmon absorption of spheroids nanoparticles depends not only on their composition and hence on the correct form of the material dielectric constant, but also on the dielectric function of the surrounding medium ϵ_m. In figure 1.7 it is shown that by increasing ϵ_m, the plasmon band intensity and bandwidth also increases as well

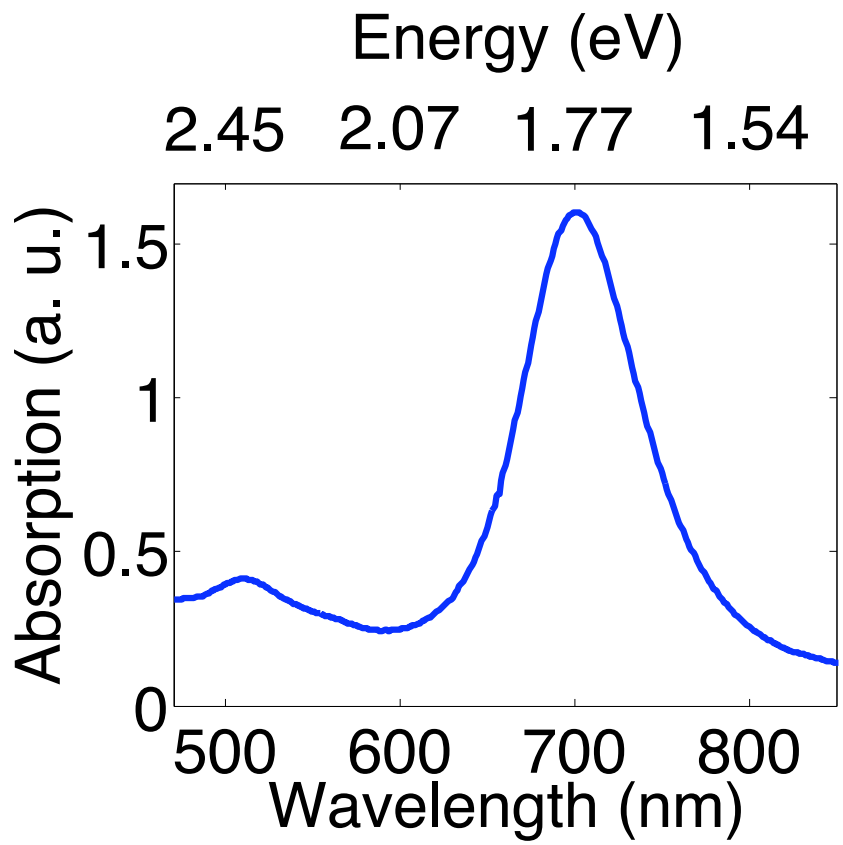

Figure 1.5: Ensemble optical absorption spectrum of colloidal Au nanorods. The 1^{st} peak at 520nm is the main surface plasmon absorption of Au and the 2^{nd} is to the longitudinal absorption of the nanorods, the observed broadening is due to the polydispersity of the sample.

as a red shift of the plasmon peak; this is known as immersion spectroscopy [7].

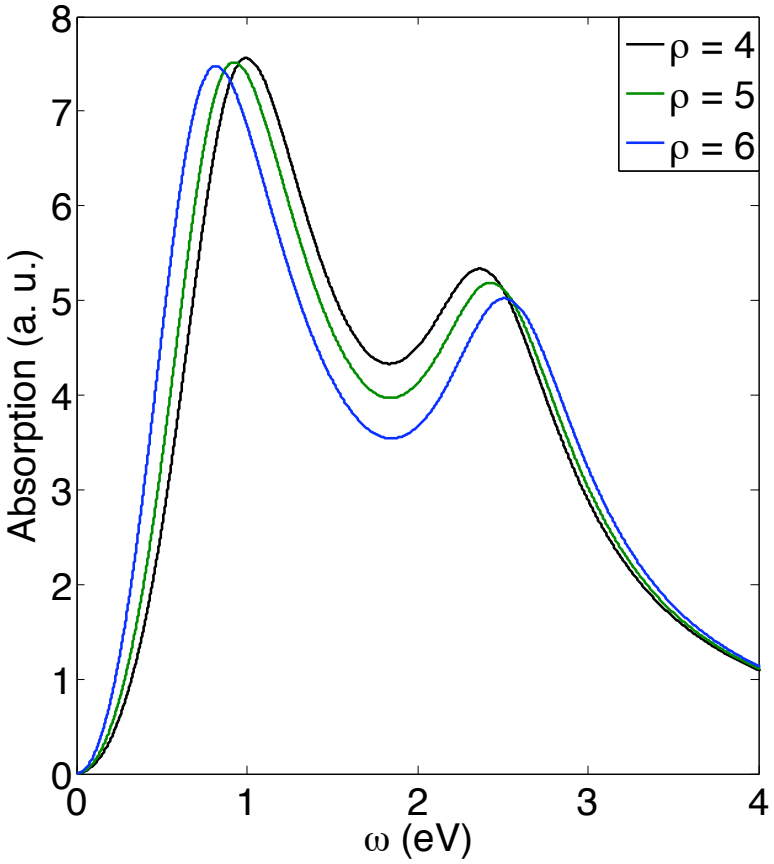

Figure 1.6: Simulation of the surface plasmon absorption of Au nanorods with varying aspect ratio, the medium dielectric cosntant ϵ_m is set to 1. This shows the dependence of the longitudinal plasmon to the particle aspect ratio

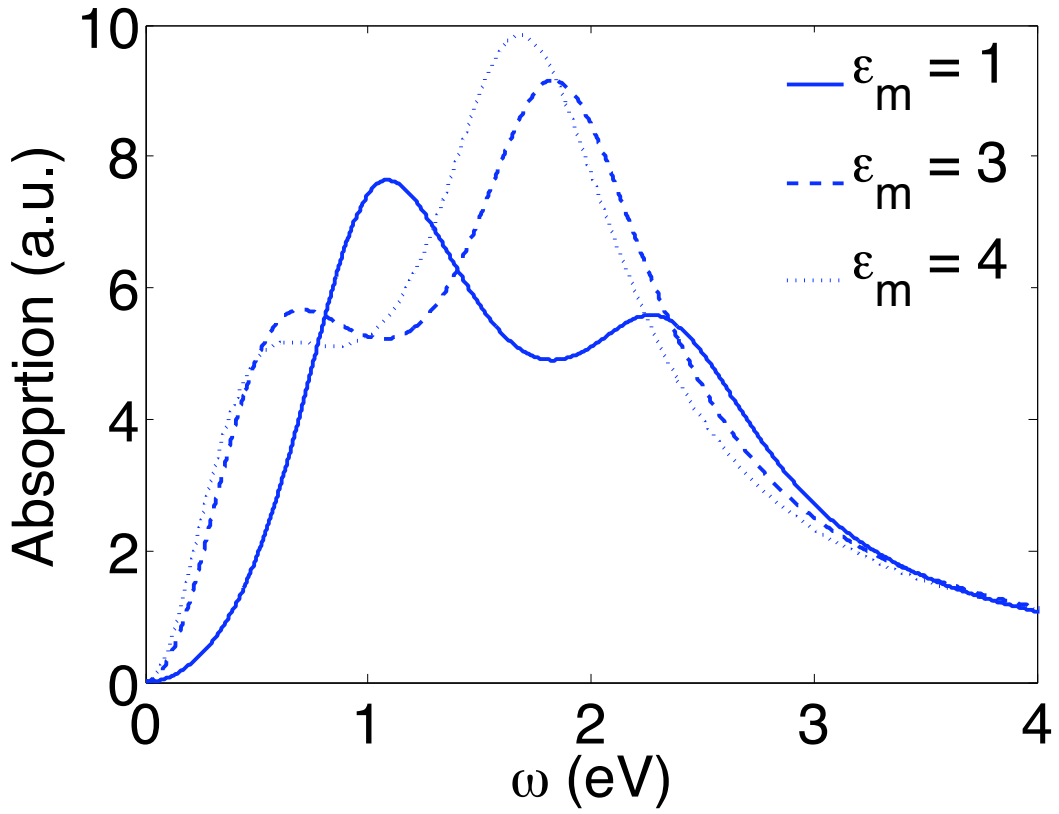

Figure 1.7: Calculated absorption spectra of a Au nanorod with aspect ratio $\rho = 4$, with varying dielectric constant ϵ_m

CHAPTER II

Analytical Description of the Energy Loss Probability for Electron Passing by a Spheroid

2.1 Introduction

State of the art electron energy loss spectroscopy (EELS) performed using scanning transmission electron microscope has allowed the acquisition of optical informations of a single metallic nanostructure. This has renewed interests in theoretical investigation of the energy loss experienced by electrons passing through or near a nanoparticle. The losses of interest are mostly due to intra-band transition of individual conduction electron [21]. One can also obtain information on the size, shape, composition and location of isolated particulate embedded in a host material and thus obtain high resolution chemical maps[22]. Pines and Bohm [23] also have suggested that the energy losses suffered by electrons passing near or through a small metallic object are due to the excitation of plasma oscillation or plasmons in the sea of conduction electron. In short many different types of surface collective effects can be observed through EELS, but we are primarily concerned with surface plasmons. A large amount of theoretical have addressed energy loss in thin films [11], metallic

spheroids (sufficiently small that retardation effects may be neglected) [22], and fully relativistic calculations of energy loss [24].

Ferrell *et al.* [22] have investigated the characteristic energy loss of fast electron flying by an oblate dielectric spheroid at near grazing incidence. The results derived therein are expressed in term of the frequency dependent and spatially local, dielectric function, this expression can then be applied to all materials with known optical constants.

Our derivation follows closely the approach adopted by Ferrell *et al.*, but we include the transformations necessary to yield results for the prolate case, which to the best of our knowledge hasn't been published.

The nanostructures we characterize throughout this chapter: silver (Ag) nanowires and gold (Au) nanorods, are modeled as spheroidal particles [25].

A spheroid can either be prolate or oblate. It has two main characteristic lengths, its major and minor axes. The oblate case contains all geometries between that of a sphere and a thin disk, while the prolate case covers a range of shapes from a sphere to a needle see figure 2.1.

Our approach is to consider a metallic prolate spheroid in (surrounded by) a dielectric host. The basic mathematical tools are presented in section 2.2.1. We then derive the electric potential in prolate spheroidal harmonics in section 2.2.2. The analytical solution for the energy loss is calculated in section 2.2.3. In section 2.3 we present a numerical evaluation and discussion of our results.

We have borrowed from and extended well established work, beginning with the work of Jackson [10], Smythe [26], and Scaife [27]. Atomic units (a.u., i.e., $e = m_e = \hbar = 1$)

are used throughout unless otherwise specified.

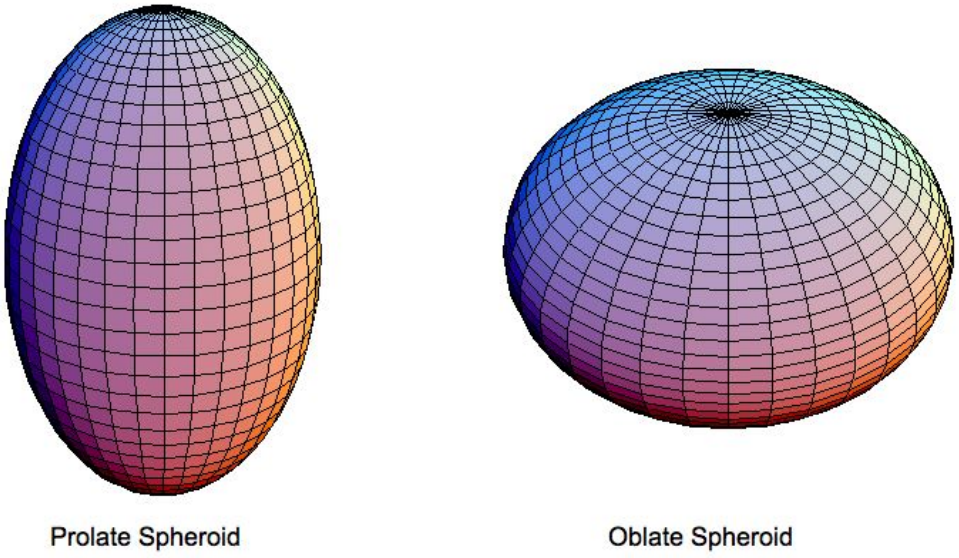

Figure 2.1: A spheroid is a quadric surface in three dimensions obtained by rotating an ellipse about one of its principal axes. Three particular cases of a spheroid are: 1) the ellipse is rotated about its major axis, the surface is a prolate spheroid; 2) the ellipse is rotated about its minor axis, the surface is an oblate spheroid.

2.2 Theory

2.2.1 Coordinate System

We consider a homogeneous spheroidal particle, which is a prolate or oblate immersed in a homogeneous, isotropic medium. Oblate spheroidal coordinates (η, μ, ϕ) are related to Cartesian coordinates (x, y, z) as:

$$x = a[(1+\eta^2)(1-\mu^2)]^{\frac{1}{2}} \cos\phi, \qquad 0 \leq \eta \leq \infty \tag{2.1}$$

$$y = a[(1+\eta^2)(1-\mu^2)]^{\frac{1}{2}} \sin\phi, \qquad -1 \leq \mu \leq 1 \tag{2.2}$$

$$z = a\eta\mu, \qquad 0 \leq \phi \leq 2\pi \tag{2.3}$$

where μ is the angular coordinate, η is the radial one, ϕ is the azimuthal one. The prolate spheroid coordinates are related to cartesian coordinates as:

$$x = a[(\eta^2-1)(1-\mu^2)]^{\frac{1}{2}} \cos\phi, \qquad 0 \leq \eta \leq \infty \tag{2.4}$$

$$y = a[(\eta^2-1)(1-\mu^2)]^{\frac{1}{2}} \sin\phi, \qquad -1 \leq \mu \leq 1 \tag{2.5}$$

$$z = a\eta\mu, \qquad 0 \leq \phi \leq 2\pi. \tag{2.6}$$

The size and shape of the spheroid are determined by the two quantities such as a the focal length of the confocal spheroid and the eccentricity e. The eccentricity is related to the radial coordinate μ in the oblate system:

$$e_o = \frac{1}{\mu} \tag{2.7}$$

and

$$e_p = \frac{1}{(\mu^2+1)^{\frac{1}{2}}} \tag{2.8}$$

for the prolate system.

In order to obtain the gradient operator in prolate spheroidal coordinates we make the connection between η, μ, ϕ and the spherical polar coordinates r, θ and ϕ we find that:

$$\overrightarrow{\nabla} = \hat{\eta}\frac{1}{a}\sqrt{\frac{(\eta^2-1)}{(\eta^2-\mu^2)}}\frac{\partial}{\partial\eta} + \hat{\mu}\frac{1}{a}\sqrt{\frac{(1-\mu^2)}{(\eta^2-\mu^2)}}\frac{\partial}{\partial\mu} + \hat{\phi}\frac{1}{a}\sqrt{(\eta^2-1)(1-\mu^2)}\frac{\partial}{\partial\phi} \tag{2.9}$$

in which $\hat{\eta}, \hat{\mu}$ and $\hat{\phi}$ are mutually perpendicular unit vector, and Laplace's equation for the scalar potential $\psi(\eta, \mu, \phi)$ may be written:

(2.10)
$$\frac{1}{a^2(\eta^2-\mu^2)}\left\{\frac{\partial}{\partial\eta}\Big[(\eta^2-1)\frac{\partial\Psi}{\partial\eta}\Big]+\frac{\partial}{\partial\mu}\Big[(1-\mu^2)\frac{\partial\Psi}{\partial\mu}\Big]\right\}+\frac{1}{a^2(\eta^2-1)(1-\mu^2)}\frac{\partial^2\Psi}{\partial^2\phi}=0$$

2.2.2 Scalar Functions

We consider a fast electron moving in a straight path with constant speed v, passing near a homogeneous prolate spheroid located in vacuum as shown in figure 2.2. The trajectory is specified in Cartesian coordinates by $(b, 0, vt)$, which corresponds to a problem with axial symmetry or no dependence on ϕ. Thus the trajectory can also be expressed in spheroidal coordinates as $(\eta'(t), \mu'(t), 0)$ found by inverting Eqs 2.4, 2.6. The Solution to Laplace's equation (Eq 2.10) inside and outside the spheroid and the electrostatic Green's function in prolate spheroidal coordinates can then be derived. We note that the electrodynamic responses of the media inside the spheroid and outside differ at different frequencies, thus we'll use the Fourier frequency components of the potential to match boundary conditions. We let $\epsilon_p(\omega)$ and $\epsilon_m(\omega)$ be the complex dielectric functions of the spheroid and the surrounding medium respectively. Let $\eta = \eta_o$ at the surface of the target, then the scalar potential's Fourier component in the region $\eta < \eta_o$ is:

(2.11)
$$\Psi_{in} = \sum_{l=0}^{\infty}\sum_{m=0}^{l} B_{lm}(\omega)P_{lm}(\eta)P_{lm}(\mu)\cos(m\phi)$$

and for $\eta_o < \eta$ the potential has a Fourier component:

(2.12)
$$\Psi_{out} = \sum_{l=0}^{\infty}\sum_{m=0}^{l} A_{lm}(\omega)Q_{lm}(\eta)P_{lm}(\mu)\cos(m\phi) + qG(\vec{r}-\vec{r'},\omega)$$

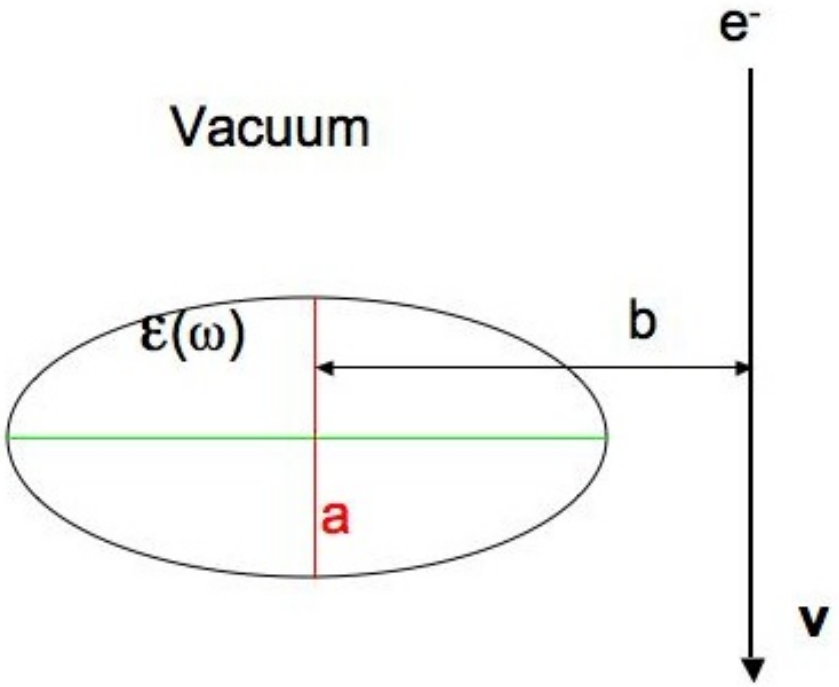

Figure 2.2: representation of the geometry under study: an electron is moving in vacuum with constant velocity and impact parameter b. The homogeneous prolate spheroid is described by a frequency dependent dielectric function $\epsilon(\omega)$

where q is the charge of the electron. For $\eta_o < \eta < \eta'$ the electrostatic Green's function in spheroidal coordinate is given by Smythe [26] as:

$$G(\vec{r} - \vec{r'}, \omega) = \frac{1}{\epsilon_m(\omega)} \sum_{l=0}^{\infty} \sum_{m=0}^{l} M_{lm} H_{lm}(\omega) P_{lm}(\eta) P_{lm}(\mu) \cos(m\phi) \tag{2.13}$$

with,

$$M_{lm} = \frac{(2 - \delta_{0m})(2l+1)}{a} \left[\frac{(l-m)!}{(l+m)!}\right]^2 \tag{2.14}$$

In the above expressions P_{lm} and Q_{lm} are respectively the associated Legendre functions of the first and second kinds, and finally,

$$H_{lm}(\omega) = \int_{-\infty}^{\infty} Q_{lm}(\eta') P_{lm}(\mu') e^{i\omega t} dt \tag{2.15}$$

with η' and μ' functions of t. Using identities given by Smythe we obtain:

$$H_{lm}(\omega) = \left(\frac{2\pi a}{|\omega| v}\right)^{\frac{1}{2}} \frac{(l-m)!}{(l+m)!} \left(\frac{\omega}{|\omega|}\right)^{l+m} \times J_{l+\frac{1}{2}}\left(\left|\frac{a\omega}{v}\right|\right) K_m\left(\left|\frac{b\omega}{v}\right|\right) \tag{2.16}$$

where $J_{l+\frac{1}{2}}$ is a the ordinary Bessel function of order $l+\frac{1}{2}$ and K_m is a modified Bessel function of order m.

The coefficients B_{lm} and A_{lm} are constants whose values will be determined by satisfying appropriate boundary conditions. At $\eta = \eta_o$ the potential must be continuous and the normal component of the Fourier amplitude of the electric displacement vector must be continuous. Only $A_{lm}(\omega)$ is of interest as it represents the coefficient of the homogeneous portion of the external potential. We conveniently write it in the form provided in ref [22]:

$$A_{lm}(\omega) = \Phi_{lm}(\omega)\left(1 - \frac{1}{\epsilon_m(\omega)}\right) - \Phi_{lm}(\omega)\alpha_{lm}(\omega) \tag{2.17}$$

where,

$$\Phi_{lm}(\omega) = \frac{qM_{lm}P_{lm}(\eta_o)H_{lm}(\omega)}{Q_{lm}(\eta_o)} \tag{2.18}$$

$$\alpha_{lm}(\omega) = \frac{\epsilon_p(\omega) - 1 - [\epsilon_m(\omega) - 1]\beta_{lm}}{\epsilon_p(\omega) - \epsilon_m(\omega)\beta_{lm}} \tag{2.19}$$

and

$$\beta_{lm} = \frac{Q'_{lm}(\eta_o)P_{lm}(\eta_o)}{P'_{lm}(\eta_o)Q_{lm}(\eta_o)} \tag{2.20}$$

which is the surface plasmon eigenvalue for the (l, m) mode of the dielectric function and real and negative number.

The first term in (2.17) is treated as a correction to the bulk plasmon losses [22]. However, in our case the local character of the dielectric function guarantees that

no beam losses are suffered to bulk excitation. Surface plasmon losses are our only concern here not volumes losses, thus we will not take into consideration this term in the following calculations. Note that A_{lm} vanishes for $l = m = 0$, so the sums begin with $l = 1$, $m = 0$.

2.2.3 Analytical Solution for the Energy Loss

The positive energy loss suffered by the fast electron passing near the spheroid can be related to the force exerted by the induced electric field E_{ind} acting on it. The passing charge has an impact parameter b which is assumed to be sufficiently large that the spheroid is not penetrated. We define work done in term of the so called loss probability then we get:

$$W = \int \vec{v}.\vec{E}_{ind}(\vec{r}_t, t)dt = \int_0^\infty \omega\Gamma_{loss}(\omega)d\omega \tag{2.21}$$

it is also written as follow after applying the inverse Fourier transform homogeneous part of (2.12):

$$W = \int_\infty^{-\infty} qE_{z'}dz = \int_\infty^{-\infty} d\omega \int_\infty^{-\infty} e^{-i(\omega/v)z'} \frac{\partial \Psi_{out}}{\partial z}\bigg|_{z=z'} dz' \tag{2.22}$$

where $E_{z'}$ is the z component of the induced field evaluated at the location of the charge and is obtained from the z component of (2.12). Equation (2.22) may be integrated by parts over the particle trajectory, the resulting integral is put in the following form via $z' = vt$ giving:

$$W = \frac{i}{2\pi} \sum_{l,m} \int_\infty^{-\infty} \omega A_{lm}(\omega) H_{lm}(-\omega)d\omega \tag{2.23}$$

or, changing to positive frequency range,

$$W = \frac{i}{2\pi} \sum_{l,m} \int_0^\infty \omega d\omega [A_{lm}(-\omega)H_{lm}(\omega) - A_{lm}(\omega)H_{lm}(-\omega)] \tag{2.24}$$

and from equation (2.21) we can deduce:

$$\Gamma_{loss}(\omega) = \int dt Re\{e^{-i\omega t}\vec{v}.\vec{E}_{ind}(\vec{r}_t,\omega)\} \tag{2.25}$$

then the energy loss probability for an electron passing a prolate spheroid parallel to the minor axis is:

$$\Gamma_{loss}(\omega) = \frac{2}{v\omega}\sum_{l=1}^{\infty}\sum_{m=0}^{l} C_{lm}\frac{P_{lm}(\eta_o)}{Q_{lm}(\eta_o)}J^2_{l+1/2}\left(\frac{a\omega}{v}\right)K^2_m\left(\frac{b\omega}{v}\right)\times Im[\alpha_{lm}(\omega)] \tag{2.26}$$

where $\mathrm{Im}[\alpha_{lm}(\omega)]$ is the imaginary part of $\alpha_{lm}(\omega)$, also,

$$C_{lm} = (-1)^m(2-\delta_{0m})(2l+1) \tag{2.27}$$

with, $\delta_{0m} = 1$ if $m = 0$ or 0 for $m \neq 0$.

In the limit of large η_o equation (3.2) recovers previous results derived by Ferrell and Echenique [28, 29] for spherical targets with $\beta_{lm} = -\frac{l+1}{l}$.

Equation (2.26) also has a form similar to its relativistic counterpart derived by Abajo [30]. In both cases, the dependence on impact parameter b is made evident inside the modified Bessel functions K_m which are decaying functions at large distances.

We also note that equation (2.26) is dependent on the spheroid dielectric response which is fully contained in the expression of α_{lm}; see equation (2.19).

2.3 Numerical Evaluation and Discussion

We have derived the energy loss probability (2.26) for an electron in vacuum passing by a metallic prolate spheroid. The calculations although involving all multipoles, are limited to numerical evaluation of $l = 1$ and $m = 0, 1$. The Drude dielectric function:

$$\epsilon(\omega) = 1 - \frac{\omega_p^2}{\omega(\omega + i\gamma)},$$

has been used to describe the spheroid with parameters appropriate for Au and Ag. Where ω_p is the the bulk plasmon and γ is the damping factor. It is important to note that most models in the literature for the dielectric constant of gold nanoparticles use the Drude model, so we also follow that convention. This is usually considered as a reasonable approximation as Dressel and Grüner have shown that the optical parameters to the Drude response at low frequwncies is dominated by the intraband contribution [31]. They have also calculated the plasma frequency ω_p of Au taking into consideration the inter-band contribution and have found it to compare well with the free electron model (see reference [31] page 305). Finally, in this work we have cited work from Pines [21], Ritchie [11], Ferrell [22], and Abajo [30]; in that body of work, the Drude free electron model is used for noble metals.

When a finite damping is considered in the dielectric constant, the feature of the loss spectra are broadened, we will set the value of $\gamma = 1.06$ for the following plots unless otherwise indicated. Figure (2.3) is a plot of the loss probability for 50 keV electron incident at different impact parameters $\frac{b}{a} = 1.05,\ 1.15,\ 1.3$, where a is the distance from the center of the prolate spheroid to its edge. In all plots we kept the shape parameter η_o constant at 0.3. We should note that η_o is dependent on the aspect ratio ρ of the particle, it is given by:

$$\eta_o = \frac{1}{\sqrt{\rho^2 - 1}} \tag{2.28}$$

The highly prolate spheroid in the form of a long needle or $\eta_o = 0.1$ corresponding to $\rho \sim 100$ clearly shows two distinct peaks for the Ag one due to the (1,1) mode at $1eV$ and a second peak due the cumulative effect of the remaining modes at $3.7eV$. As the spheroid becomes more spherical, all multipolar peaks move closer together to

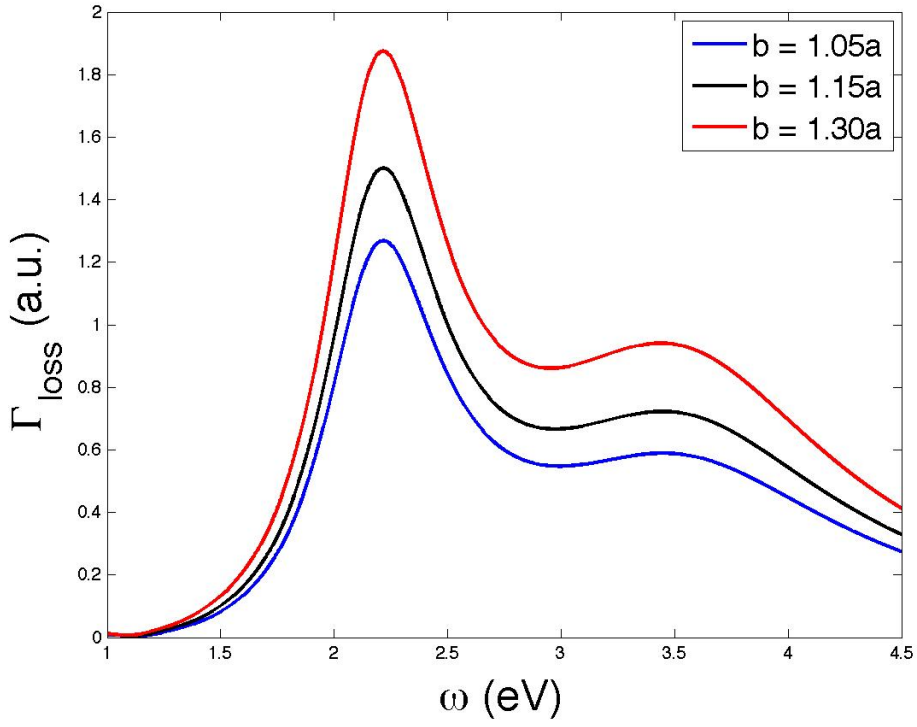

Figure 2.3: energy loss probability vs energy for 50 keV electrons incident a different impact parameter ($\frac{b}{a} = 1.05, 1.15, 1.3$) on a Ag prolate spheroid.

produce a broad peak while shifting towards the toward the resonance of the sphere; see figure (2.4). We also note that the resonance of spheres depends only on l at the dielectric values $-\frac{l+1}{l}$ and the corresponding energy losses for Ag will range from $\sim 3.5eV(l = 1)$ to $3.7eV(l \gg 1)$ [22]. For a given shape, in our case $\eta_o = 0.3$ each mode will have a unique energy peak that is invariant as we vary the values of a, b, and v. In figures (2.3, 2.5, 2.6) we've plotted the loss spectra function for different values of these parameters while holding the shape constant. We also see that the loss probability we derived above has some dependence on the surrounding medium dielectric and also on the dielectric of the prolate spheroid. This dependence is fully contained in α_{lm} equation (2.19), which shows a $\mathrm{Im}\left(\frac{1}{\epsilon(\omega)}\right)$ dependence. This is con-

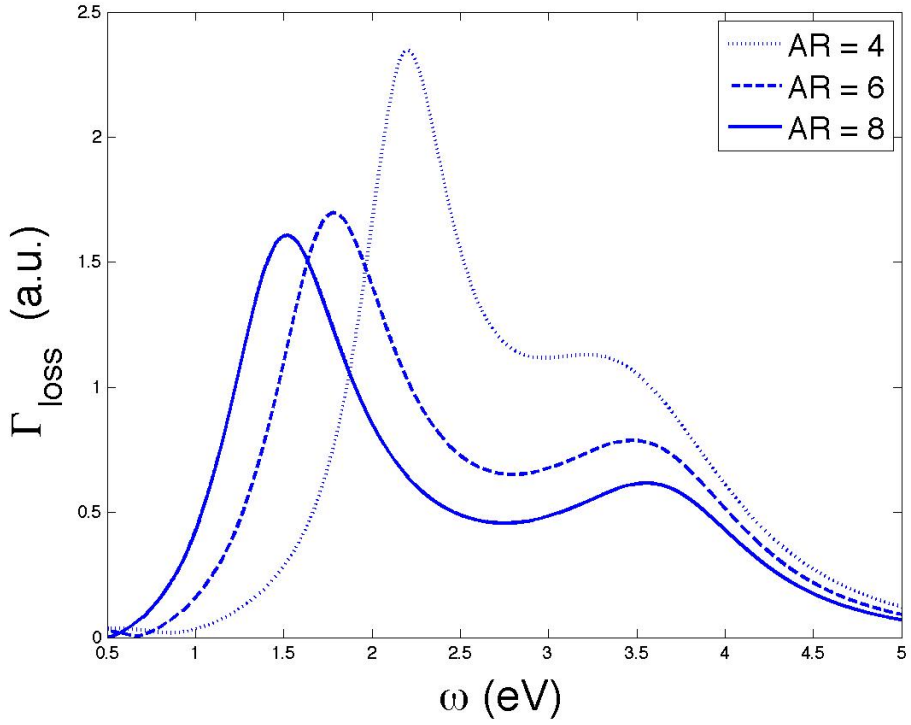

Figure 2.4: energy loss probability vs energy for 50 keV electrons with impact parameter ($\frac{b}{a} = 1.05$) incident on three different Ag prolate spheroid of different shape ($\eta_o = 0.38, 0.45, 0.58$), see equation (2.28).

sistent with the classical expression of the energy loss spectrum derived by Pines [21] and Glick and Ferrell [32]. They show that the energy transfer from the electron beam to the electron gas is determined by $\mathrm{Im}\left(\frac{1}{\epsilon_p(\omega)}\right)$, where $\epsilon_p(\omega)$ is the frequency dependent complex dielectric function of the material particle.

Finally, We should mention that the relativistic counterpart of the energy loss probability for a metallic spherical particle$\left(\Gamma_{loss}(\omega)\right)$ has been derived by Abajo [24]. His results are compared to the non relativistic counterpart derived by Ferrell *et al* [22] and it shows that both calculations agree relatively well for small sphere radius but for larger sphere the differences are considerable specially in the position of the

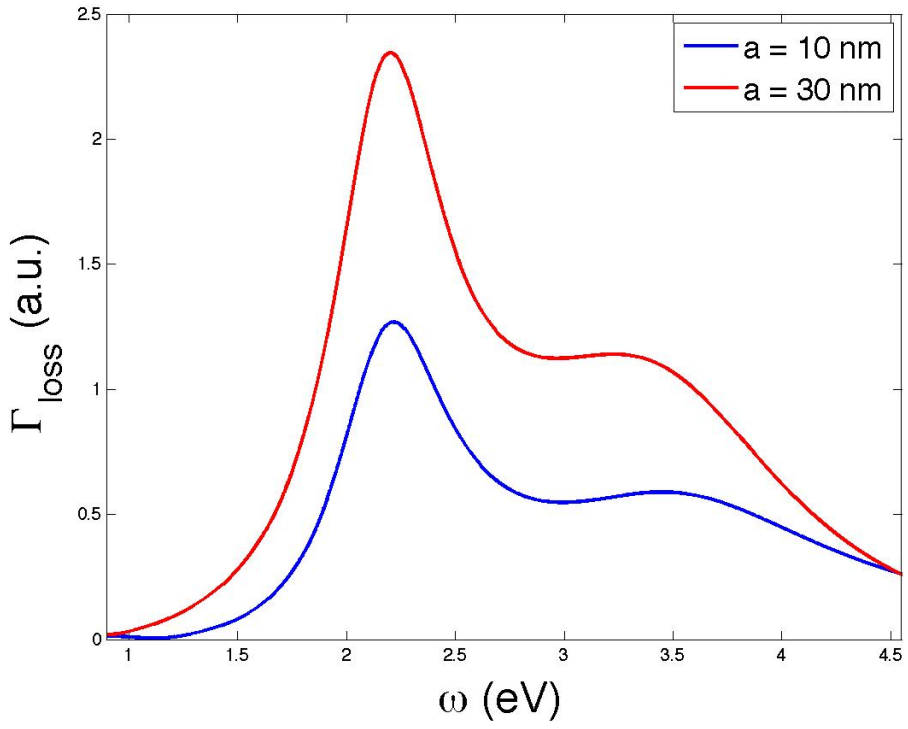

Figure 2.5: energy loss probability vs energy for 50 keV electrons at different impact parameter ($\frac{b}{a} = 1.05$) on a two different Ag prolate spheroid of equal shape ($\rho = 4$) and different size ($a = 10, 30$).

plasmon peaks and their relative magnitude. The relativistic limit goes beyond our comparative study.

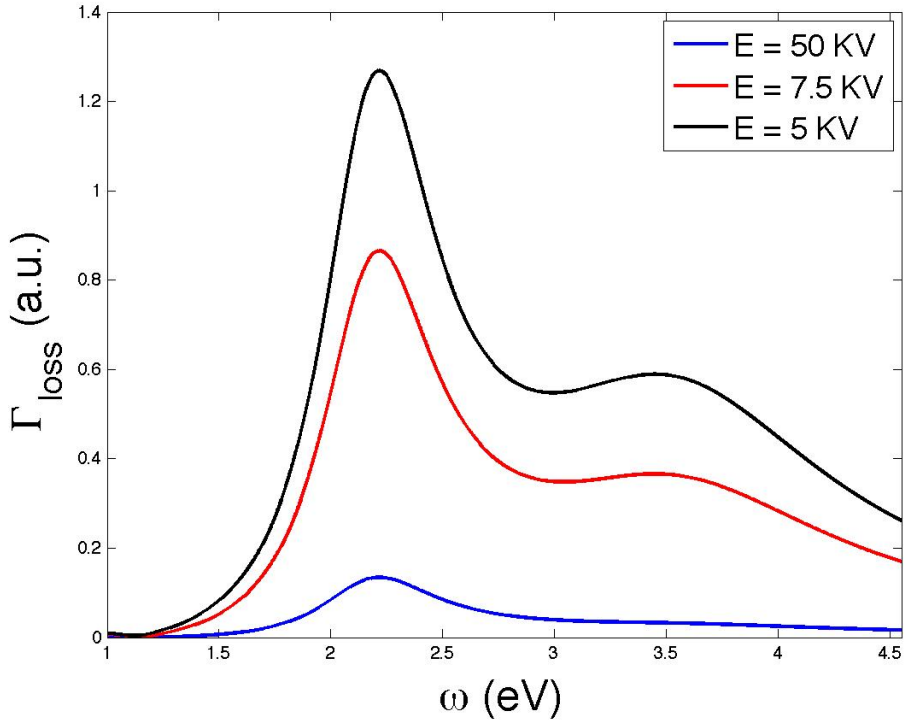

Figure 2.6: energy loss probability vs energy for Ag prolate spheroid with ($\eta_o = 0.3$) at impact parameter ($\frac{b}{a} = 1.05$) and size ($a = 10$). Shown are results for 3 different incident energies ($E = 5, 10$, and $50KeV$).

CHAPTER III

Single Particle Plasmon Spectroscopy of Gold Nanorods and Silver Nanowires

3.1 Introduction

The surface plasmon modes of metallic nanoparticles lie in the optical (visible and near-infrared) part of the electromagnetic spectrum, corresponding to energies in the range of a few eV. For this reason, optical spectroscopy has been one of the primary methods for investigating nanoparticle samples for many decades. Also, the development of new and powerful synthesis techniques has opened up the possibility of engineering the plasmon modes of metallic nanostructures for applications in optics and photonics. For example, the development of nanofabrication and self-assembly based on wet chemistry methods has enabled synthesis of high yield gold (Au) and silver (Ag) colloidal particles with well defined structures other than solid spheres[33], including triangular prisms, disks[34], shells [33], wires [35] and rods [36]. Most methods of synthesis produce samples with a range of nanoparticles with varying length and width. Characterization of samples in solution by optical absorption [3, 16] yields strongly inhomogeneously broadened spectra due to the sample

polydispersity.

In order to overcome the inhomogeneous broadening inherent in ensemble measurements, single-particle spectra are desired. One of the primary challenges in optical studies of nanostructures has been to measure the plasmon modes of single nanoparticles or single nanoparticle complexes. Scanning near-field optical microscopy (SNOM) [37] and dark field illumination (DF) [38] have been demonstrated to measure the absorption or scattering spectrum of a single nanoparticle. However, apart from the serious technical challenges involved in these experiments, SNOM and DF are limited in their ability to spatially resolve the mode structure of the plasmon, e.g. of a metal nanorod or nanowire. Thus, alternative techniques are required to measure the dielectric response function $\epsilon(\omega)$ of single metal nanoparticles.

Recent advances in electron microscopy have enabled the acquisition of energy loss spectra of single nanostructures with energies as low as 1.75 eV [39] and 2.5 eV for metal clusters [40]. Thus, the optical plasmon modes of nanoparticles are accessible using electron energy-loss spectroscopy (EELS). EELS involves analyzing the energy of initially mono-energetic electrons, after they have interacted with a specimen [41]. This interaction takes place within a few atomic layers; hence EELS provides a highly localized spectrum of the excitations of the system.

Physically, a plasma oscillation may be induced by either the driving electric field of a resonant optical field, or impulsively by the transient field associated with a fast electron passing near a nanoparticle. Energy lost by a monoenergetic electron beam due to excitation of plasmon oscillations can be directly measured, yielding the plasmon spectrum [11, 41]. Furthermore, the small size of the electron beam

allows measurements of energy loss with high spatial resolution ($1 - 4\ nm$), thus enabling the spatial structure of a plasmon mode to be mapped with a resolution not achievable by near-field optical methods.

The ability of high-resolution EELS to measure nano-plasmonic resonances has been demonstrated by Khan *et al* [42] and the work of Colliex *et al* [39]. Those studies have shown the feasibility of detecting spectral features for low energy loss and of mapping the spatial variation of surface plasmon resonances on individual noble metal nanostructures. They have also demonstrated its capability to image these localized optical excitation with sufficient resolution to reveal dramatic spatial variation over a single nanoparticle[39]

The question naturally arises, therefore, as to the relation between optical spectroscopy and electron energy loss spectroscopy (EELS). The goal of both measurements is to determine the dielectric function of a nanoparticle or particle complex. Optical absorption generally measures $\mathrm{Im}\Big(\epsilon(\omega)\Big)$. On the other hand it has been established that the energy loss function characterizing energy transfer to the electron gas of bulk plasmon modes is determined by the energy loss function $\mathrm{Im}\Big(\frac{1}{\epsilon_p(\omega)}\Big)$ [21]. EELS spectra for nanoparticles have been calculated directly for several specific cases [30, 22]. Here, we compare the experimental spectra obtained by optical absorption and by EELS to observe the relationship between these different approaches to plasmon spectroscopy. We also examine the relation between the theoretical representation of EEL spectra and the optical measurements. We plot together and discuss the energy loss probability equation 3.2, the optical absorption $\mathrm{Im}\Big(\epsilon(\omega)\Big)$ and the energy loss function $\mathrm{Im}\Big(\frac{1}{\epsilon_p(\omega)}\Big)$ obtained from equation 1.40.

3.2 Experiment

3.2.1 Synthesis of Gold Nanorods and Silver Nanowires

The Au nanoparticles were fabricated using a seeding growth method to make varied aspect ratio gold and silver nanorods[36, 43]. The rod aspect ratio could be controlled from 1 to 7 by simply varying the ratio of seed to metal salt in the presence of a rod like micellar template[44]. It is observed that the use of additives such as $AgNO_3$ and cyclohexane strongly influenced the gold nanorod formation. The cylindrical shape of the Au rods in figure 3.13 is distinctly different from an earlier observed needlelike shape. This method requires no nano-porous template and therefore may be more practical for large-scale synthesis.

The sample of Au nanoparticles used in our experiment contains nanorods with aspect ratio 4.6 ± 1. They are prepared in a clean test tube, 10 mL of growth solution, containing 2.5×10^{-4} M $HAuCl_4$ and 0.1 M cetyltrimethylammonium bromide (CTAB), was mixed with 0.05 mL of 0.1 M freshly prepared ascorbic acid solution, next 0.025 mL of the 3.5 nm seed solution is added. No further stirring or agitation was done. Within 5-10 min, the solution color changed to reddish brown. The solution contained 4.6 aspect ratio rods, spheres, and some plates shown in figure 4.1. The Ag nanowires were assembled using the polyol method; details are given in [45]. The polyol method involves the reduction of a metal salt precursor by a polyol, a compound containing multiple hydroxyl groups. The polyol used in this synthesis, ethylene glycol, served as both the reducing agent and solvent. 5 mL of ethylene glycol was heated at 150C for one hour with stirring (260 rpm). This pre-heating was done in disposable glass vials placed in an oil bath. 40 μL of a 4

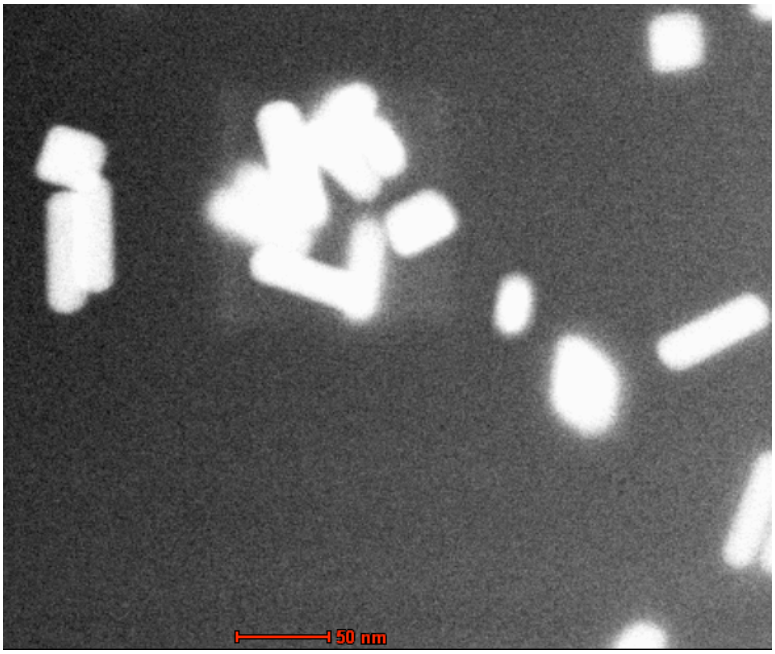

Figure 3.1: TEM images of 4.6 aspect ratio gold nanorods

mM CuCl22H2O/ethylene glycol solution was added, and the solution was allowed to heat for 15 minutes. 1.5 mL 114 mM PVP/ethylene glycol was then added to each vial, followed by 1.5 mL 94 mM AgNO3/ethylene glycol. All reagents were delivered by pipette. The reaction was stopped when the solution became gray and wispy, after approximately one hour. The reaction was stopped by submerging the vials in cold water. The product was washed once with acetone and three times with deionized water.

The produced wires were relatively uniform in shape and size. They had a pentagonal cross-section, as determined by scanning electron microscope (SEM), and were, on average, approximately 0.5-50 μm in length.

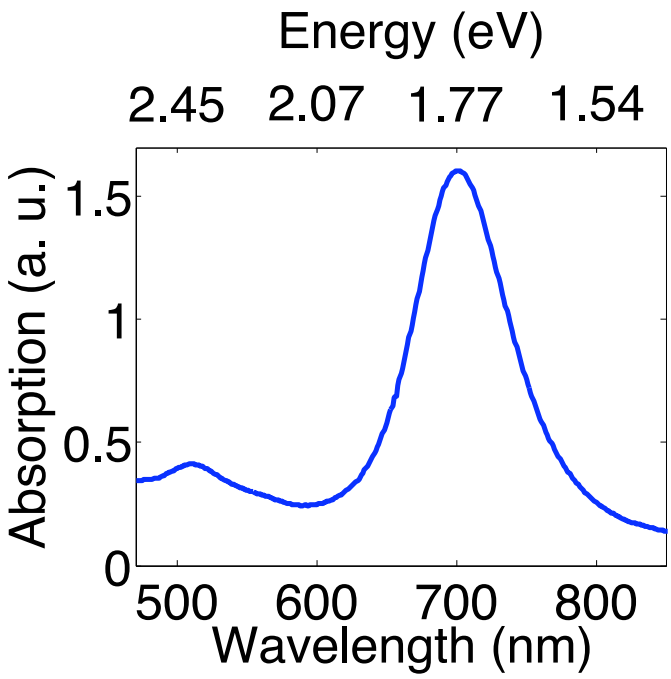

Figure 3.2: Ensemble optical absorption spectrum of solution. The 1^{st} peak at 520nm is the main surface plasmon absorption of Au and the 2^{nd} is to the longitudinal absorption of the nanorods, the observed broadening is due to the polydispersity of the sample.

3.2.2 Electron Energy Loss Spectroscopy

Electron energy loss spectroscopy (EELS) in the transmission electron microscope (TEM) is the study of the vibrational motion of atoms and molecules on and near the surface of thin film materials by the analysis of the energy spectrum of low-energy electrons backscattered from it. An electron passing through or near a material can interact with electron clouds of the atoms present and transfer some of its kinetic energy to them. There are four widely used kinds of electron spectroscopy techniques, they are:

- Electron Energy Loss Spectroscopy(EELS)

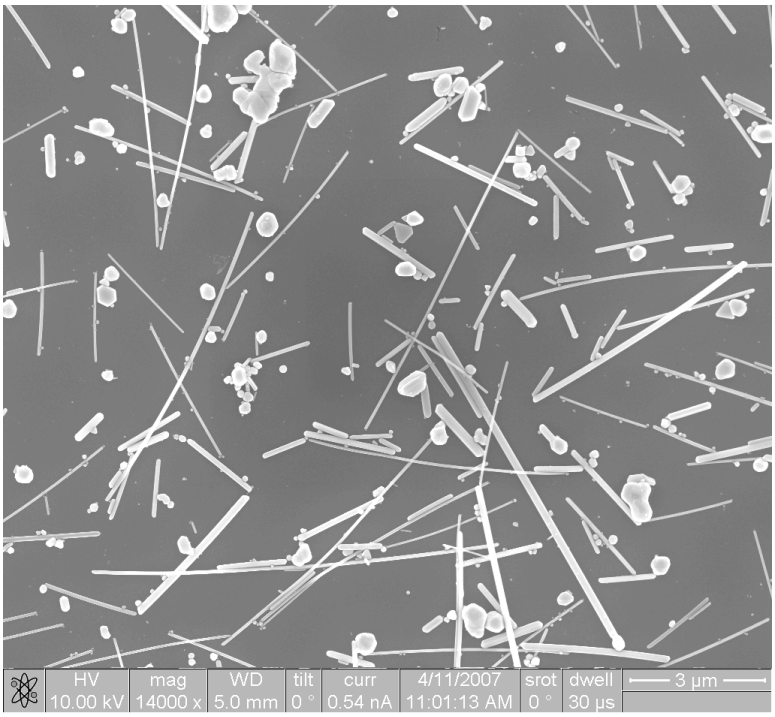

Figure 3.3: SEM images of silver nanowires

- High Resolution Electron Energy Loss Spectroscopy(HREELS)
- Core Electron Energy Loss Spectroscopy(CEELS)
- Valence Electron Energy Loss Spectroscopy (VEELS)

In our experiment EELS is the main technique employed. EELS uses electrons from 0.1 to 80 keV and passes them through a thin foil or small particle of the material of interest. At high energies, the transmitted beam contains inelastically scattered electrons whose energy has been decreased by amounts corresponding to characteristic absorption frequencies in the solid. At lower energies, the reflected beam is monitored for the same transitions. Bulk and surface plasmons are the principal features of these spectra.

The typical EEL spectrum we obtain from our experiments is shown in figure 3.6. It

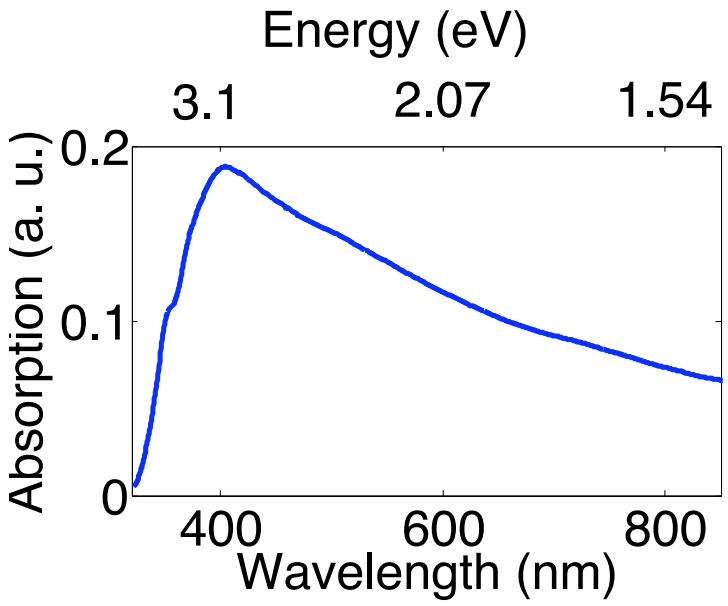

Figure 3.4: (a) Ensemble optical absorption spectrum of Ag nanowires in solution; the peak at 3.5eV is due to the transverse plasmon absorption. The broad peak is due to longitudinal plasmon absorption; the broadening is due to contributions from different length and width nanowires present in the solution.

features two parts of interest:

- The zero-loss peak centered at 0 eV, it mainly contains electrons that still have the original beam energy (E_i), i.e., they have only interacted elastically or not at all with the specimen. In thin specimens, the intensity of the zero-loss beam is high, so that damage of the CCD chip can occur and since there is no useful information in it, the zero-loss beam is very often omitted during spectrum collection.

- Low-loss region ($<$ 10 eV): here, the electrons that have induced plasmon oscillations occur. Since the plasmon generation is the most frequent inelastic interaction of electron with the sample, the intensity in this region is relatively

high. Intensity and number of plasmon peaks increases with specimen thickness, size, and shape.

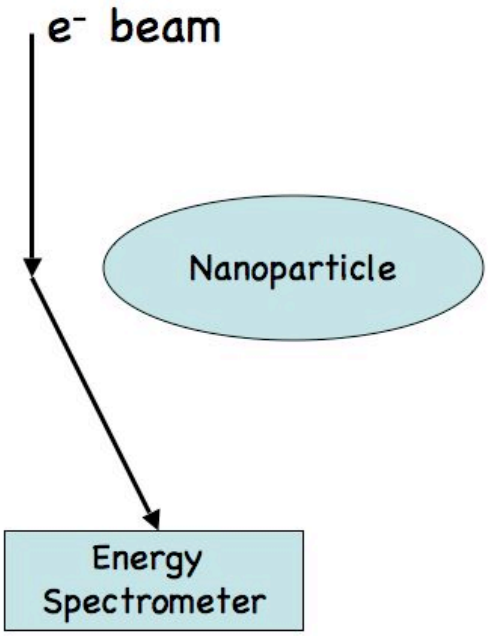

Figure 3.5: A typical electron energy loss spectrum scheme is shown. The electrons are collected through a spectrometer to show their energy distribution following their interaction with the sample.

Throughout our study, we use two methods to collect EEL spectrum from our samples:

- the stationary probe mode in which, the beam is static at a location on or near the sample at which point all the generated signal is collected to produce a spectrum,
- or in scanning transmission electron microscope (STEM) mode in which, a tiny, convergent electron beam is scanned over a defined area of the sample. At each

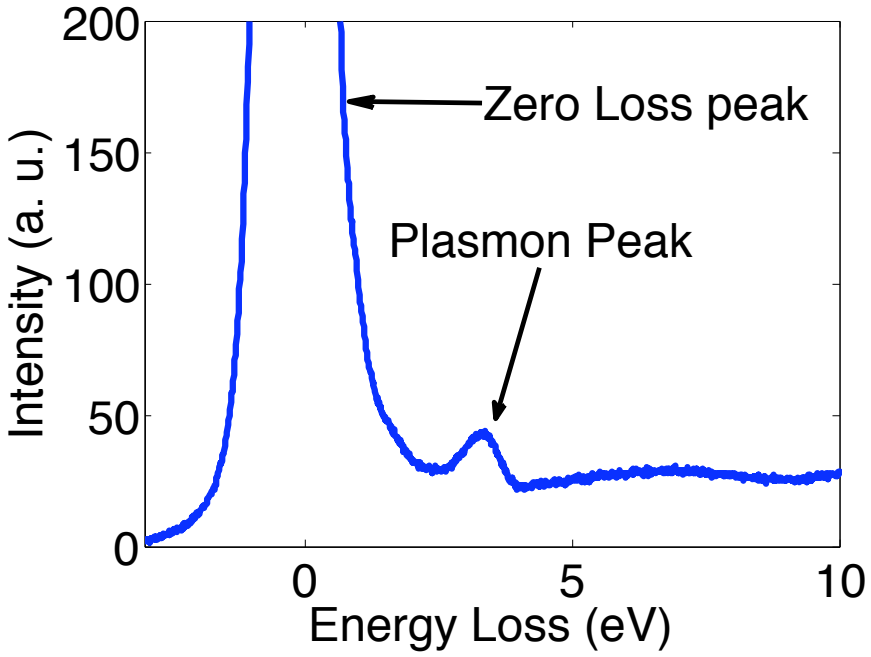

Figure 3.6: A typical electron energy loss spectrum is shown displaying the peaks of interest: the zero loss peak and the plasmon peak

spot, the generated signal is simultaneously recorded, building up an image. Furthermore, such a convergent beam is used to gain a highly localized signal from the specimen in analytical TEM (e.g., EELS), and thus the combination of STEM with EELS is a the main tool used to image plasmon energy distribution.

3.3 Results and Discussion

EELS measurements were carried out on an FEI Titan (OSU) , FEI Tecnai F20 (ANL), a JEOL 2010 (U of M), and a FEI Titan 80-300 (LBL) all equipped with HR EELS spectrometers with energy resolutions ranging from 0.2 to 1 eV. To improve the visibility of the spectral features in the EELS data presented in this work, deconvolution was performed using a commercial software (HREM Research Inc.) utilizing the Richardson-Lucy algorithm [46]. The nanoparticle spectra were deconvoluted from the spectrum of the support film collected under similar conditions. We note however that our conclusions regarding resonance positions and behavior are not dependent on the deconvolution.

With the various state-of-the-art EELS used in this work, we have resolved the plasmon modes of individual Ag nanowires, and individual and pairs of Au nanorods. These particles have plasmon resonances in the UV, visible and near infrared. They have two plasmon absorption resonances; one is due to the transverse oscillation of electrons (i.e. electron motion perpendicular to the long axis of the rods or wires) with energy around 2.4 eV for Au and 3.5 eV for Ag, approximately coincident with the plasmon of spherical particles, while the second plasmon is due to the oscillation of electrons along the long axis. This longitudinal mode is red shifted and strongly

depends on the nanostructures aspect ratio, defined as the length divided by the width of the nanoparticle [3]. The energy resolution of the EELS system is sufficient to spectrally resolve these two modes. Furthermore, utilizing the nanoscale dimensions of the focused electron beam of the TEM, we are able to excite the nanoparticles at precise locations, and thus probe the spatial dependence of the relative excitation of the different plasmon modes. Energy Loss measurements reported herein were recorded in a stationary probe mode.

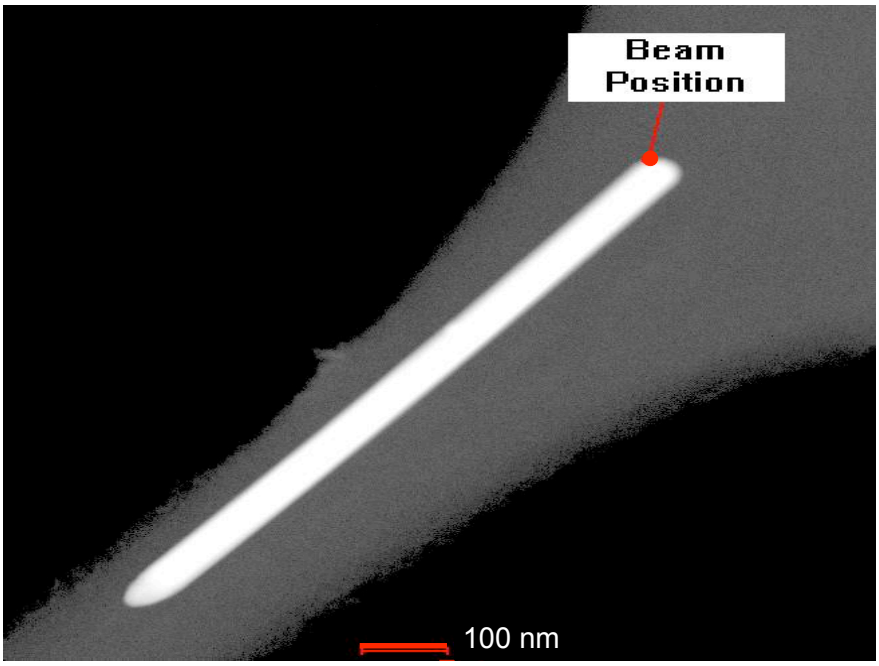

Figure 3.7: TEM images of Ag nanowires of length 706 nm and width 50 nm

A single droplet of the solution of Au or Ag nanostructures diluted in de-ionized water was placed on a thin SiO_x film supported on a 3 mm diameter copper mesh TEM grid. The solvent was evaporated in room temperature. Care was taken when acquiring single-nanoparticle spectra to leave sufficient spatial separation between

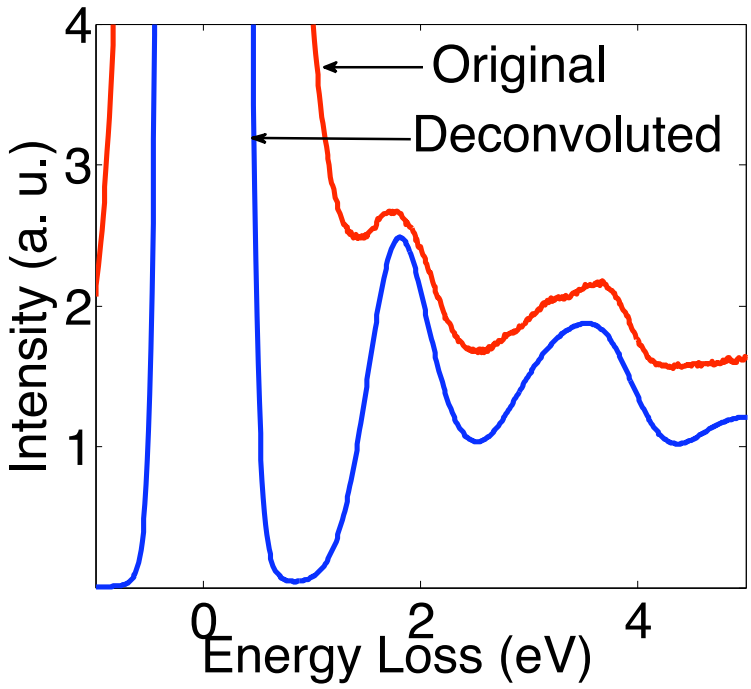

Figure 3.8: deconvoluted spectrum acquired from the edge of the particle. Two peaks are clearly resolved, the transverse mode is at 3.54 eV and longitudinal mode is at 1.8 eV.

particles to avoid electromagnetic coupling. After identifying a nanostructure of interest, we positioned the beam at the corner of the particle to induce charge displacement along both axes of the wire. Figure 3.8 shows raw and deconvoluted EEL spectra taken at the corner of a Ag nanowire 706 nm long and 50 nm wide (fig 3.7). Two main surface plasmon peaks are identified, at 1.8 eV and 3.54 eV, which correspond to the longitudinal and transverse plasmon respectively. For comparison, the optical absorption spectrum of the solution is shown in figure 3.9; the peak at 3.5 eV corresponds to the transverse plasmon absorption and the broad peak at lower energy is due to the absorption of different length and shape nanostructures present in the solution. The extremely broad peak in the ensemble optical spectrum

implies a highly polydisperse sample, containing nanostructures with a wide range of aspect ratios [47, 48]. We note that the nanoparticle concentration in solution is very low, and surface charge prevents aggregation, so the breadth of the spectrum may be attributed to inhomogeneous broadening and not to random interparticle electromagnetic coupling. Figure 3.10 shows spectra taken from different nanowires

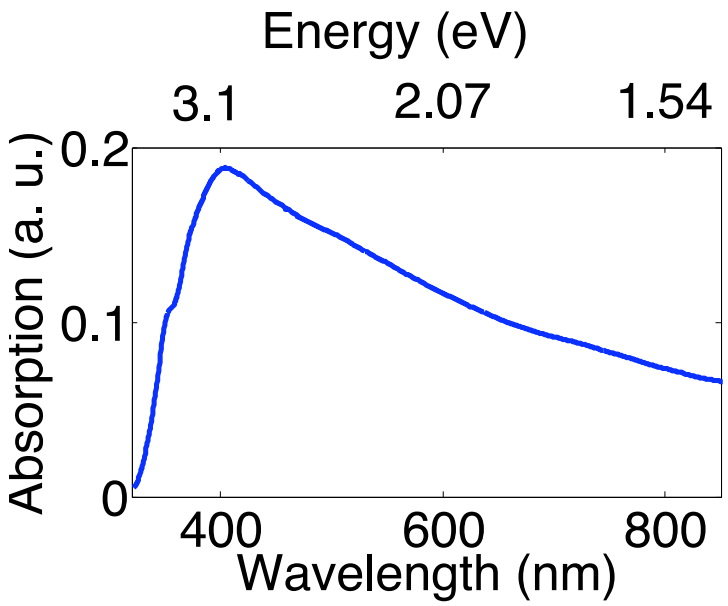

Figure 3.9: (a) Ensemble optical absorption spectrum of Ag nanowires in solution; the peak at 3.5eV is due to the transverse plasmon absorption. The broad peak is due to longitudinal plasmon absorption; the broadening is due to contributions from different length and width nanowires present in the solution.

of varying length and width, accurately measured from the TEM image to within a nanometer. As the length of the nanowire increases we observe a significant shift to lower energy of the longitudinal plasmon peak, while the transverse plasmon peak is nearly constant. The slight variation in the transverse mode peaks is due to different nanowire width and support film thickness. The variation of mode energy

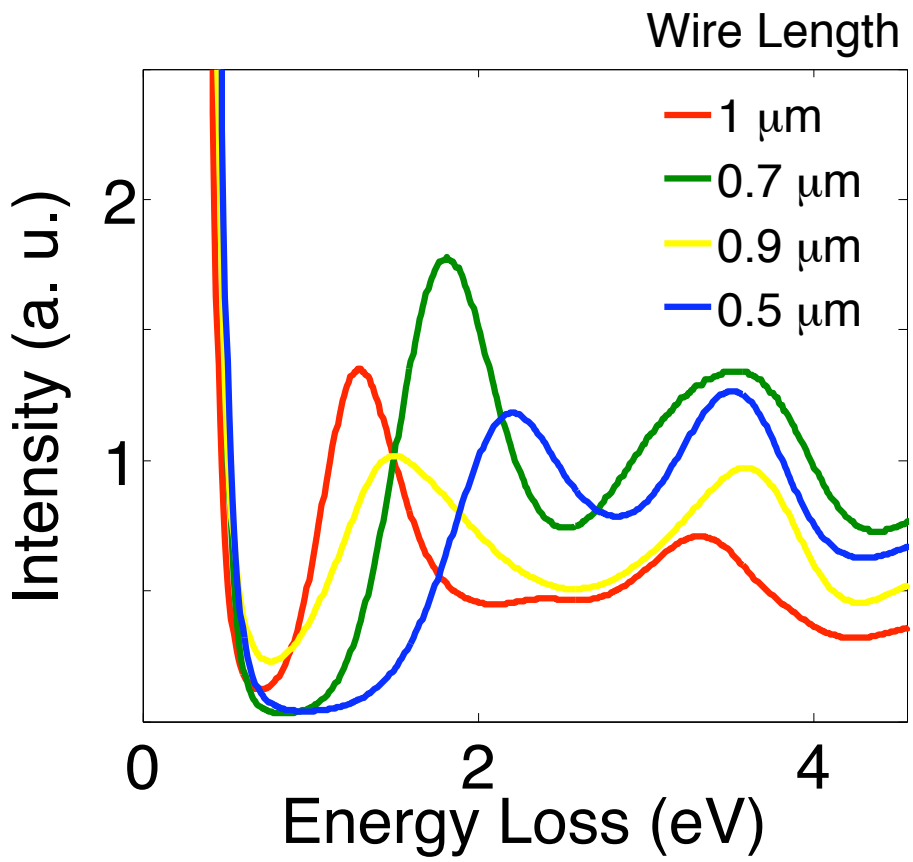

Figure 3.10: Deconvoluted spectra of four different length Ag wires with an average diameter of $\sim$ 50 nm: the transverse plasmon resonance is relatively consistent (3.4 to 3.6 eV); the slight peak variations can be largely attributed to wire thickness and film support. The longitudinal plasmon peak is red shifted as the wire length increases confirming its dependence on the particle aspect ratio.

with nanowire dimensions implies strong inhomogeneous broadening of the optical absorption spectra of ensembles; the optical absorption of our Ag nanowire sample is shown in figure 3.9.

Theory predicts that the number of resonance peaks increases when the symmetry of the cross sections of the Ag nanowires decreases [49]. Our results for 2D nanoparticles (nanowires) clearly show the longitudinal plasmon blue shifted as the particle aspect

ratio decreases. This result has been demonstrated optically in ensemble spectra, where the absorption spectra of nanowire samples fabricated with different average length [50].

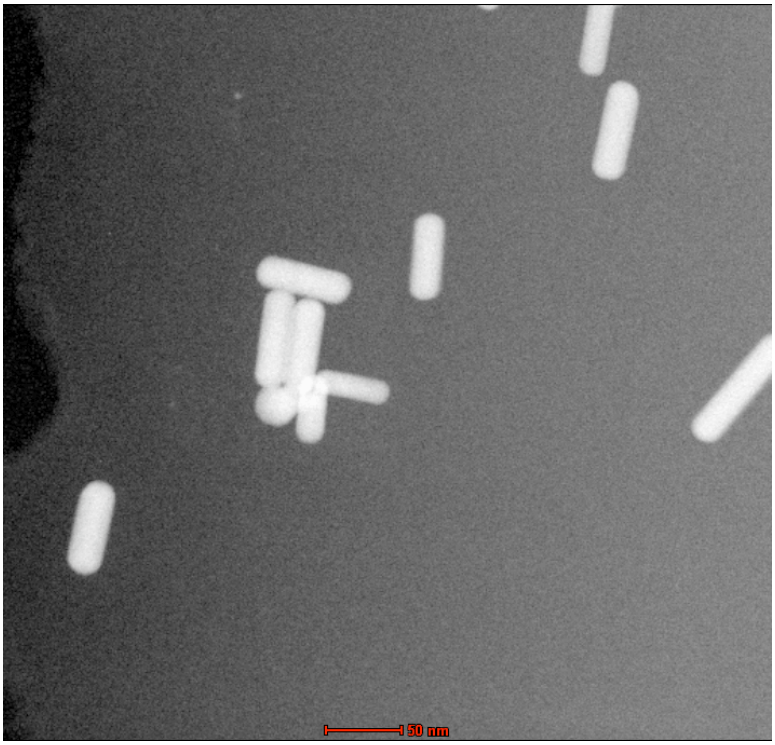

Figure 3.11: An overview of the different size and shape Au nanorods present in the sample. The solution is mainly composed of different size nanorods.

We next consider the plasmon resonances of Au nanorods which are generally at lower energy than those of silver. Figure 3.11 shows an overview of the shape and size of the nanorods present in the solution that accounts for the two peaks in the optical absorption spectrum in figure 5.4. The plasmon peak at 520 nm (2.4 eV) is the transverse plasmon mode for Au nanorods, and is present in spherical particles at the same energy. The much broader peak is due to the longitudinal modes, with wavelength maximum depending on the aspect ratio. To obtain a single-nanoparticle

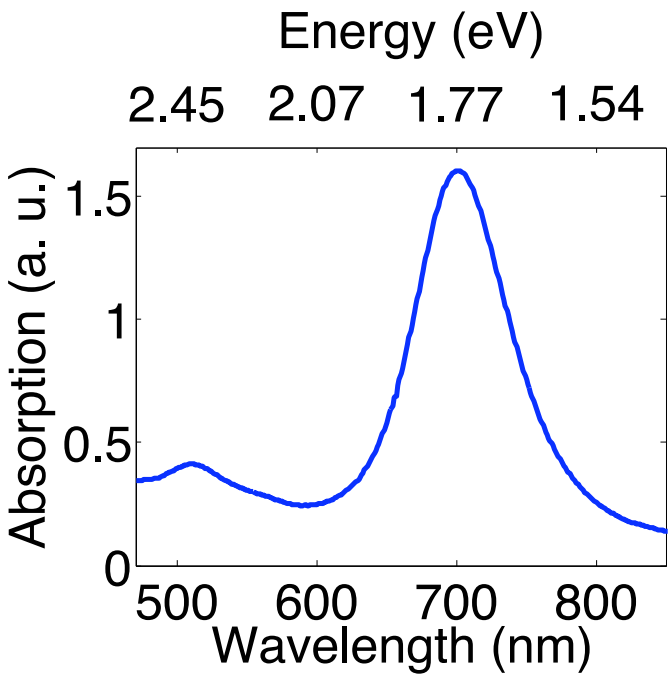

Figure 3.12: Ensemble optical absorption spectrum of solution. The 1^{st} peak at 520nm is the main surface plasmon absorption of Au and the 2^{nd} is to the longitudinal absorption of the nanorods, the observed broadening is due to the polydispersity of the sample.

spectrum we selected a nanorod 40 nm long and 10 nm wide; again the electron beam was positioned at the edge of the rod, as shown in figure 3.13 to induce charge oscillations along the axes of the rod. Figure 3.14 shows the resulting spectrum; the longitudinal plasmon resonance maximum is located at 1.74 eV corresponding to the theoretical value of an AR equal to 4 [16];the transverse plasmon mode is located at 2.47 eV.

Metal nanoparticle plasmon modes can also be affected by near-field interparticle coupling [51, 52]. Figure 3.15 shows two nanorods separated by a 10 nm gap. We measured the energy loss in the gap and at the edge of the particles at close proximity; deconvoluted spectra are shown in figure 3.16.

Previous investigations [51, 52, 53] have shown that the plasmon resonance of two electromagnetically coupled particles is shifted to lower frequencies or lower energy. The peak shift dependence on particle proximity can be interpreted by a simple dipole-dipole interaction. The spectra in figure (3.16) show that the resonance peak is red shifted when the particle is excited at the edge of either rod. This shift is due to the weakened restoring forces on the oscillating charge: the electron beam at one edge pushes the negative charges toward the other edge. These negative charges in turn induce the same effect on the second nanorod. Thus negative charges near the gap face positive charges, effectively lessening the net restoring effect and shifting the mode to lower energy. When the electron beam is positioned in the gap between the two particles, the energy loss peak amplitude is slightly larger, which may be due to local field enhancement. Additionally, we see that the peak is slightly blue shifted relative to excitation at the edge. This is attributed to the increased restoring force present with excitation in the gap, although microscopic calculations of the EELS spectra for coupled nanoparticles is required for a detailed understanding of the peak shifts.

We now turn to a discussion of the relation between EEL spectra and optical measurements. Pines and Bohm [23] first suggested that the energy losses suffered by electrons passing near or through a small metallic object are due to the excitation of surface plasmons. Subsequent theoretical work addressed energy loss in thin films [11], metallic spheroids (sufficiently small that retardation effects may be neglected) [22], and fully relativistic calculations of energy loss [30]. In order to interpret our experiments, we consider the nanowires and nanorods to be reasonably approximated

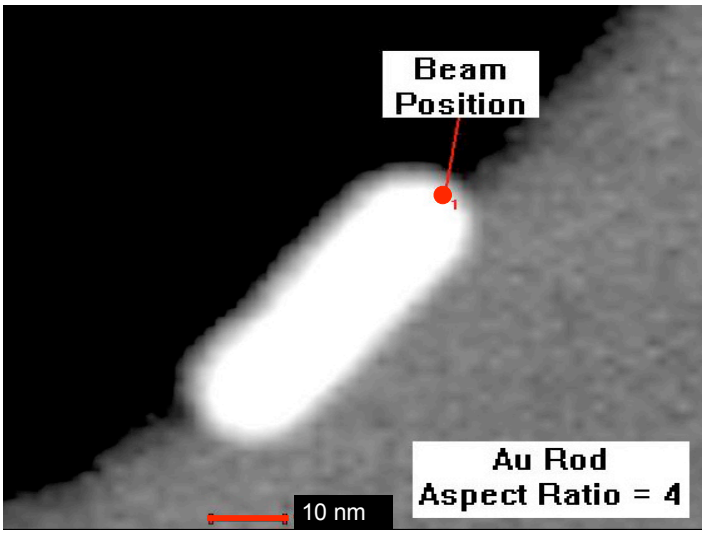

Figure 3.13: (a) TEM image of a single Au rod 40nm long and 10nm wide with electron beam position indicated by the small red circle a the tip of the particle.

as prolate spheroids of varying aspect ratio.

Our aim here is to compare energy loss spectra calculated from $\mathrm{Im}\left(\frac{1}{\epsilon_p(\omega)}\right)$ and from the analytical energy loss probability calculated for prolate spheroids, and to relate these to optical absorption spectra.

We begin with the imaginary part of the inverse dielectric function [21] - the energy loss function $\mathrm{Im}\left(\frac{1}{\epsilon_p(\omega)}\right)$ - where the frequency-dependent dielectric function $\epsilon_p(\omega)$ of the prolate spheroid is derived using the electrostatic approximation [10] as detailed in section 1.3.1. The dielectric function of a prolate spheroid is expressed as:

$$\epsilon_p \sim 1 + \alpha, \tag{3.1}$$

where α is the polarizability of the prolate particle; see equation 1.39. We take the energy loss probability derived in section 2.2.3 equation 2.26 for an electron with

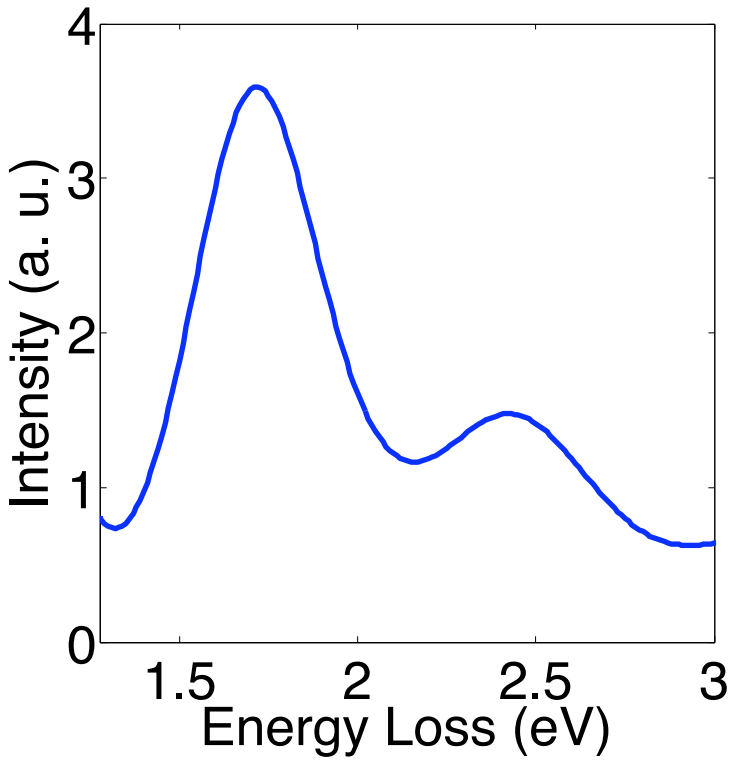

Figure 3.14: deconvoluted Spectrum of a single nanorod. Both plasmon peaks are resolved: the longitudinal plasmon peak is at 1.74 eV and the transverse peak is at 2.47 eV.

constant velocity v and impact parameter b passing a prolate spheroid traveling parallel its minor axis:

$$\Gamma_{loss}(\omega) = \frac{2}{v\omega}\sum_{l=1}^{\infty}\sum_{m=0}^{l} C_{lm}\frac{P_{lm}(\eta_o)}{Q_{lm}(\eta_o)}J^2_{l+1/2}\left(\frac{a\omega}{v}\right)K^2_m\left(\frac{b\omega}{v}\right) \times Im[\alpha_{lm}(\omega)] \tag{3.2}$$

where a is the focal length of the confocal spheroid, η_o depends on the aspect ratio ρ of the particle and is given by:

$$\eta_o = \frac{1}{\sqrt{\rho^2 - 1}}$$

$\mathrm{Im}[\alpha_{lm}(\omega)]$ is the imaginary part of $\alpha_{lm}(\omega)$, $\alpha_{lm}(\omega) = \frac{\epsilon(\omega)-1-[\epsilon_m(\omega)-1]\beta_{lm}}{\epsilon(\omega)-\epsilon_m(\omega)\beta_{lm}}$ and

$$C_{lm} = (-1)^m(2-\delta_{0m})(2l+1)$$

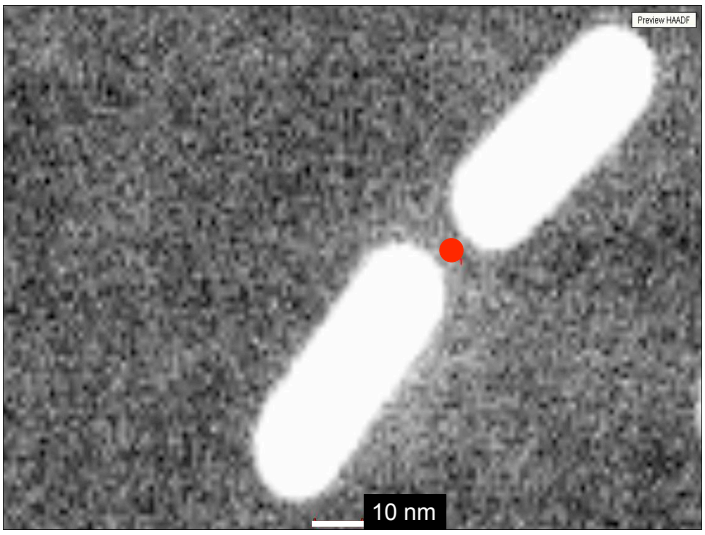

Figure 3.15: Two nanorods (dipole) positioned with a 10-nm gap.

with, $\delta_{0m} = 1$ if $m = 0$ or 0 for $m \neq 0$. Finally,

$$\beta_{lm} = \frac{Q'_{lm}(\eta_o)P_{lm}(\eta_o)}{P'_{lm}(\eta_o)Q_{lm}(\eta_o)} \tag{3.3}$$

is the surface plasmon eigenvalue for the (l, m) mode of the dielectric function and real and negative number, P_{lm} and Q_{lm} are the associated Legendre functions of the first and second kinds respectively; $J_{l+\frac{1}{2}}$ is a the ordinary Bessel function of order $l + \frac{1}{2}$ and K_m is the modified Bessel function of order m.

In figure (3.17), we plot together the optical absorption of the prolate spheroid here taken as [10, 6]:

$$Im(1 + \alpha) \tag{3.4}$$

for the transverse and longitudinal axis, the energy loss probability equation from (3.2), and the size dependent $\mathrm{Im}\left(\frac{1}{\epsilon_p(\omega)}\right)$. The medium dielectric is kept constant

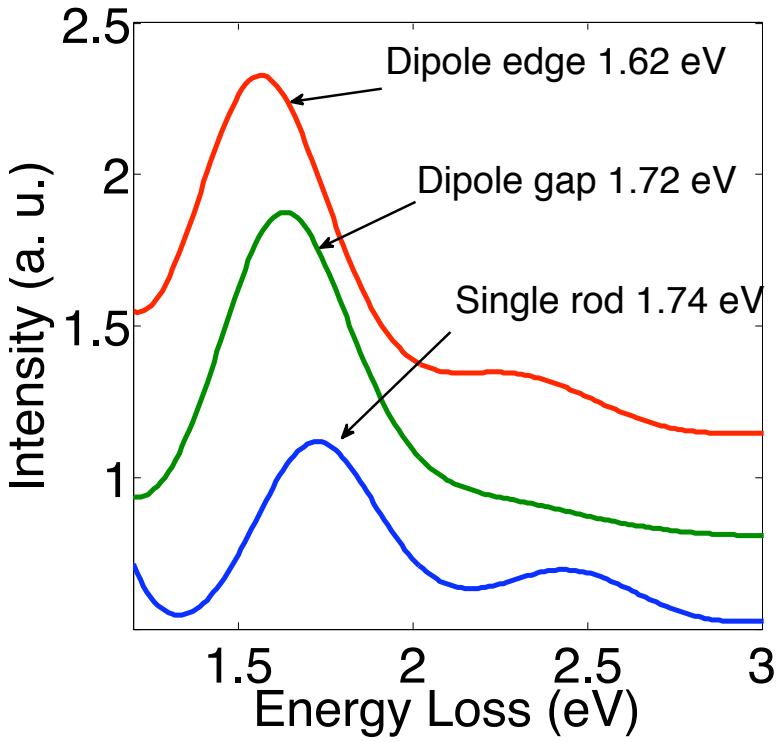

Figure 3.16: Deconvoluted spectra of the dipole taken at the edge and in the gap between the two rods along with that of the single nanorod fig 3.14. The plasmon peak at the edge of the dipole is 1.62 eV and 1.72 eV in the gap both peaks are red shifted compared to the single rod plasmon peak but the shift is smaller for excitation in the gap.

($\epsilon_m = 1$), and the Drude dielectric function

$$\epsilon(\omega) = 1 - \frac{\omega_p^2}{\omega(\omega + i\gamma)},$$

has been used for the material response. Although in principle the interband contribution to the dielectric constant for Au should be included, the Drude model does give a very good approximation to the Au plasma frequency since the free-carrier contribution is much larger than the interband part of the dielectric constant, as indicated by Dressel and Grüner [31]. We have selected parameters appropriate for Au ($\omega_p = 2.5\ eV$, $\gamma = 1.06$), the effect of the aspect ratio is shown ($\rho = 4,\ 4.5$, and

5). Atomic Units are used (a.u., i.e., $e = m = \hbar = 1$)

It is apparent in figure (3.17) that the EELS and optical measurements are sensitive to the same modes, and each clearly resolves the longitudinal and transverse modes of the structures. Furthermore, the red shift of the longitudinal plasmon peak with increasing aspect ratio is also manifested in all three approaches. Nevertheless, important differences are apparent. The spectral peak position of the optical absorption $\mathrm{Im}(\epsilon_p)$, the loss function $\mathrm{Im}(\frac{1}{\epsilon_p})$, and the loss probability Γ_{loss}, do not exactly coincide. The loss function and the loss probability longitudinal peaks are blue-shifted relative to the longitudinal peak of the optical absorption. Their transverse peaks also show less dependence on the aspect ratio than the transverse optical absorption peak. The energy loss expressions $\Gamma_{loss}(\omega)$, and $\mathrm{Im}\left(\frac{1}{\epsilon_p(\omega)}\right)$ for a prolate spheroid with $\rho = 4$, show longitudinal peaks at 1.6 eV and 1.76 eV respectively and transverse peak between 2.4 and 2.5 eV. These values agree quite well with our experimental values for the Au nanorod with the same ρ displayed in figure 3.14.

3.4 Conclusion

The primary consequence of this work is that the dielectric function of metallic nanostructures can be deduced from an EELS experiment, and the mode structure required for understanding or engineering optical plasmonic interactions can be accomplished through EELS measurements of single nanoparticles. Most importantly we've shown that optics and EELS are in many ways complimentary: optic measurements are good for high spectral resolution, but are limited in spatial resolution even with near-field techniques. TEM/EELS is good for nanometer scale imaging

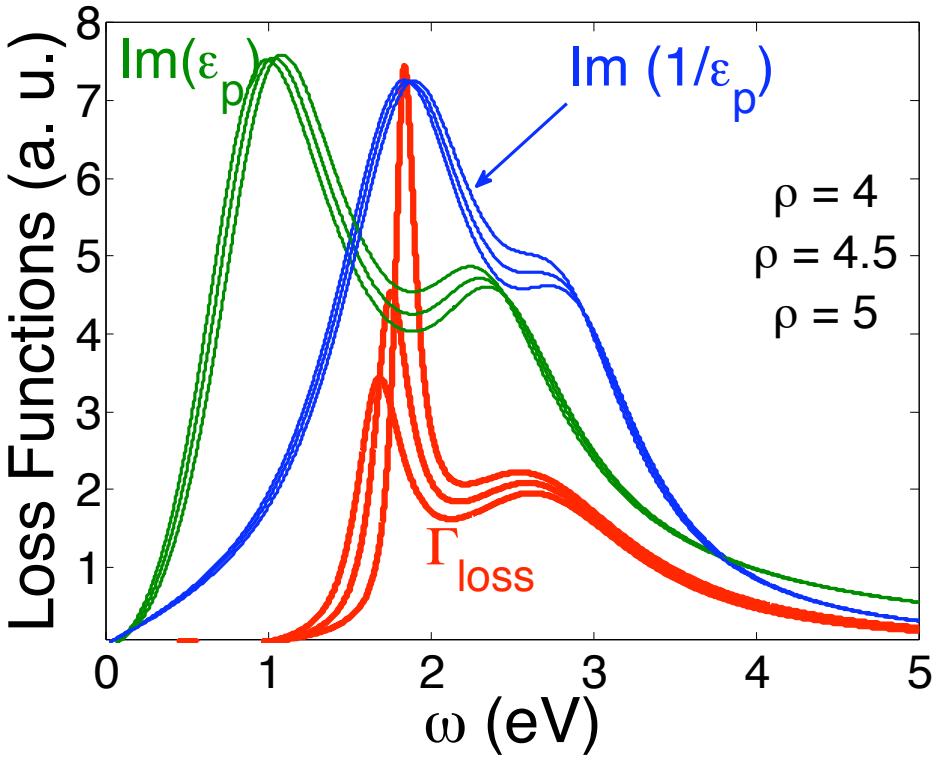

Figure 3.17: Comparison between analytical representations of the energy loss peak for 3 Au prolate spheroids. For all expressions we set the host dielectric $\epsilon_m = 1$ and the damping coefficient for the Drude model for dielectric $\gamma = 1.06$. The aspect ratio ρ is varied to show its influence on the plasmon peak absorption.

and thus for detailed mapping in of plasmon modes in nanostructures. Although EELS can distinguish different plasmon modes, it cannot yet produce meaningful measurements of the spectral line width or shape. Optical frequency modes are accessible via both techniques, and thus give us access to the full dielectric behavior of nanostructures, but a complete description still requires both. Indeed, we expect that the intersection of optics and EELS will be a remarkably fruitful area of research in plasmonics in the near future.

CHAPTER IV

Electron Beam Mapping of Plasmon Resonances of Electromagnetically Coupled Gold Nanorods

4.1 Introduction

Knowledge of spatial characteristics of surface plasmon (SP) modes in noble metal nanoparticles and nanostructures is essential for a direct control of electric field confinement in the near-field. Experimental methodologies such as near field optics and electron microscopy serve as powerful basic tools for investigation of plasmonic interactions. SP are electromagnetic excitations propagating at the interface between a dielectric and a conductor. They arise via the coupling of optical fields to oscillations of the conductor's electron plasma. Physically, these oscillations can be induced by either the driving electric field of an incident resonant optical field or impulsively by the transient field associated with a fast electron passing near a nanoparticle.

SP are used for a variety of applications like guiding electromagnetic energy in subwavelength-sized optoelectronic devices [54], enhanced fluorescence spectroscopy [55], Raman spectroscopy [56, 57], near-field imaging [58], and biosensing [59].

Electron energy loss spectroscopy (EELS) in a transmission electron microscope

(TEM) can be used to obtain the SP spectrum by analyzing the energy of initially quasi-mono-energetic electrons, after they have interacted with a sample [41]. State of the art electron microscopy has achieved spatial resolution as low as 0.1 nm and energy resolution as low as ~ 0.2 eV [48]. For this reason, the optical plasmon modes of metallic nanoparticles have recently become accessible using EELS.

We have demonstrated in chapter III that the dielectric function of metallic nanostructures and the mode structure required for understanding or engineering optical plasmons of a single nanoparticle can be determined via EELS [39, 60, 61]. Of course, engineered nanostructures are getting more complex, involving the coupling of simple elements to enable new functionality such as negative index materials [62]. For this reason, a number of optical spectroscopy techniques [37, 38] and theoretical analyses have been used to study the distance dependance of near field interactions between coupled systems, using both near and far field detection. Hao et al.[25] theoretically considered metallic nanostructures of different shapes and sizes. Experimental studies have investigated coupled gold (Au) nanodisks in an array [52] and single nanoparticle pairs [51, 63]. To date few attempts using EELS have been made to study coupled nanoparticles and particularly their effect on the surface plasmon modes and their ability to produce high field enhancements.

In this chapter, we take the next step beyond single particle analysis [60, 64], and investigate the effects of electromagnetic coupling on the SP modes of metallic nanoparticles using EELS in scanning TEM (STEM) mode. We employ energy-filtered imaging (EFTEM) in order to map their SP response. We then compare the energy loss results to the calculated optical response of the same particle arrangement using the

discrete dipole approximation (DDA) method [65]

We employ energy-filtered imaging (EFTEM) in order to map their SP response. EFTEM imaging was carried out within an energy loss range of 1 – 5 eV using a monochromated electron beam in combination with an energy window of 0.2 eV. Whereas the STEM/EELS mapping technique has previously been used to observe the SP energy and distribution of single Au nanoparticles [61], we employ EFTEM mapping to study coupled Au nanorods and to show the plasmon mode dependence on particle proximity and to reveal field enhancement effects that arise due to their interaction.

4.2 Experiment

4.2.1 Synthesis of Gold Nanorods

The Au nanoparticles were fabricated using a seeding growth method to make varied aspect ratio gold and silver nanorods[36, 43]. The rod aspect ratio could be controlled from 1 to 7 by simply varying the ratio of seed to metal salt in the presence of a rod like micellar template[44]. It is observed that the use of additives such as $AgNO_3$ and cyclohexane strongly influenced the gold nanorod formation. The cylindrical shape of the Au rods in figure 3.13 is distinctly different from an earlier observed needlelike shape. This method requires no nano-porous template and therefore may be more practical for large-scale synthesis.

The sample of Au nanoparticles used in our experiment contains nanorods with aspect ratio 4.6 ± 1. They are prepared in a clean test tube, 10 mL of growth solution, containing 2.5×10^{-4} M $HAuCl_4$ and 0.1 M cetyltrimethylammonium bromide

(CTAB), was mixed with 0.05 mL of 0.1 M freshly prepared ascorbic acid solution, next 0.025 mL of the 3.5 nm seed solution is added. No further stirring or agitation was done. Within 5-10 min, the solution color changed to reddish brown. The solution contained 4.6 aspect ratio rods, spheres, and some plates shown in figure 4.1.

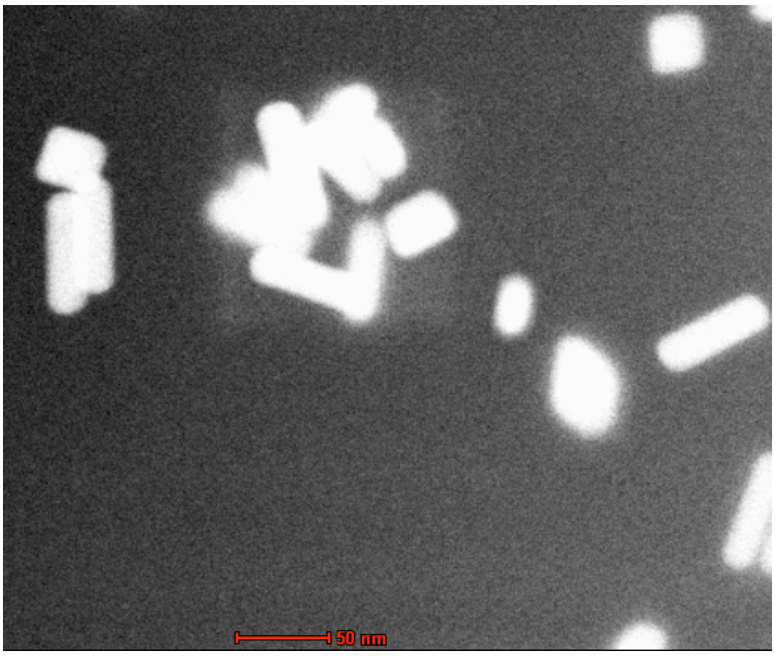

Figure 4.1: TEM images of 4.6 aspect ratio gold nanorods

4.2.2 Energy Filtered Transmission Electron Microscopy

If a very thin sample is illuminated with a beam of high-energy electrons, then a majority of the electrons will pass unhindered through the sample but some will interact with the sample, being scattered elastically or inelastically (phonon scattering, plasmon scattering or inner shell ionisation). Inelastic scattering results in both a loss of energy and a change in momentum, which in the case of plasmon or low

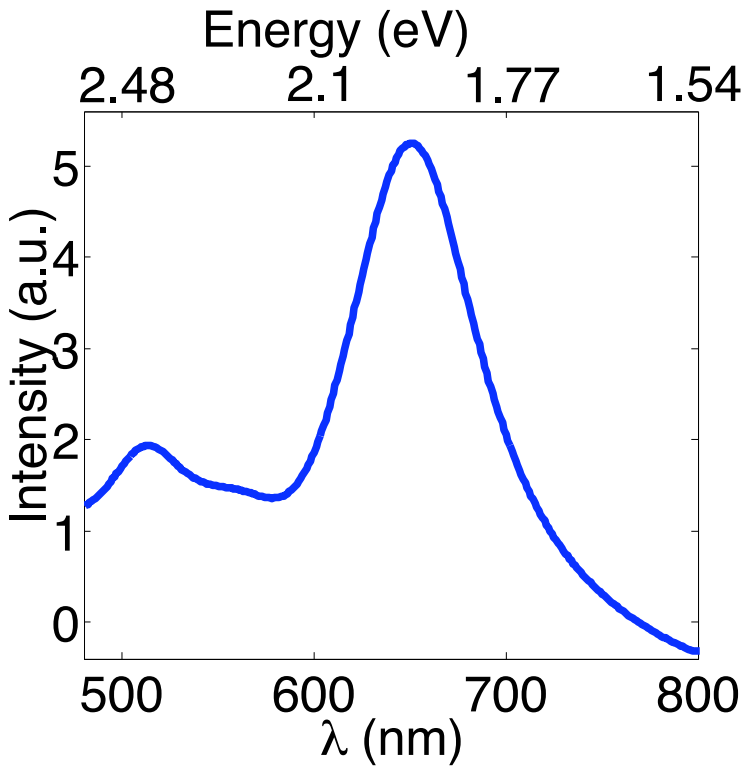

Figure 4.2: Ensemble UV-Vis absorption spectrum of Au nanorod solution. The first peak at 520 nm ($\sim$ $2.4eV$) is the main surface plasmon absorption of Au and the second is to the longitudinal absorption of the nanorods. The observed broadening is due to the polydispersity of the sample.

energy is characteristic of the element in the sample. If the electron beam emerging from the sample is passed through a magnetic prism, then the flight path of the electrons will vary depending on their energy. This technique is used to form spectra in EELS (this is discussed in more details in section 3.2.2), but it is also possible to place an adjustable slit to allow only electrons with a certain range of energies through, and reform an image using these electrons on a detector [66]. The energy slit can be adjusted so as to only allow electrons which have not lost energy to pass through to form the image. This prevents inelastic scattering from contributing to the image, and hence produces an enhanced contrast image [67]. Adjusting the slit to only allow electrons which have lost a specific amount of energy can be used to obtain elementally sensitive images. As the ionisation signal is often significantly smaller than the background signal, it is normally necessary to obtain more than one image at varying energies to remove the background effect. The simplest method is known as the jump ratio technique, where an image recorded using electrons at the energy of the maximum of the energy loss peak caused is divided by an image recorded just before the plasmon energy. It is often necessary to cross-correlate the images to compensate for relative drift of the sample between the two images. Improved elemental maps can be obtained by taking a series of images, allowing quantitative analysis and improved accuracy of mapping where more than one element is involved. By taking a series of images, it is also possible to extract the EELS profile from particular features.

EEL spectra and energy-filtered images are obtained using a modified FEI Titan 80-300 microscope equipped with a special high-brightness Schottky-field emission

electron source, a gun monochromator, a high-resolution GIF Tridiem energy-filter, and two CEOS hexapole-type spherical aberration correctors.

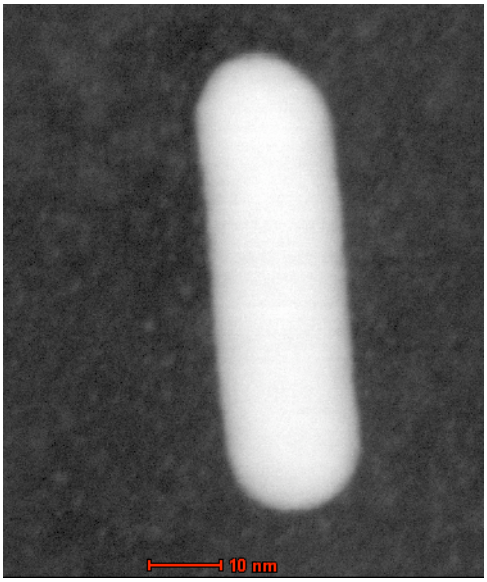

Figure 4.3: single Au nanorod with aspect ratio of ~ 3

4.3 Results and Discussion

The experimental EEL spectrum of a single nanorod 70 nm long and 28 nm wide is shown in figure 4.3. The two plasmon peaks characteristic to nanorods are displayed; the transverse peak at 2.4 eV and the longitudinal at 1.9 eV displayed in figure 4.7.

The experimental EEL spectra of two identical Au nanorods are shown in figures 4.4 and 4.5. Figure 4.7 displays their corresponding spectra plotted together with that of the single rod. The peak positions exhibit a significant redshift compared to the single isolated particle peak; the longitudinal peaks shift from 1.9 eV (650 nm) to 1.3 eV (950 nm) due to the coupling, and the transverse peaks also experience a

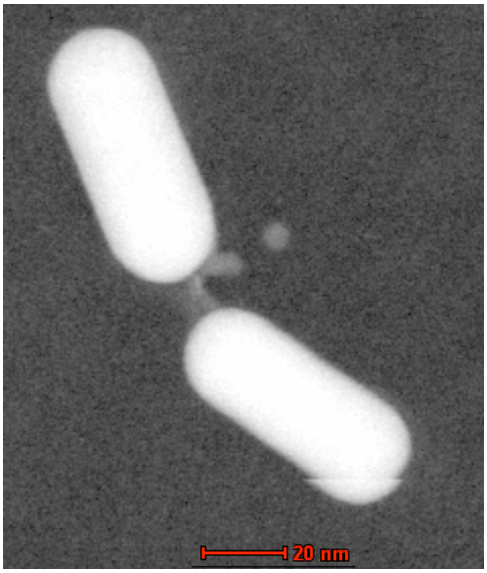

Figure 4.4: Dimer 1; pair of identical nanorod forming an angle dipole with a gap ~ 10 nm.

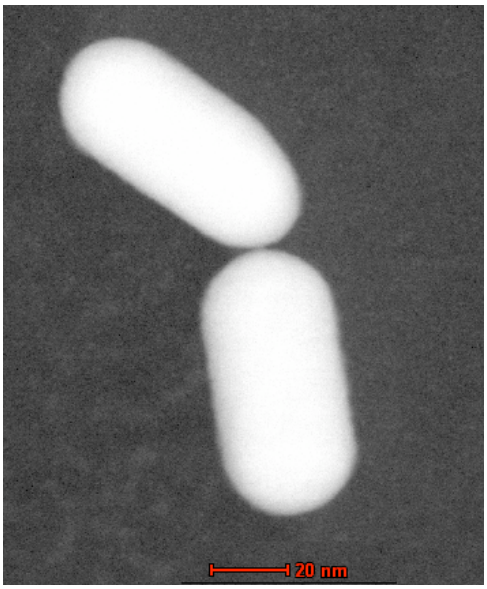

Figure 4.5: Dimer 2; angle dipole with separation ~ 1 nm.

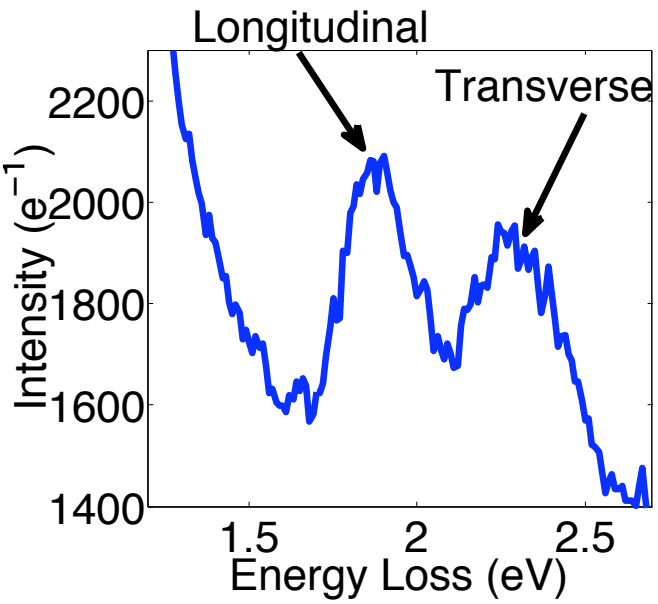

Figure 4.6: energy loss spectrum of a single Au nanorod the transverse peak is at 2.4 eV and the longitudinal peak is at 1.8 eV.

slight but noticeable redshift. Similar shifts to lower resonance energies have been demonstrated, when the nanoparticles are separated by a gap less than 10 nm, by a number of optical measurements on nanospheres and nanotriangles [52, 51, 63], and theoretically by Hao and Schatz [25] for spheroidal nanoparticles. We also observe a distinct increase in the amplitude of the longitudinal peak; this is attributed to the local field enhancement that occurs when nanostructures are close enough to strongly interact [25, 68].

We next use EFTEM to image the spatial distribution of the plasmon modes around the nanorods. Figure 4.8(a) shows the longitudinal and transverse plasmon modes respectively of a single Au nanorod. Although methods have been developed to calculate the energy loss of an electron beam (see for example [22, 30]) it is interesting to investigate the relation between the spatial distribution of the energy loss prob-

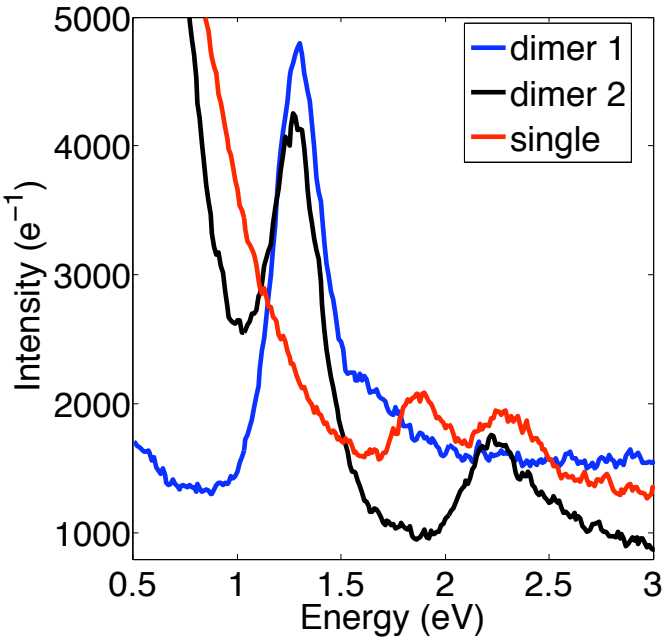

Figure 4.7: the electron loss spectra of coupled nanorods compared to the single nanoparticle spectrum. The dipole formations show a significant redshift of the longitudinal plasmon peak and a larger number of electron count largely attributed to high concentration of fields at the gap; confirming the large field enhancement at the dipole gap.

ability and the optical plasmon mode profile. To this end, we compare our energy loss data with the theoretical distribution of the electromagnetic field around the particles obtained via the discrete dipole approximation (DDA) method [25].

All DDA calculations are performed using DDSCAT 7.0 [69] where the grid spacing is fixed at 1 nm. The refractive index of water is 1.331 and gold dielectric constants are from Johnson & Christy [19]. Figures 4.8(b) shows the electric field distribution around a single gold rod 70 nm long and 28 nm wide in vacuum. The Au nanoparticle is simulated by a rod with two half-sphere caps on both end, its dimensions are those of the Au nanorod used in the EELS spectral imaging in figure 4.3. The incident wavelength is 650 nm, when the electric field is parallel to the axis of the Au

rod, the longitudinal mode is excited. The square of the electric fields ($|E|^2$) around the rod are plotted. Both the EFTEM and the DDA calculations reveal that the longitudinal mode shows a concentration of fields at the end of the rods whereas the transverse mode displays more uniform fields along the nanoparticle.

Figure 4.9(a) shows the longitudinal and transverse field distributions of two nanorods with a $\sim$ 5 nm gap. Again, the two plasmon modes of interest are mapped quite clearly with the longitudinal plasmon at $\sim$ 1.4 eV and the transverse plasmon at $\sim$ 2.2 eV. The spatial mode of the longitudinal plasmon show similar characteristics as that of the calculated distribution in figure 4.9(b). They both show the same distribution of field at the edge of the particle and a higher concentration of field at the gap.

As a further test of the relation between electromagnetic mode profile and energy loss, we compare the decay of the surface plasmon intensity obtained from the experimental EELS spatial profile (figure 4.8(a)) to that obtained from the DDA method (figure 4.8(b)). Specifically, we plot the energy loss amplitude and the plasmon mode intensity measured from the tip of the nanorod in figure 4.8 at the longitudinal mode energy. The results in figure 4.10 show that the two decay length are very similar. These results confirm that EELS and optical techniques are complimentary in many ways. Most importantly, they bring us closer to the possibility to accurately predict the spatial distribution of enhanced localized plasmon modes in nanostructure arrays. This can have a significant impact for the design and fabrication of novel nano-plasmonics devices [70].

The EELS mode profiles are related to the optical mode intensity because the energy

lost by the incident electrons is determined by the electric fields that are induced on the nanoparticle. However, care should be taken for coupled particles when comparing field enhancements as there are important differences in the plasmon excitation mechanism for EELS and optical excitation. Optical excitation with a polarized resonant field induces a uniform field across the two particles. However, electron beam excitation is much more localized and induces charge displacement that varies in intensity and spatial structure as the beam location is changed, as illustrated in figure 4.11. For example, to characterize the plasmon mode at the gap between the nanorods, an optical excitation induces a symmetric charge distribution across the nanoparticles; positive and negative charges alternate at the edge of the structures thus weakening the restoring forces. On the other hand when the electron beam is scanned in the gap, it induces an antisymmetric charge distribution by repelling the negative charges from the tip of the nanorods. This formation in turn produces stronger restoring forces which in turn induces a blue shift of the plasmon peaks with respect to the optical excitation [60]. Furthermore, utilizing the nanoscale dimensions of the focused electron beam of the TEM, we are able to probe precise locations on and around the nanoparticle to isolate either plasmon peak or probe both plasmon resonances at once. Figure 4.12 shows three spectra collected from coupled nanorods at 3 different locations. The energy loss at the gap and edge of the structures are collected. The peak shift due to particle proximity as well as the field enhancement are made evident in these measurements. Figure 4.12 also shows that the electron beam can isolate each plasmon peak by inducing charge displacement along the corresponding axis.

4.4 Conclusion

In summary, we have demonstrated that EELS and EFTEM are viable methods to investigate and image the optical modes of metallic nanoparticles and coupled systems. We have shown that the spatial distribution of the plasmon modes obtained by electron spectroscopy and DDA simulation have similar characteristics. These results confirm that EELS and optics are in many ways complimentary and that access to a complete description of the optical and electrical characteristics of nanostructures, requires a combination of both techniques.

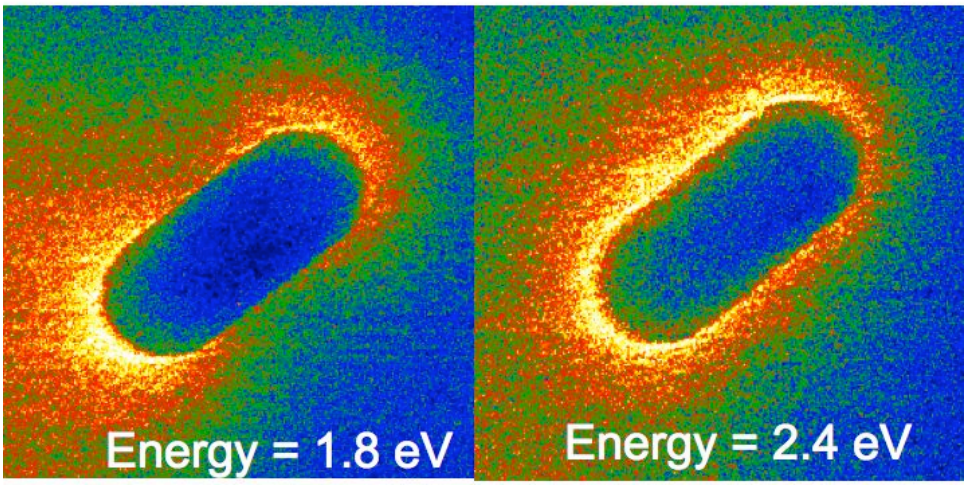

(a)

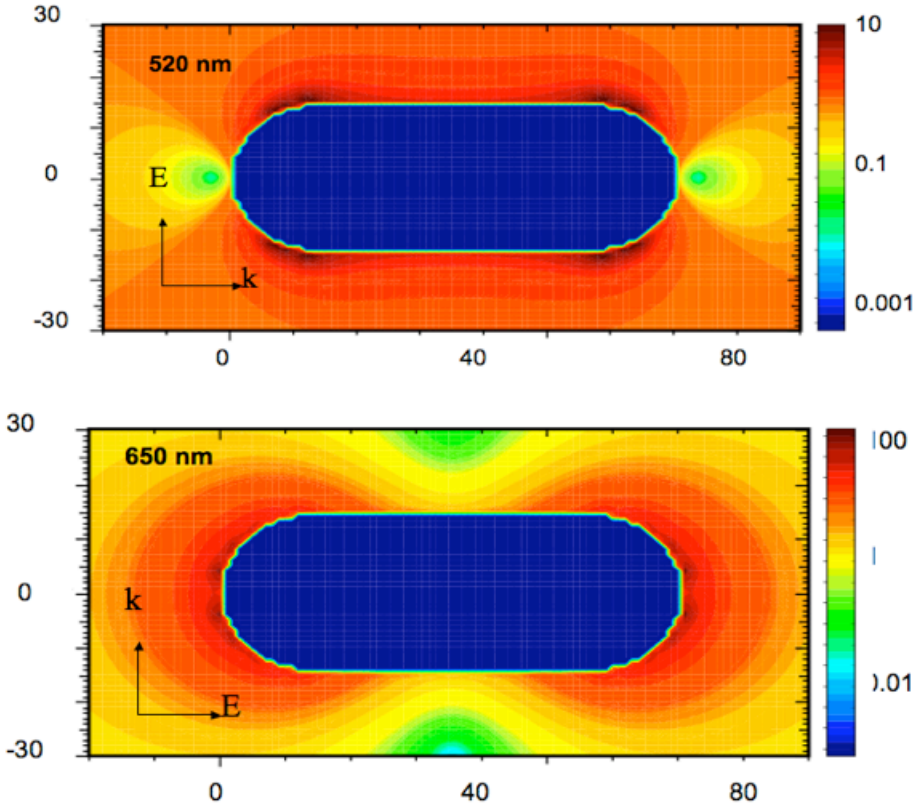

(b)

Figure 4.8: (a) EFTEM spectral map of the spatial variation of the longitudinal plasmon at 1.9 eV (corresponding to optical transition wavelength of ∼650nm) and the transverse plasmon 2.4 eV (520nm). (b) Theoretical distribution of the electromagnetic field around a single particle at 1.9 eV (650 nm) for the longitudinal plasmon and the transverse plasmon at 2.4 eV (520 nm).

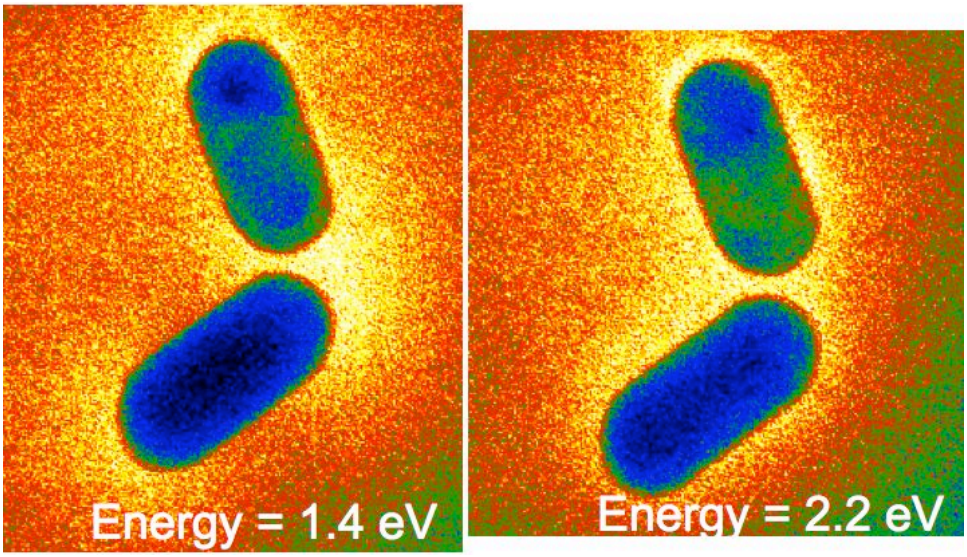

(a)

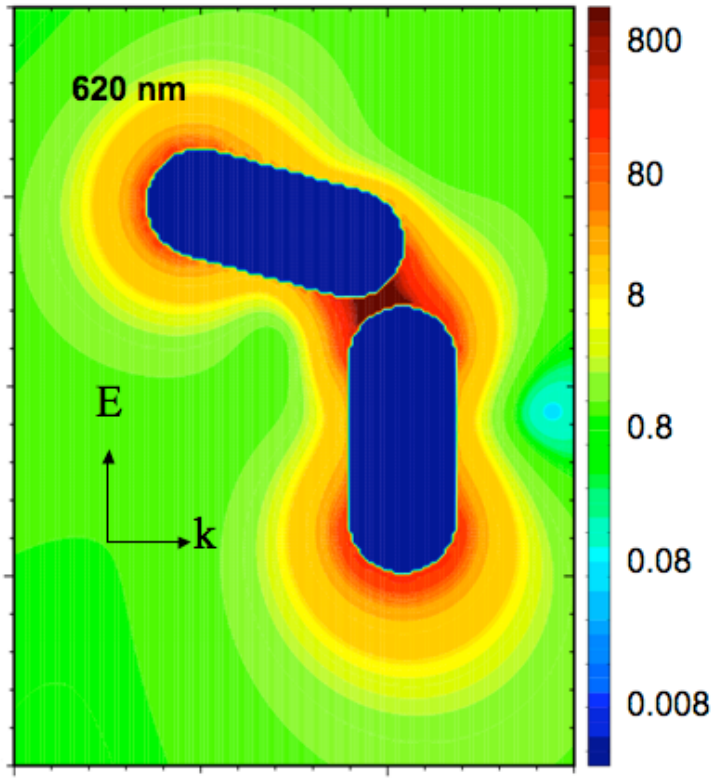

(b)

Figure 4.9: map of spatial mode of the longitudinal (1.4 eV) and transverse (2.2 eV) plasmon of a pair of Au nanorods at close proximity with a 5 nm gap. (b) Theoretical distribution of the longitudinal plasmon around the pair of Au nanorods.

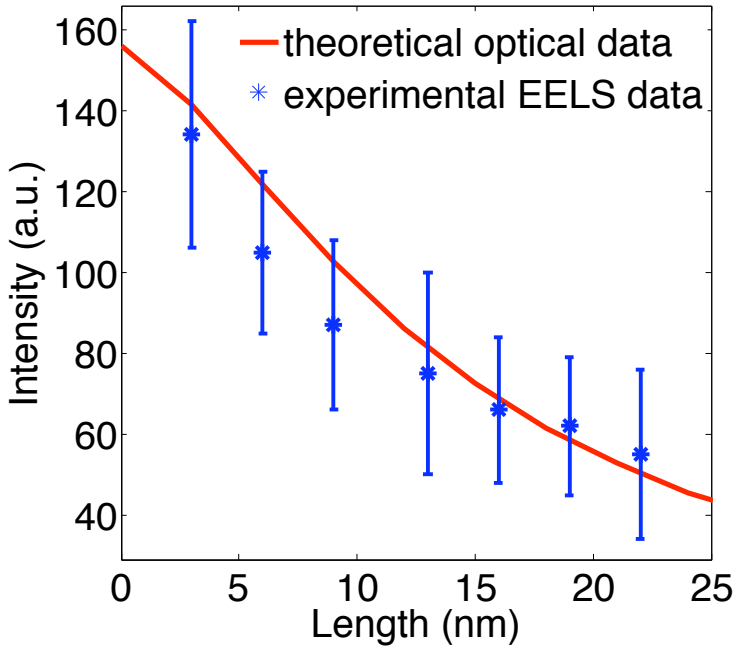

Figure 4.10: comparison of the decay of surface plasmon intensity of the experimental EELS data and the optical calculations obtained using the DDA method. The intensity decay is measured along the symmetric axis of the Au nanorod

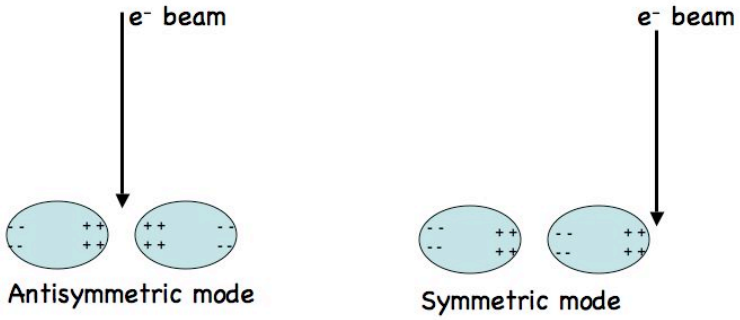

Figure 4.11: Sketch to illustrate the induced spatial charge structure between closely spaced nanoparticles, when exposed to an electron beam

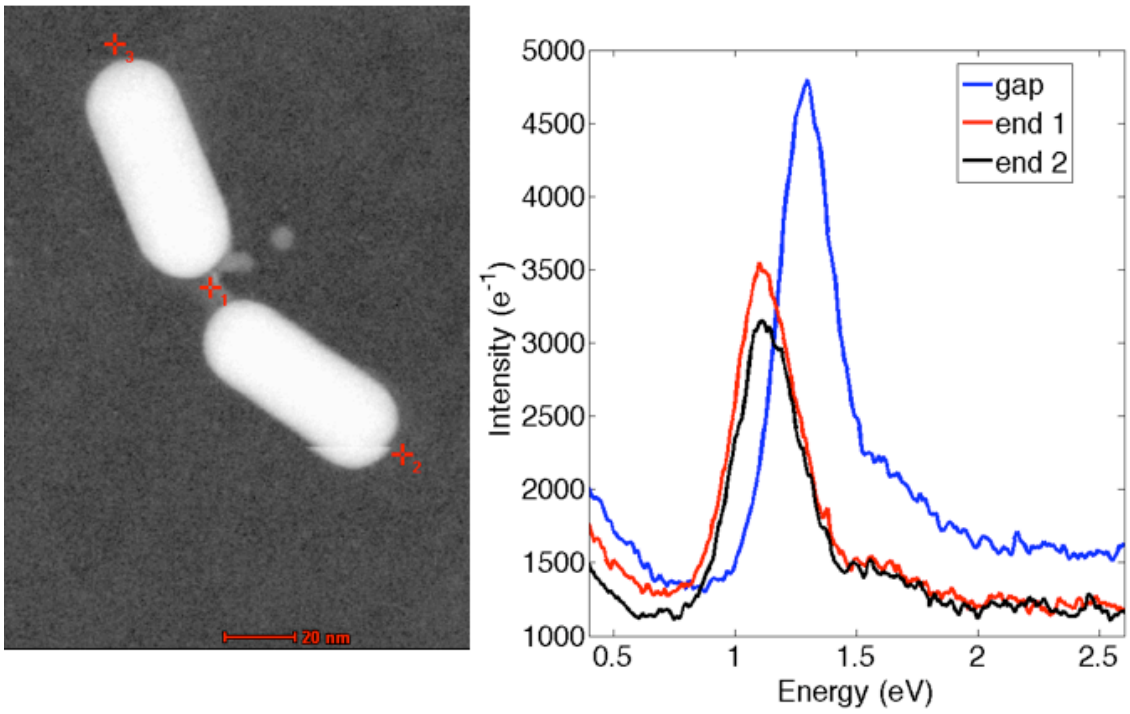

Figure 4.12: Spectra collected at the edge and gap of two nanorods at close proximity. This measurement also shows that the electron beam can induce charge displacement along one axis at a time, as it is demonstrated here for the longitudinal axis

CHAPTER V

Enhanced Surface Third Harmonic Generation from Gold Nanorods

5.1 Introduction

We've demonstrated that the light matter interaction that arises from the excitation of nanoparticles' plasmon mode, leads to high concentrations of optical fields in the close vicinity of the particles; see figure 4.8(a). In chapter IV, we also show that the electromagnetic coupling of Au nanorods at close proximity, leads to strongly enhanced field as displayed in figures 4.7 and 4.9(a). The local response of these Au nanostructures can therefore be used to enhance the incoming and generated fields for nonlinear processes. In this chapter, we explore the ability of Au nanorods to enhance the surface nonlinear response of materials, in particularly third harmonic generation (THG) produced at the surface of glass substrates.

THG is emerging as an important method to image transparent isotropic specimens in optical microscopy [71, 72]. This generally weak nonlinear process is dipole allowed and thus occurs in all materials including biological tissues. The image resolution and efficiency of this multiphoton microscopy largely depends on the intensity of the

signal produced at sample interfaces. Therefore, the need to enhance the signal is required to increase the yield in nonlinear microscopy. The enhancement of THG has been subject of several investigations [73, 74, 75, 76].

Tsang *et al* [77] have demonstrated that THG can be produced at any simple dielectric interface and that it is insensitive to the choice of laser wavelength. Most early investigations have shown that enhancement is obtained by matching the surface plasmon resonance of noble metal spheroidal nanoparticles with that of the TH produced from the surrounding material dielectric [78, 79, 74, 75] i.e. the pump or fundamental wavelength is in the infrared corresponding to a third harmonic signal in the visible matching the Mie frequency of gold nanoparticles. Advances in self assembly of colloidal nanoparticle provides us the opportunity to extend the wavelength at which the THG signal can be enhanced. Indeed, the development of new and powerful synthesis techniques has opened up the possibility of engineering methods that can easily tune the plasmon modes of nanostructures to be of the desired wavelength. The development of nanofabrication and self assembly based on wet chemistry methods has enabled synthesis of high yield (Au) and silver (Ag) colloidal particles with well defined structures specifically ellipsoidal nanoparticles [36]. These processes produce single nanoparticles with smooth surfaces and controllable aspect ratio. The ellipsoidal nanoparticles have two plasmon resonances, as demonstrated in detail in chapters I and III. One corresponds to the electron oscillation along the transverse axis of the rods, and has a resonance close to the plasmon mode of a spheroidal nanostructure. The second corresponds to a longitudinal oscillation along the long axis of the rod; it is red-shifted with respect to the transverse plasmon

and has a resonant frequency strongly dependent on the aspect ratio of the particle (which can be controlled during assembly). Noble metal nanoparticles, and Au especially, are ideal for applications in biological samples due to their low chemical reactivity while strongly interacting with light

In this chapter, we investigate the enhancement of TH signal by matching our fundamental laser signal with that of the longitudinal plasmon resonance of Au nanorods. We propose to use the focal point of a tightly focused ultrashort laser pulse, as a tool to probe isolated and clusters of nanoparticles. The variation in uniformity at the surface of the substrate containing the sample, is evidence of the presence of nanorods at different locations in the sample, translating to differences in THG intensities that are easily measured. Since the enhanced fields are concentrated at the edge of the nanorods as figure 4.8(a) shows, they can thus serve as a local probe of the dielectric environment within a few nanometers of the particle surface.

5.2 Third Harmonic Generation Using Focused Gaussian Beam

Consider a laser propagating in the z direction and tightly focused into a sample (figure 5.2). Using the theory of harmonic generation with focused Gaussian beam, we can calculate the intensity of the third harmonic light under the undepleted pump approximation. The THG power generated by such a beam is given by [80, 72]:

$$P_{3\omega} = k_{3\omega} k_{\omega}^{3} \Big(\frac{4\pi}{n_{3\omega} n_{\omega}^{2} c} \Big)^{2} P_{\omega}^{3} |J|^{2} \tag{5.1}$$

with P_ω the fundamental beam power, k_ω and $k_{3\omega}$ are the fundamental and third harmonic wave numbers, and the integral J is defined by:

$$J = \int_{z'_L}^{z'_R} \frac{\chi(z')e^{i\Delta k b z'}}{(1+2iz')^2} dz' \tag{5.2}$$

where χ is the third order susceptibility, $\Delta k = k_{3\omega} - 3k_\omega$ is the phase mismatch, $b = k_\omega \omega_0^2$ is the confocal parameter of the fundamental beam with waist radius of ω_0, $z' = x/b$ is the normalized coordinate along the optical axis measured from the beam wait position, and z'_L and z'_R are the normalized input and output planes coordinate respectively. In the case of an infinite, uniform nonlinear medium, this integral can be evaluated by contour integration. The result of this integration is somewhat surprising: The efficiency of THG in this limit vanishes for the case of positive phase mismatch ($\Delta k > 0$, which is the case of normally dispersive materials) and even for perfect phase matching ($\Delta k = 0$). The need for negative phase mismatch can be understood if we remember that a focused beam contains a collection of wave vectors in many directions. Three such wave vectors can add to give $k_{3\omega}$ only when $k_{3\omega} \leq 3k_\omega$ [80].

When the nonlinear medium is not uniform, either in the refractive index or in the nonlinear susceptibility, the THG signal does not vanish, and significant THG output can be obtained. For example, near an interface between two media with the same linear refractive index but with different nonlinear susceptibility it is shown (assuming $\Delta k b \ll 1$) that $P_{3\omega} \propto \delta\chi^2(1 + 4z_\omega^2/b^2)^{-1}$, where $\delta\chi$ is the difference in susceptibility values and z_ω is the distance between the interface and the beam waist [72]. Hence, as this interface is scanned along the optical axis the THG signal is generated efficiently when the interface is near the beam waist. The signal peaks

when the interface is at the beam waist position, and its full-width at half-maximum FWHM is b. When the linear index and the phase mismatch are also discontinuous at the interface, the beam parameters change across the interface, but the third harmonic is still generated efficiently only when the interface is located within one confocal parameter of the focal plane. Similarly, a thin film with a thickness t/b embedded in a homogeneous medium will generate a THG signal with

$$P_{3\omega} \propto \delta\chi^2(\frac{t}{b})^2(1+4z_\omega^2/b^2)^{-2} \tag{5.3}$$

Again we see that the signal is generated only when the film is near the focal plane, now with a FWHM of $0.64b$.

Thus the THG reported here, is produced in transmission at the interface of our sapphire substrate and air. This surface THG is a fundamental process occuring at all interfaces and is relatively free from the constraint of phase matching condition and wavelength restrictions [77, 80].

5.3 Experiment

We used a tightly focused high intensity ultrashort laser pulses to generate TH light at simple air-dielectric interface[77]. We produced a weak TH signal on the surface of a sapphire substrate that contains the sample. The tight focusing also allowed the laser beam to spatially discriminate the front and rear interface of the sapphire substrate. We confirmed that the detected signal is the third harmonic of the fundamental wavelength by showing the third power dependence of the emitted intensity with respect to the excitation intensity see figure 5.1. All our measurements were done at room temperature. The laser light was irradiated at a normal angle of

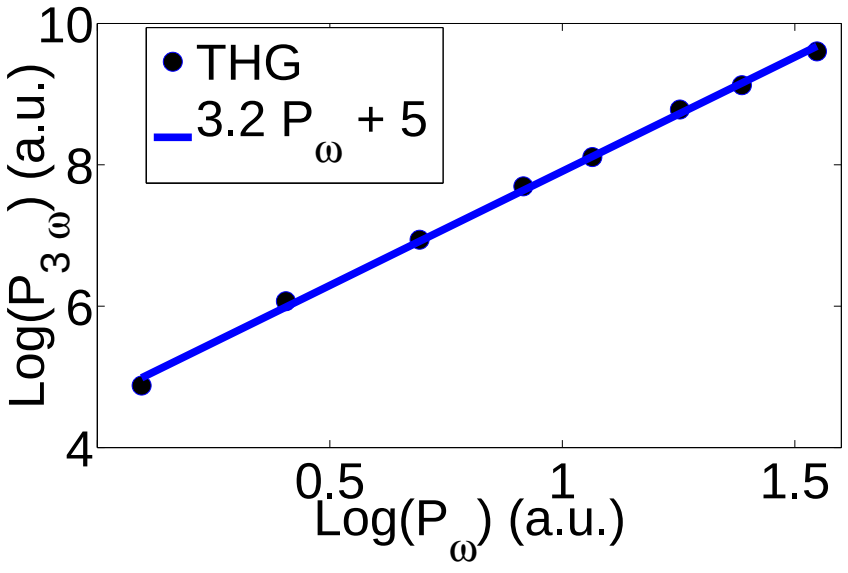

Figure 5.1: log-log plot of the Excitation power dependence of the measured THG signal measured over a single point within the scanned sample area: the surface of the sapphire substrate containing the Au nanorods

incidence at the sample surface. The laser beam was focused by a 40X microscope objective (N.A. = 0.6) to a $\sim 1\ \mu m$ spot that we rastered across the sample. The TH light was filtered out by two bandpass filters centered at 266 nm and detected by a photomultiplier tube and gated electronics; the experimental setup is shown in figure 5.2. The TH signal produced from the surface of the bare sapphire substrate has an average intensity more than 3 times than that of the background when no signal was turned on. For measurements of THG enhancement, a drop of diluted solution of the Au nanorods was evenly dispersed and dried on one surface of an epitaxially polished sapphire substrate. The Au nanorods were randomly oriented on the surface of the substrate as seen in figure 5.3. The fundamental signal was linearly polarized and parallel to the sample surface. This would drive electron oscillation along the

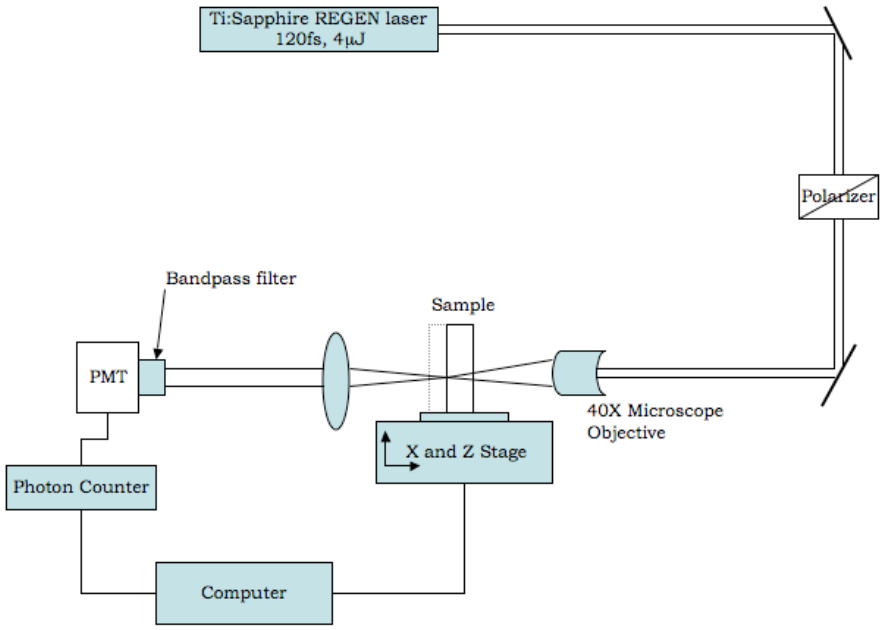

Figure 5.2: Experimental arrangement for third harmonic generation in transmission at the interface of a sapphire substrate and air

longitudinal axis of the nanorod that were aligned horizontally or vertical to the sample surface.

5.3.1 Synthesis of Gold Nanorods

The Au nanoparticles were fabricated using a seeding growth method to make varied aspect ratio gold and silver nanorods [36, 43]. The rod aspect ratio could be controlled from 1 to 7 by simply varying the ratio of seed to metal salt in the presence of a rod like micellar template [44]. It is observed that the use of additives such as $AgNO_3$ and cyclohexane strongly influenced the gold nanorod formation. The cylindrical shape of the Au rods in figure 3.13 is distinctly different from an

earlier observed needlelike shape. This method requires no nano-porous template and therefore may be more practical for large-scale synthesis.

The sample of Au nanoparticles used in our experiment contains nanorods with aspect ratio 4.6 $\pm$ 1. They are prepared in a clean test tube, 10 mL of growth solution, containing 2.5×10^{-4} M $HAuCl_4$ and 0.1 M cetyltrimethylammonium bromide (CTAB), was mixed with 0.05 mL of 0.1 M freshly prepared ascorbic acid solution, next 0.025 mL of the 3.5 nm seed solution is added. No further stirring or agitation was done. Within 5-10 min, the solution color changed to reddish brown. The solution contained 4.6 aspect ratio rods, spheres, and some plates shown in figure 5.3.

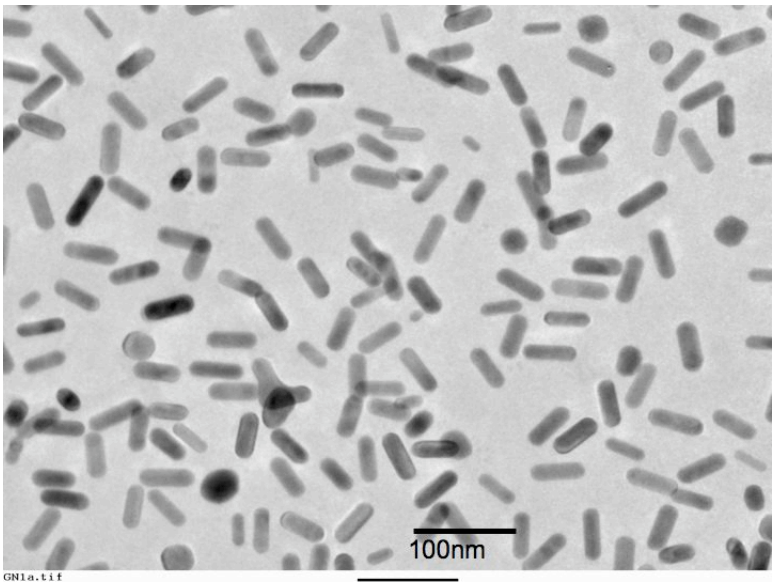

Figure 5.3: TEM image of an overview of the different size and shape Au nanorods present in the sample.

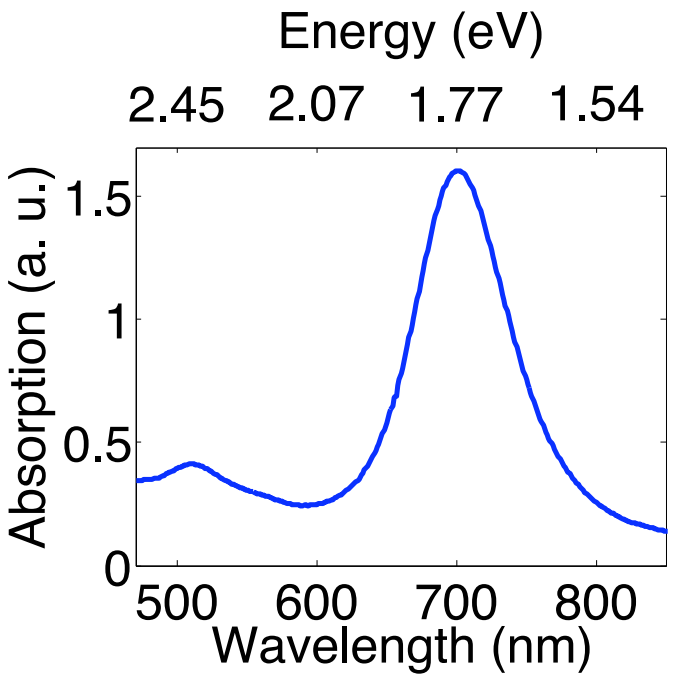

Figure 5.4: Ensemble optical absorption spectrum of solution. The 1^{st} peak at 520nm is the main surface plasmon absorption of Au and the 2^{nd} is to the longitudinal absorption of the nanorods, the observed broadening is due to the polydispersity of the sample.

5.3.2 Laser Systems

Our light source is a mode locked regenerative Ti:sapphire laser producing up to 4 μJ of energy at 800 nm center wavelength. The laser runs at a repetition rate of 250 KHz with a 120 fs pulse duration. The maximum average power delivered to the sample in our experiment is 120 μW, below the damage threshold of the Au sample [17].

The ultrafast laser based on Ti:Sapphire as a gain medium provides a wide tunability of its spectrum, and stability, which are all essential for the investigations of ultrafast dynamics such as SP dephasing time which are in the femtosecond regime. Such a laser system also delivers high peak power with relatively low average power, which

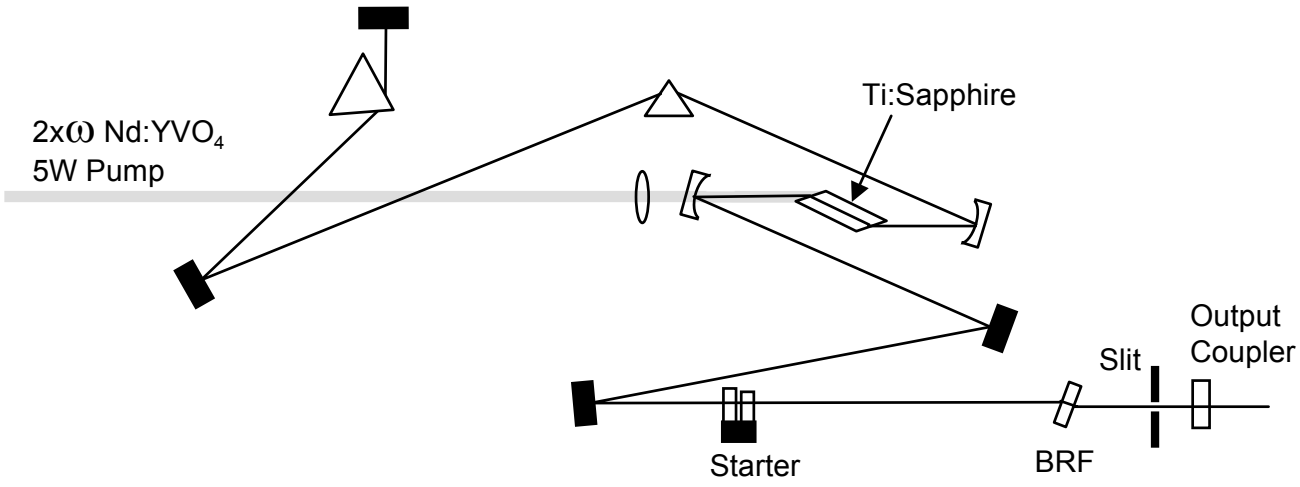

Figure 5.5: Ti:Sapphire Oscillator.

has enable non linear processes such as THG to have wider applicability in areas where its high light intensity requirement has been a limiting factor. The duration of generated ultrashort pulse enables the efficient coupling of the fundamental light to the plasmon generated signal [81].

We will first describe the workings of the oscillator, then the regenerative amplifier.

Ti:Sapphire Oscillator

The schematic diagram of our oscillator (Coherent MIRA) is shown in figure 5.5. The laser cavity is pumped by a 5 W continuous-wave frequency-doubled Nd:YVO_4 laser at 532 nm. The oscillator produces a 60 fs, 5 nJ energy pulse at 76 MHz repetition rate with average power of 400 mW at 800 nm center wavelength. The cavity is a standard astigmatically-compensated Z-cavity. Although the center wavelength of the output laser beam can be tunable by changing the birefringent filter at the

end of the cavity, it is usually set to 800 nm with a typical spectral bandwidth of 25 nm. The tuning range of our oscillator is limited by the bandwidth of the mirrors rather than the gain spectrum of Ti:Sapphire crystal which covers a wide band from 770 nm to 875 nm. The accumulating intra-cavity dispersion is compensated by the anti-parallel equilateral SF-10 prisms.

The laser is mode-locked due to the Kerr-lens mode-locking which is induced by a combination of the third-order process of the self-focusing and the spatial beam-loss modulation by the end slit as a hard aperture.

Ti:Sapphire Regenative Amplifier

The chirped pulse amplification (CPA) method is used to amplify the ultrashort nJ pulse from the oscillator [82]. An ultrashort pulse from the oscillator is stretched in a temporal domain using a multi-pass holographic grating pair by a factor of 500 before the amplification. The temporal duration of the stretched pulse is a few hundreds of picosecond. This long pulse is then injected into the amplifier cavity, amplified, and ejected out of the cavity. The cavity output is then compressed in time to its original seed pulsewidth using another grating pair with opposite dispersion to that of the stretcher. Since the stretched pulse reduces the peak intensities in the cavity, it safely amplifies the high energy pluses without any nonlinearities or material breakdown. The CPA method thus enables the design of a compact high power table top laser, which has significantly contributed to the investigations of ultrafast phenomena in physics, biology, chemistry, and even nuclear fusion sciences. The schematic diagram of the regenerative amplifier systems (Coherent RegA) is

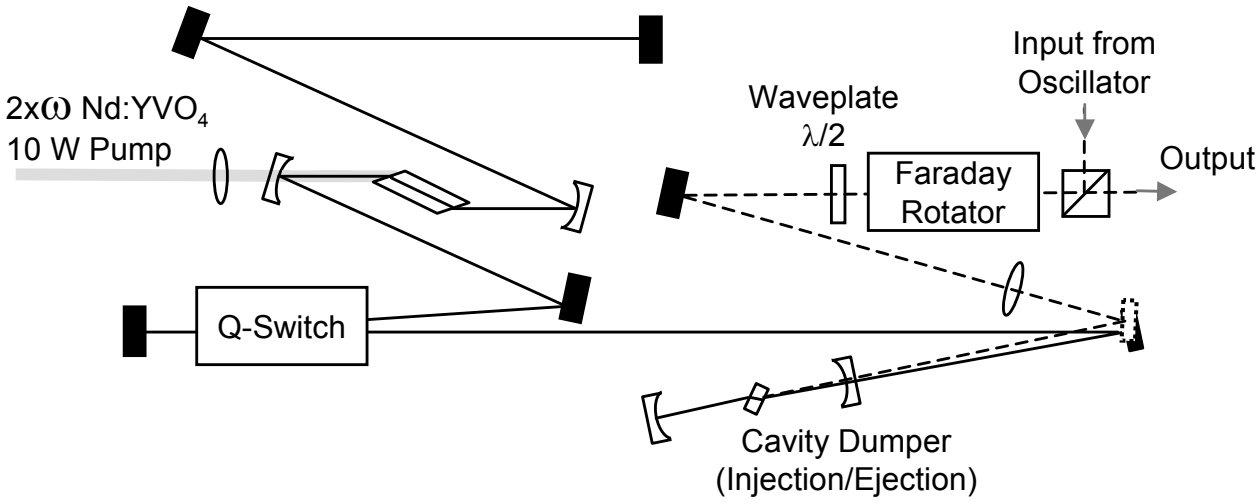

Figure 5.6: Ti:Sapphire Regenerative Amplifier.

shown in Fig. 5.6, which is the same standard Z-cavity design as the oscillator. Q-switching in the system sets the repetition rate at 250 kHz, which is determined by the Ti:Sapphire lifetime ~ 3 μs. While the Q-switch is closed, the population inversion in Ti:Sapphire is obtained so that the laser can not lase because of the low Q of the cavity. When the Q-switch is open, a stretched pulse from the oscillator is injected by a short RF-driven pulse through the acousto-optic Bragg cell cavity dumper. While the pulses are circulating in the cavity, factor of a few hundreds of amplification is achieved until they saturate the available Ti:Sapphire gain. Typical round trips of the injected pulses are twenty five. After saturation of the gain, the stretched pulse is ejected out of the cavity by the same Bragg cell in the cavity dumper. After passing through the Faraday isolator which isolates the back-reflection light from the oscillator, the ejected pulse is recompressed to 80 fs 5 μJ pulses at 250 kHz.

5.4 Results

During measurement, the beam focus is fixed and the TH signal is collected in transmission. The sample is scanned along the along the stationary beam in a 50 $\times$ 50 μm area with a 1 μm step. The rods were evenly distributed on the sample sapphire substrate closer to the detector as shown in figure 5.2 surface with random orientation. The same preparation procedures that have produced the nanorod distribution shown in figure 5.3, have been been followed to ensure a similar distribution at the surface of the sapphire substrate. We control the linear polarization of the fundamental signal with a half wave-plate. This allows us to isolate the nanorods whose longitudinal axis is perfectly vertical or horizontal accross the sample surface. Figure 2 shows the intensity of the third harmonic signal as a function of beam position on the sample for various laser polarization states. Hot spots are observed; these high intensities correspond to positions at which resonant single or cluster of nanorods are present on the surface. The THG signal is enhanced by up to several orders of magnitude relative to the bare surface THG signal; this is expected to occur when the plasmon resonance is near or at the laser frequency and when the nanorod axis is aligned with the incident laser polarization. The highest enhancement observed is $\sim$ 8.5 (3.8) $\times$ 10^3 for horizontal (vertical) linear polarization. To confirm that these large enhancements are due solely to the nanorods present in the scanned sample, we next use a circularly polarized fundamental signal controlled using a quarter wave-plate. This setup ideally produces no THG at an isotropic interface due to angular momentum conservation [83] but due to imperfection of the optics used, there is always a small portion of the signal that is linearly polarized.

Thus the circular polarization effectively diminishes the background signal due to the host dielectric [83, 84]. We first orient the quarter wave-plate such that it coincides with the direction of the maximum TH light collection at the desired input laser power. The wave plate is then rotated to dramatically, reduce and in some case eliminate the background signal, this corresponds to the minimum TH signal intensity collected (~ 5 counts). This effectively guaranties that the intense TH light collected during the scan is solely due to the surface plasmon oscillation along the axes with plasmon resonance at the laser wavelength.

The high field concentration at the tip and immediately at the vicinity of the nanostructure probes the surrounding dielectric material to produce the high yield TH light. This effect happens no matter the orientation of the nanorods. This is displayed in figure 5.8, the circularly polarized light produces enhancement from all relevant nanorods within the sample area. We should note that due to software limitations; that the scanned areas with very intense signal are assigned bright colors on the intensity graphs, this effect in turn overwhelms the dimmer colors assigned to lower intensity points thus effectively rendering them almost unreadable.

It is clear that the enhancement factor reported here is not just the effect of a single nanorod, the following is a rough calculation of the actual enhancement from each nanorod present in the laser spot. We estimate from figure 5.3 that there are ~ 150 nanorods present in the 1 μm diameter laser spot, we also assume the laser spot to be a perfect circle so that the intensity is:

$$I \sim \frac{E^2}{\pi r^2}$$

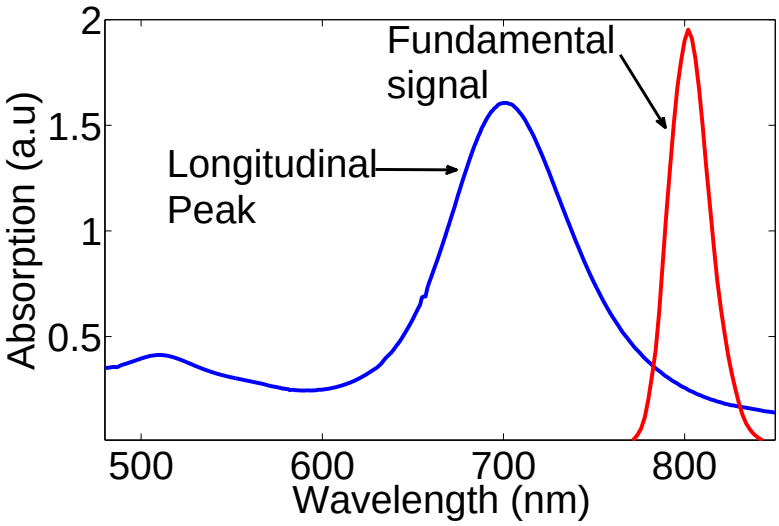

Figure 5.7: Different size and shape nanoparticle present in solution have different absorption spectra that add up to give the broad UV-Vis spectrum. The small peak at 520 nm is due to the transverse absorption of the spheroidal particles and the broad peak is the longitudinal absorption due different length particle in the solution.

where r_i is either r_l the radius for the 1 μm laser spot or r_n the radius of the circular area in the immediate of the nanorod of interest, with diameter equivalent to the length of the rod (40 nm). We can approximate the enhancement due to an individual nanorod as follow. First, we write down the total intensity of the signal after enhancement as a sum of the transmitted signal and the intensity of the signal from the nanorods:

$$I_{final} = \eta_{tot}(I_l + I_r)$$

where I_l and I_r are the laser spot intensity (spot containing no rods) and the intensity of the signal enhance by the rods respectively. But, we know that the signal from the spot containing no rods is not enhance thus the total intensity can also be written

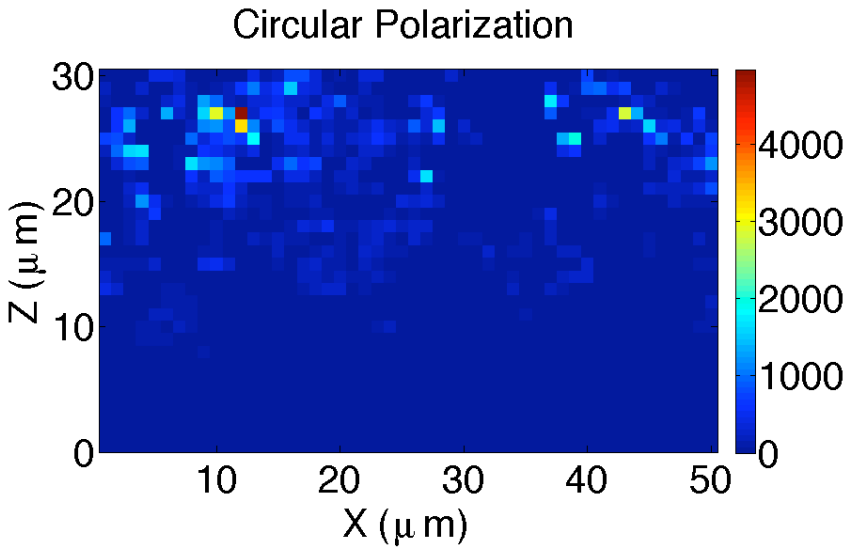

Figure 5.8: Area scanned with a circularly polarized light. Intensity graphs of THG 2-D scan of sample area. View of along the x (horizontal) axis and the z (vertical) axis with 1 μm steps in both directions. The lighter color represent the intensity of the THG signal in linear scale. High intensity signal is generated when we scan over a nanorod. The bright red dots represent the highest enhancement obtained

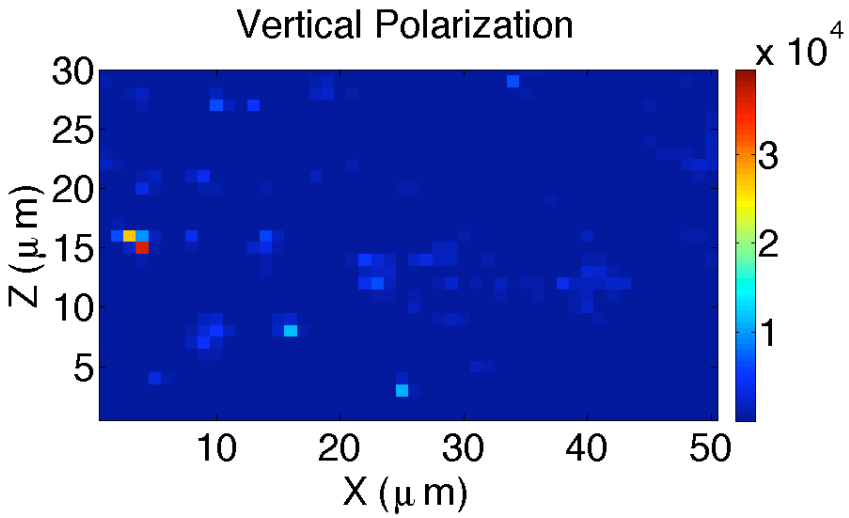

Figure 5.9: Area 2-D scan with a vertically polarized light. View of along the x (horizontal) axis and the z (vertical) axis with 1 μm steps in both directions.

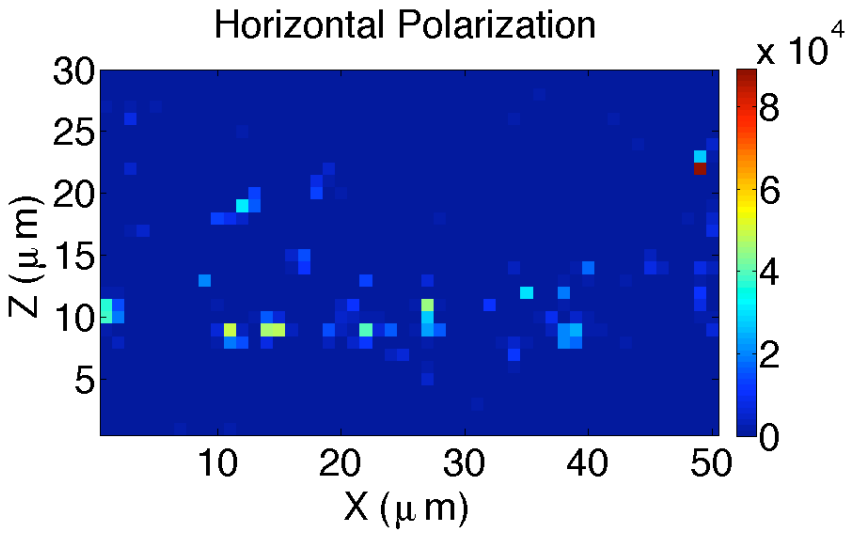

Figure 5.10: Area 2-D scan with a horizontally polarized light. View of along the x (horizontal) axis and the z (vertical) axis with 1 μm steps in both directions.

as:

$$I_{final} = I_l + \eta_{rod} I_r$$

thus,

$$\eta_{tot}(I_l + I_r) = I_l + \eta_{rod} I_r$$

where η_{tot} is the total enhancement of the signal taken directly from measurements and η_{rod} is the enhancement due to each rod respectively. Assuming the rods present in the laser spot are small compared to the spot surface area, we have:

$$\eta_{tot} = \frac{r_l^{-2} + \eta_{rod} r_n^{-2}}{r_l^{-2} + r_n^{-2}}$$

with the above expression we can then proceed to estimate the actual enhancement due to each nanorod in its immediate vicinity. After trivial manipulations we find that η_{rod} is $\sim 14.1 \times 10^4$. These results agree well with calculated enhancement factors from earlier theoretical calculations [73]. Where enhancement of the TH signal was

recorded to be $7\times\ 10^4$ at the tip of ellipsoidal nanostructures.

Next we proceed to determine that the nanoparticles used to enhance the THG signal, in the scanned area aren't destroyed after being subjected to such intense signals. We excite the THG scanned sample area with a coherent white light and measure the absorption spectrum. Figure 5.11 shows the spectrum of the scanned sample area, it clearly displays absorption at 800 nm confirming the presence of a few nanorods with plasmon absorption at the laser wavelength. Furthermore, the narrow width of the peak centered at 800 confirms that there are only a few particle present in the sample area as we stated above. To further reinforce this argument we took SEM images in figure 5.12 of the nanorods still present in the scanned area after laser irradiation.

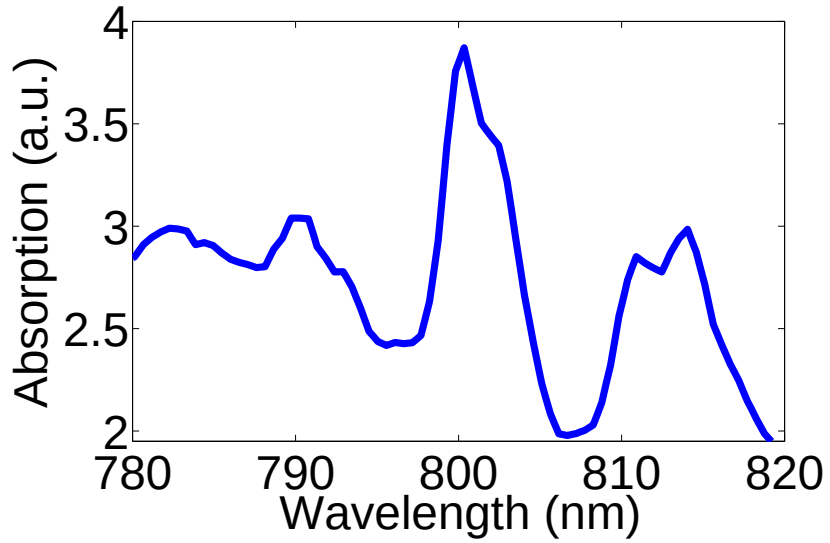

Figure 5.11: optical absorption spectrum of the sample of laser irradiation, obtained by excitation using a coherent light source.

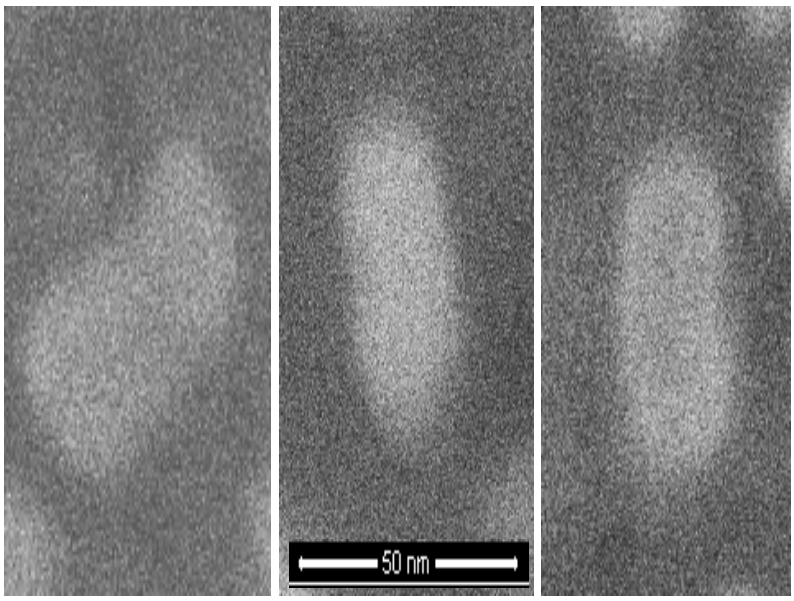

Figure 5.12: SEM image of parts of the sample area after laser (THG) irradiation; it shows that the area still contains Au rod of different shape and size

5.5 Conclusion

In conclusion, surface third harmonic light is enhanced by more than 3 orders of magnitude when polarized fundamental signal is resonant with the longitudinal surface plasmon of self assembled Au nanorods. These results show orders of magnitude higher intensities than previously measured enhanced TH signal by noble metal nanoparticle where the TH of the fundamental light is resonant with their Mie plasmon resonance. This is accomplished using very short and intense pulse energy but care was taken to avoid both optical and physical damage to the sample.

Conclusion and Future Work

Conclusion

Using electron energy loss spectroscopy inside the TEM, we have investigated the surface plasmon modes of individual and coupled spheroidal noble metal nanoparticles. We've discussed in details the relationship between EELS and optical spectroscopy techniques, in the process we've shown how the two techniques can become complementary.

Prior experiments have also investigated single particle spectra using both EELS [39, 85, 86, 87, 88] and near field optical spectroscopy [37, 38, 89, 90]:

- Using optical near field techniques, Klar *et al* have measured the homogeneous line shape of the surface plasmon resonance in single gold nanoparticles using a near-field optical antenna effect. More recently Estaban *et al* have mapped in real space and by purely optical means near-field optical information of localized surface plasmon resonances excited in nanoscopic particles.

- And using EELS Cowley *et al* have measured for the first time the predicted surface plasmon of spherical Aluminum nanoparticles (4.5 eV and 7.5 eV). Since then the energy resolution of EELS has greatly improved, thus Colliex *et al* have then been able to resolve the plasmon modes of silver nanotriangles (2.7 eV and

3.5 eV).

However, we are the first to bring both fields together by comparing electron spectroscopy techniques to optical techniques. We have shown that:

- Au nanostructures can be characterized using EELS and that all plasmon modes from spheroidal nanoparticles can be resolved at once.
- We have characterized coupled nanoparticles using EELS; such as the influence on the particle plasmon modes:
  - by showing evidence of plasmon peak shift
  - and field enhancement due to their electromagnetic coupling.
- Most importantly, we have shown that the results obtained from EELS experiment have strong similarities to those obtained by both experimental and theoretical optical characterization techniques.
- We have used EFTEM imaging to map the surface plasmon intensity distribution around single and coupled Au nanorods.
- We are the first to have shown that EFTEM intensity images are very similar to that of electromagnetic field distribution around Au nanorods simulated using the DDA method.
- We've also compared the decay of the surface plasmon intensity from experimental EFTEM images to intensity decay from the DDA calculations.

Indeed, most of the work presented in this thesis dwells at the emerging frontier at the intersection of optics and electron microscopy, by using electron energy loss

spectroscopy to characterize optical properties of individual and coupled nanostructures. It establishes that the dielectric function for a single metallic nanostructure can be deduced from EELS experiments. Most importantly, it shows that optics and EELS are in many ways complementary: optical measurements are good for high spectral but limited in spatial resolution, even using near-field techniques. Transmission electron microscopy/EELS is good for nanometer scale imaging and thus for detailed mapping of plasmon modes in nanostructures. Although EELS can distinguish different plasmon modes, it cannot yet produce meaningful measurements of spectral-line widths or shapes. Optical-frequency modes are accessible through both techniques and thus give us access to the full dielectric behavior of nanoparticles. However, a complete description still requires both. We expect that the intersection of optics and EELS will soon become a remarkably fruitful area of plasmonics research.

Indeed, surface plasmons of an optical wavelength concentrate light in a region that is considerably smaller than their wavelength, a feature that is the main ingredient behind the use of surface-plasmon polaritons for the fabrication of nanoscale photonic circuits operating at optical frequencies. Therefore, a full description of these properties at the nanoscale is needed for an efficient fabrication of nanoscale photonics circuits. We, thus expect a combination of EELS and optical spectroscopy to be an important an integral part of the future of nano-photonics design.

We also show that the local response of these nanostructures leads to strongly enhanced third harmonic signals. However, these enhancement properties extend far beyond non linear processes, they are crucial to the enhancement of evanescent waves

thus to the concept of the so-called superlens design. Through the excitation of surface plasmon, the perfect reproduction of the electromagnetic field of a source plane at the image plane is becoming a reality. This is one of the greatest and exciting challenges in todays physics, nanostructures with novel optical properties like -1 refractive index and nonlinear optical properties upon demand. Such novel nanostructures can allow measuring of fundamental photonic and electronic properties, additionally such structures can be used to measure and image very small objects in biology, materials science, etc.

We believe that collaborative investigations hold the key to perfect plasmonic designs. Indeed, joint efforts into the further advancements of numerical design tools, fabrication, as well as a combination of EELS and near-field optical characterization techniques, are needed to close the size gap between optical and electronic devices.

Future Work

The future of research at the frontier of electron microscopy and optics will benefit a great deal from progress in electron beam lithography for nanostructure design. Indeed, EELS analysis of nanostructures designed for negative material will greatly contribute to the advancement of metamaterial.

The idea is to design split ring resonators (SRR) onto a TEM substrate. The SRR consists of a planar set of concentric rings, each ring with a gap. Because the SRR is planar, it is easily fabricated by lithographic methods at scales appropriate for low frequencies to optical frequencies. In this structure, the coiled metal sheets have a self capacitance and self-inductance that create a resonance. The currents

that flow when this resonance is activated couple strongly to an applied magnetic field, yielding an effective permeability that can reach quite high values [62]. This resonant magnetic field can be characterize using EELS and the result compared to both experimental and theoretical optical characterization techniques.

Energy gain Spectroscopy: charged particles passing a dense gas of electron can also gain energy when they interact with plasmons already present in the electron gas. This process has already been reported in energy loss spectra of 10 keV electrons reflected from a liquid indium surface [91]. Thus the next major step in this project will be to implement an electron energy gain spectroscopy (EEGS) experiment to study the collective electronic behavior on nanostructured material. It will begin with the physics of SP generation, propagation, coupling and decay in spherical and ellipsoidal nanoparticles. This will enable details of processes to be seen experimentally; details that until now have been unresolved outside of theory and computation. This expeirment will be a combined and continued effort with existing projects studying similar physics with conventional TEM and optical spectroscopy. The preliminary EEGS experiment will involve quantum dots (QD) as first samples to physically observe the gain peak to the left of the zero loss peak.

The aim is to investigate the energy spectrum of a single zinc oxide (ZnO) quantum dots (QD) and nanostructures by means of high resolution electron energy loss spectroscopy (HR-EELS) in a transmission electron microscope (TEM). There are several motivations for performing EELS on ZnO quantum dots.

- Very few EELS experiments on semiconductor quantum dots have been reported; some results for of the size dependent energy gap of individual CdTe

QD has been explored using valence electron energy loss spectroscopy (VEELS) [48], and their optical absorption has also been studied using EELS in the TEM [92]. The primary problem for CdS and CdSe dots is sample degradation under the energetic electron beam. In contrast to this systems, ZnO should be far more robust, and has no organic surfactant necessary to passivate the surface, stabilize the particles, and prevent aggregation.

- ZnO is an important material e.g. for applications in blue/UV laser design using ZnO thin film [93] or nanowires [94]. A nm-resolution spatial map of the excitation spectrum would be an important contribution to the characterization of quantum-confined ZnO systems.

- Finally, these experiments will point the way to performing energy GAIN spectroscopy for the first time. Brief attempts to observe energy gain in plasmonic structures have previously been performed unsuccessfully, but it is expected a much larger signal to occur with quantum dot systems as opposed to plasmonic systems due to the longer upper state lifetime.

Initially a cw laser will be outfitted to the TEM; the appropriate laser light will induce electronic transition from the lower to the upper state of the QD. The electron beam will then induce radiative transition from the upper state to lower state thus gaining energy equivalent to the gap energy. This experiment will yield an energy gain peak intensity that will be a percentage of the energy loss peak intensity. The focus will then shift again to plasmonics to investigate the manipulation of optical energy on very fine details using SP and related phenomena.

The long term goal of this project will see the implementation of an ultrafast TEM.

It will consist of a high resolution analytical TEM outfitted with an ultrafast laser to yield high spatial and temporal resolution. Every event in the lifetime of an SP wave (generation, propagation, interaction, scattering, and eventual decay) will be captured with extremely high spatial, temporal, and spectroscopic resolution. The program will be expanded to broader classes of nanostructured materials and new areas of physics (within the general category of collective electronic behavior), uncovering the intrinsically interesting complexity of collective electronics while also revealing the details of processes essential to future technology.

BIBLIOGRAPHY

BIBLIOGRAPHY

[1] M. Faraday. *Experimental Relation of Golg (and other Metals) to Light*, volume 147. Trans. Royal Soc., London, 1857.

[2] G. Schmid. *Clusters and Colloids: from Theory to Application.* VCH: Weinheim, 1994.

[3] S. Link and M. A. El-Sayed. Spectral properties and relaxation dynamics of surface plasmon electronic oscillations in gold and silver nanodots and nanorods. *J. Phys. Chem. B*, 103(8410-8426), 1999.

[4] G. Mie. Beiträge zur optik trüber medien, speziell kolloidaler metallösungen. *Ann. Phys.*, 25, 1908.

[5] R. Gans. *Ann. Phys.*, 47:270, 1915.

[6] Craig F. Bohren and Donald Huffman. *Absorption and Scattering of Light by Small Particles.* John Wiley & Sons, Inc, 1st edition, 1998.

[7] U. Kreibig and M. Vollmer. *Optical Properties of metal Clusters.* Springer, Berlin, 1995.

[8] Charles Kittel. *Introduction to Solid State Physics.* Wiley NY, 7th edition, 1995.

[9] A. Hohenau A. Leitner and F. R. Aussenegg. *Surface Plasmon nanophotonics.* 131. Springer Series in Optical Sciences, 2007.

[10] J. D. Jackson. *Classical Eletrodynamics.* John Wiley Sons, Inc, third edition, 1998.

[11] R. H. Ritchie. Plasma losses by fast electron in thin films. *Phys. Rev.*, 106(5), 1957.

[12] J. M. Pitarke V. M. Silkin E. V. Chulkov and P. M. Echenique. Theory of surface plasmons and surface-plasmon polaritons. *Reports on Progress in Physics*, 70:1–87, 2007.

[13] Stefan Alexander Maier. *Plasmonics: Fundamentals and Applications.* Springer Science, 2007.

[14] M. Kerker. *The Scattering of Light and Other Electromagnetic Radiation.* Academic Press, New York, 1969.

[15] S. Link M. B. Mohamed and M. A. El-Sayed. Simulation of the optical absorption of au nanorods... *J. Phys. Chem. B*, 103:3073 – 3077, 1999.

[16] Susie Eustis and Mostafa A. El-Sayed. Determination of the ar statistical distribution of au nanorods... *J. App. Phys.*, 100(044324), 2006.

[17] Mostafa A. El-Sayed. Some interesting properties of metals... *Accounts of Chemical Research*, 34(4):257 – 264, 2001.

[18] Luis M. Liz-Marzan. Colourful: Plamonics of tailored metal nanoparticle colloids. *Optical material Effects*, 1, 2008.

[19] P. B. Johnson and R. W. Christy. *Phys. Rev. B.*, 6, 1972.

[20] C. A. Foss *et al. J. Phys. Chem.*, 96:9001, 1992.

[21] David Pines. *Elementary Ecitations in Solids: Lectures on Phonons, Electrons, and Plasmons.* W. A. Benjamin, Inc, 1964.

[22] B. L. Illman V. E. Anderson R. J. Warmack and T. L. Ferrell. Spectrum of surface mode contribution to the diffrential energy loss probability for electron passing by a spheroid. *Phys. Rev. B*, 38(5):3045, August 1988.

[23] D. Pines and D. Bohm. *Phys. Rev.*, 85(338), 1952.

[24] F. J. Garcia de Abajo. *Relativistic energy loss and induced photon emission in the interaction of a dielectric sphere with an external electron beam. Phys. Rev. B*, 59(4):3095, January 1999.

[25] E. Hoa and G. C. Schatz. Em fields around ag nanoparticles and dimers. *J. Chem. Phys.*, 120(1):357, 2004.

[26] William R. Smythe. *Static and Dynamic Electricity.* Hemisphere Publishing Corporation, third edition, 1989.

[27] B. K. P. Scaife. The dielectric spheroid revisited. *Journnal of Molecular Structure*, 479:285 – 297, 1999.

[28] T. L. Ferrell and P. M. Echenique. *Phys. Rev. Lett.*, 55:1526, 1985.

[29] T. L. Ferrell *et. al. Phys. Rev. B*, 35:7365, 1987.

[30] F. J. Garcia de Abajo and A. Howie. *Phys. Rev. Lett.*, 80(23):5180, June 1998.

[31] Martin Dressel and Geoger Grüner. *Electrodynamics of Solids.* Crambridge University Press, 2002.

[32] ArnoldJ. Glick and Richard A. Ferrell. Single particle excitation of a degenerate electron gas. *Ann. Phys.*, 11:359 – 376, 1960.

[33] Encai Hoa *et al.* Optical properties of metal nanoshells. *J. Phys. Chem. B*, 108:1224–1229, 2004.

[34] J. J. Mock *et al. J. Chem. Phys.*, 116, 2002.

[35] A. Graff et al. *Eur. Phys. J. D.*, 34:263 – 269, 2005.

[36] N.R. Jana C.J. Murphy. *Adv. Mater.*, 14(1):80–82, 2002.

[37] T. Klar *et al.* Surface plasmon resonance in single metallic nanoparticle. *Phys. Rev. Lett.*, 80(19), 1998.

[38] C. Sönnichsen *et al. Phys. Rev. Lett.*, 88(7):077402, 2002.

[39] Jaysen Nelayah *et al.* Mapping surface plasmon on a single metallic nanoparticle. *Nature Physics*, 575, 2007.

[40] P. E. Batson. Surface plasmon in cluster of small spheres. *Phys. Rev. Lett.*, 49(13):936, 1982.

[41] R. F. Egerton. *Electron Energy Loss Spectroscopy in the Electron Microscope,* 2^{nd}*ed.* Plenum Press, NY and London, 1996.

[42] I. R. Khan *et al.* A tem and eels investigation of the active and inactive ag for serrs. *Faraday Discuss.*, 132:171–178, 2006.

[43] N.R. Jana *et al. Chem. Commu.*, page 617, 2001.

[44] Nikhil R. Jana *et al. J. Phys. Chem. B*, 105:4065 – 4067, 2001.

[45] Kylee Korte. *National Nanotechnology Infrastructure Network*, page 28, 2007.

[46] A. Gloter *et al. Ultramicroscopy*, 96:385 – 400, 2003.

[47] Le Qui *et al. IEEE J. Sel. Top. Quantum Electron.*, 13(6), 2007.

[48] R. Erni and N. D. Browning. *Ultramicroscopy*, 107:267 – 273, 2007.

[49] Jorg P. Kottman *et al. Phys. Rev. B*, 64(235402), 2001.

[50] Y. Gao *et al. Jour. of Crystal Growth*, 276:606 – 612, 2005.

[51] K. H. Su *et al.* Interparticle effect on pr of nanogold particles. *Nano Letters*, 3(8):1087 – 1090, 2003.

[52] W. Rechberger *et al.* Optical properties of two interacting particles. *Opt. Comm.*, 220:137 – 141, 2003.

[53] M. Quinten *et al.* Optical absorption of pairs of small metal particles. *Surf. Sci*, 156:741 – 750, 1985.

[54] S. A. Maier *et al. App. Phys. Lett.*, 81, 2002.

[55] H. F. Hamann *et al. J. Chem. Phys.*, 114, 2003.

[56] A. Hartschub *et al. Phys. Rev. Lett.*, 90, 2003.

[57] M. Moskovits. *Rev. Mod. Phys.*, 57(783), 1986.

[58] A. Takashi and A. V. Zayats. *App. Phys. Lett.*, 80(1536), 2002.

[59] Y. C. Cao *at al. Science*, 297:1536, 2002.

[60] M. N'Gom *et al.* Single particle plasmon spectroscopy... *Nano Letters*, 8(10):3200 – 3204, 2008.

[61] M. Bosman *et al. Nanotechnology*, 18(165505):5pp, 2007.

[62] D. R. Smith *et al.* Metamaterials and negative refractive index. *Science*, 305:788 – 792, August 2004.

[63] T. Atay *et al. Nano Letters*, 4(9):1627 – 1631, 2004.

[64] B Schaffer U Hohenester A Trügler and A Hofer. *Phys. Rev. B*, 79(041401 (R)), 2009.

[65] J. J. Goodman B.T̃. Draines and P.J̃. Flatau. *Opt. Lett.*, 16(15), 1991.

[66] F. Hofer *et al.* Imaging of nanometer-sized precipitates in solids by electron spectroscopic imaging. *Ultramicroscopy*, 59:15 – 31, 1995.

[67] M. A. Aronova *et al.* Quantitative eftem mapping of near physiological calcium concentrations in biological specimens. *Ultramicroscopy*, 109:201 – 212, 2009.

[68] Arvi Sundaramurthy *et al. Phys. Rev. B*, 72(165409), 2007.

[69] B. T. Draine and P. J. Flatau. User guide to the discrete dipole approximation code ddscat 7.0.

[70] R. Dallapiccola A. Gopinath F. Stellaci L. D. Negro. *Opt. Express*, 16(8), 2008.

[71] J. A. Squier *et al. Opt. Lett.*, 3:315 – 324, 1998.

[72] Y. Barad *et al. Appl. Rev. Lett.*, 70, 1997.

[73] Thomas Y. F. Tsang. *Opt. Lett.*, 88, 1996.

[74] E. M. Kim *et al. Phys. Rev. Lett.*, 95:227402, 2005.

[75] Tzu Ming Liu *et al. App. Phys. Lett.*, 89:043122, 2006.

[76] N. Del Fatti and F. Valle. *Phys. Rev. A*, 56:4116–4126, 1995.

[77] Thomas Y. F. Tsang *et al. Phys. Rev. A*, 52, 1995.

[78] M. Pelton *et al. Cond. Mat. Mtrl Sci*, 4(0506158), 2006.

[79] M. Lippitz *et al. Nano Letters*, 5(4):4799 – 47802, 2005.

[80] R. Boyd. *Nonlinear Optics*. Academic Press, New York, 1992.

[81] T. B. Norris *et al. Opt. Lett.*, 17, 2002.

[82] D. Stricklank and G. Mourou. Compression of amplified chirped optical pulses. *Optics Communications*, 56(3):219–221, 1985.

[83] R. Chadwick *et al. UCRL JRNL*, 223054, 2006.

[84] D. Oron *et al. Opt. Lett.*, 28(23):2315 – 2317, 2003.

[85] Z. L. wang and J. M. Cowley. *Utramicroscopy*, 21:77, 1987.

[86] Z. L. wang and J. M. Cowley. *Utramicroscopy*, 21:347, 1987.

[87] Z. L. wang and J. M. Cowley. *Utramicroscopy*, 21:335, 1987.

[88] Z. L. wang and J. M. Cowley. *Utramicroscopy*, 23:97, 1987.

[89] R. Hillenbrand and F. Keilmann. Optical oscillation modes of plasmon particles observed in direct space by phase-contrast near-field microscopy. *App. Phys. B.*, 73:239–243, 2001.

[90] R. Estaban *et al.* Direct near-field optical imaging of higher order plasmonic resonances. *Nano Letters*, 8(10):3155 – 3159, 2008.

[91] J. Schilling and H. Raether. *J. Phys. C.: Solid State Phys.*, 6, 1973.

[92] M. L. Redgolo *et al*. Optical absorption and transmission electron microscopy analysis of cdte quantum dots size distribution. *Micros. Microanal*, 9(suppl 2), 2003.

[93] V. Srikant and D. R. Clarkea. On the optical band gap of zinc oxid. *J. of App. Phys*, 83(10), 1998.

[94] B. P. Zhang N. T. Binh and Y. Segawa. Optical properties of zno rods formed by metalorganic chemical vapor deposition. *App. Phys. Lett.*, 83(8), 2003.